Ab initio **unraveling of structural, magnetic, and optical properties of monosulfides and vacancy clustering in perovskite heterostructures**

Dissertation
zur Erlangung des Doktorgrades
der Naturwissenschaften

vorgelegt beim Fachbereich Geowissenschaften/Geographie
der Johann Wolfgang Goethe-Universität
Frankfurt am Main

von
Artem Chmeruk
Ukraine

Frankfurt 2023
(D30)

vom Fachbereich Geowissenschaften/Geographie der Johann Wolfgang Goethe-Universität als Dissertation angenommen

Dekan: Prof. Dr. Jürgen Runge

Erster Gutachter:
Prof. Dr. Maribel Núñez-Valdez

Zweiter Gutachter:
Prof. Dr. Björn Winkler

Datum der Disputation
24.11.2023

Contents

List of Tables

List of Figures

Zusammenfassung

Sogenannte “First-principle”- Modellierungstechniken bieten die Möglichkeit, eine Vielzahl von Systemen unter unterschiedlichen physikalischen Bedingungen wie Temperatur, Druck und Zusammensetzung zu simulieren, ohne auf empirisches Wissen angewiesen zu sein. Die Dichtefunktionaltheorie (DFT) [1, 2], eine quantenmechanische Methode, hat sich als außergewöhnlich erfolgreiches Rahmenwerk für die Modellierungen in den Materialwissenschaften etabliert. Durch den Einsatz von DFT ist es möglich, wertvolle Einblicke in den grundlegenden Zustand eines Systems zu gewinnen und Gleichgewichtskristallstrukturen zuverlässlich zu bestimmen. Im Laufe der Zeit hat sich DFT zu einem unverzichtbaren Werkzeug entwickelt, das zur Vorhersage von Eigenschaften eines Materials im Zusammenhang mit seiner Struktur, seinem isolierenden/metallischen Verhalten, Magnetismus und Optik in verschiedene Schemata integriert werden kann. DFT wird regelmäßig in zahlreichen Bereichen angewendet, von grundlegenden Themen in der Physik der kondensierten Materie bis hin zur Untersuchung von Phänomenen im großen Maßstab in den Geowissenschaften. In letzteren ist die Effektivität von DFT darauf zurückzuführen, dass sie die Eigenschaften von Materialien simulieren kann, die auf der Erde, anderen Planeten und in Meteoriten vorkommen und deren Untersuchungen im Labor große experimentelle Herausforderungen darstellen könnten. In dieser Arbeit wurde eine umfassende Untersuchung einer Familie von Monosulfiden und einer Perowskit-Heterostruktur durchgeführt. Diese Materialien sind aufgrund ihrer potenziellen Anwendungen in Technologie und Energiegewinnung [10, 21−29, 38−44, 73−77] sowie im Fall der Monosulfide aufgrund ihrer vermuteten Häufigkeit auf dem Planeten Merkur relevant [45−50]. Zunächst wurde ein DFT-Ansatz verwendet, um zwei nichtmagnetische Monosulfide, CaS und MgS, zu analysieren. Der Schwerpunkt lag auf der Bestimmung ihrer strukturellen Eigen-

schaften und der Modellierung des Reflexionsverhaltens im Infrarotbereich. Bei der Berechnung der Reflexion wurden sowohl harmonische als auch anharmonische Beiträge berücksichtigt [194]. Im harmonischen Limit wurde die nichtanalytische Korrektur verwendet [215], um die LO/TO-Aufspaltung genau zu bestimmen. Eine genaue Berechnung der TO- und LO-Moden ist entscheidend, da sie die Grenzen des sogenannten Reststrahlenbands festlegen, das heißt die niedrigen und hohen Frequenzgrenzen der maximalen Reflexion. Um die Dämpfung in der Reflexion korrekt zu simulieren, wurden anharmonische Effekte einbezogen. Dies wurde durch Verwendung der Störungstheorie erreicht, wobei Dreiphononen-Streuungen [95, 96] und Isotopen-Unordnungsprozesse [97] in den Berechnungen berücksichtigt wurden. Es wurde festgestellt, dass diese Effekte hauptsächlich die Verbreiterung der Kanten der Reflexionsspektren beeinflussen, wobei ein stärkerer Einfluss bei höheren Wellenzahlen zu beobachten ist.

Während höhere anharmonische Terme wie Vier-Phononen-Streuungen in dieser Studie nicht berücksichtigt wurden, ist es angemessen anzunehmen, dass diese Prozesse nur bei höheren Wellenzahlen jenseits des Maximums der Reflexions-Bande erkennbar wären. Diese höheren anharmonischen Terme könnten möglicherweise die in den vorhergesagten Reflexionsspektren beobachteten Spitzen beseitigen. Schließlich wurde argumentiert, dass es sinnvoll sein könnte, die Integration anharmonischer Terme in die Modellierung von polykristallinen und Pulverproben zu untersuchen. Ihre Rolle in solchen Fällen wird jedoch als zweitrangig angesehen, da die Dämpfung (Selbstenergie) in diesen Systemen hauptsächlich von Prozessen beeinflusst wird, die für Pulverproben charakteristisch sind, wie zum Beispiel diffuse Reflexion und Brechung.

Zweitens wurden vier verschiedene Polymorphe von MnS unter Verwendung einer Kombination von “First-principles”-Methoden untersucht, um den antiferromag-

netischen (AFM) und paramagnetischen (PM) Zustand zu simulieren. Die Integration von DFT+U [147, 152, 190, 200] mit Superzellen von speziellen Quasizufallsstrukturen (SQS) [92] und Techniken zur Kontrolle der Besetzungsmatrix [176] war entscheidend, um Konvergenz, Genauigkeit bei der Strukturoptimierung und die Erzielung von endlichen Energiebandlücken und lokalen magnetischen Momenten in den PM-Phasen zu erreichen. Die Hinzufügung der Hubbard-U-Korrektur war notwendig, um die stark korrelierten Mn-d-Elektronen zu behandeln. Der Erfolg des Ansatzes zeigte sich deutlich an den Vorhersagen zur elektronischen Struktur für das PM-Steinsalz-B1-MnS-Polymorph. Experimentell wurde festgestellt, dass diese Phase ein Isolator ist [229, 234], aber mehrere frühere *ab initio*-Arbeiten prognostizierten metallisches Verhalten [230, 235]. Die Berechnungen in dieser Arbeit sagten hingegen isolierende und magnetische Eigenschaften voraus, was gut mit vorhandenen Messungen übereinstimmt. Darüber hinaus wurden die Auswirkungen einer hydrostatischen Kompression auf die MnS-Polymorphe untersucht, indem die Energieänderungen bei der Relaxation der ionischen und gitternahen Freiheitsgrade getrennt wurden. Die berechneten Enthalpien zeigten, dass die kubische PM-B1-MnS-Struktur die stabilste Phase bis etwa 21 GPa ist, die danach in das orthorhombische B31-MnS-Polymorph übergeht. Diese Trends der elektronischen Struktur und der Phasenübergänge sind natürlich vom jeweiligen U-Wert abhängig. Eine Erhöhung oder Verringerung des U-Werts würde zu Veränderungen der strukturellen Parameter und der Größenordnung des Übergangsdrucks führen. Der in dieser Arbeit gewählte U-Wert basierte auf anderen Studien zu Mn in oktaedrischer Symmetrie [175] und wird auch durch die enge Übereinstimmung zwischen den vorhergesagten und experimentellen strukturellen Parametern unterstützt [81−83]. Bemerkenswerterweise ist die vorhergesagte B1→B31-Transformation einem strukturellen Phasenübergang sehr ähnlich,

der in Hochdruckexperimenten (von B1-MnS ausgehend) beobachtet wurde [80−83], was den in dieser Studie verwendeten Modellierungsansatz weiter validiert.
Die atomaren Schwingungen der PM-B1-, B4- und B31-MnS-Polymorphe wurden auch unter Benutzung der harmonischen Annäherung untersucht. Dazu wurde auch die SQS Technik angewandt mit dem Ziel Konfigurationen für die lokalen magnetischen Momente zu erhalten, die frei von weichen Moden sind. Die Suche nach dynamisch stabilen SQS-Konfigurationen beinhaltete für jedes Polymorph verschiedene Strategien, die letztendlich zur vollständigen Beseitigung von Moden mit negativen Frequenzen führten. Zusätzlich wurden die optischen Eigenschaften der PM-B1- und B4-MnS-Polymorphe jenseits der harmonischen Näherung berechnet. Aufgrund seiner Bedeutung wurde das PM-B1-MnS-Polymorph eingehend untersucht, indem die vollständige interatomaren Kraftkonstante (IFC) dritter Ordnung berechnet wurde. Das resultierende Reflexionsverhalten ist in angemessener Übereinstimmung mit experimentellen Daten, insbesondere in Bezug auf die LO/TO-Aufspaltung von MnS, das auf einem Glassubstrat gewachsen war [229, 238]. Beobachtete Abweichungen können teilweise auf spezifische Anpassungsverfahren zurückgeführt werden, die bei den Reflexionsmessungen verwendet wurden. Die größte Abweichung könnte jedoch der Natur des experimentellen Systems selbst zugeordnet werden. Während die Modellierung in dieser Arbeit an Einkristall-B1-MnS durchgeführt wurde, basierten Experimente aus der Literatur auf polykristallinen Dünnschichten und gepressten Pulverproben, Solche Experimente unterscheiden sich stark von Einkristallexperimenten. Aufgrund der geringeren Symmetrie der B4-MnS- und B31-MnS-Polymorphe wäre eine signifikant größere Anzahl von Verschiebungskonfigurationen erforderlich gewesen, um die vollständigen IFC-Matrizen zu konstruieren. Aber aufgrund von beschränkter Rechenkapazität wurde nur die B4-MnS-Phase mit einer reduzierten Anzahl von Verschiebungskon-

figurationen modelliert. Unter solchen Einschränkungen zeigte das berechnete Reflexionsverhalten des B4-MnS-Polymorphs nur eine geringfügige Abweichung von dem idealisierten ungedämpften Fall, was darauf hindeutet, dass die Hauptdämpfungsprozesse jenseits der betrachteten Grenzweite der Phononwechselwirkung auftreten. Nichtsdestotrotz stimmten die berechneten optischen Parameter des Reststrahlenbands gut mit den experimentellen Daten überein [238]. Daher kann angenommen werden, dass die Verwendung der vollständigen IFC-Matrix zu einem genaueren Vergleich zwischen den berechneten und experimentellen Ergebnissen für den B4-MnS-Polymorph führen würde.

Schließlich wurde die sauerstoffdefiziente Heterostruktur von $LaAlO_{3-\delta}/SrTiO_{3-\delta}$ unter Anwendung von DFT+U untersucht, mit besonderem Augenmerk auf die potenziellen Auswirkungen von Leerstellen-Clusterbildung an der Grenzfläche. Sauerstoffleerstellen wurden simuliert, indem manuell zwei Sauerstoffatome entfernt wurden. Abhängig von der Distanz zwischen einem Ti-Platz und den Sauerstoffleerstellen können verschiedene Mechanismen der Orbitalrekonstruktion auftreten. Wenn ein Ti-Platz nicht direkter Nachbar einer Sauerstoffleerstellen ist, wird die t_{2g}-Symmetrie aufgehoben, was zu einer energetischen Absenkung des d_{xy}-Orbitals führt. Dieses Phänomen wurde auch in stöchiometrischen LAO/STO-Heterostrukturen beobachtet, bei denen es aufgrund von Phänomenen der polaren Katastrophe zu einer Umverteilung der Valenzelektronen kommt [10, 240, 243]. Speziell die Energieabsenkung des d_{xy}-Orbitals kann auf Veränderungen im umgebenden Kristallfeld als Störungursache zurückgeführt werden [88, 89]. Die Absenkung des d_{xy}-Orbitals wurde auch für Ti-Positionen beobachtet, die benachbart zu den Sauerstoffleerstellen lagen. In diesem Fall ist jedoch die energetische Verringerung der e_g-Orbitale signifikanter. Es wurde deduziert, dass diese Zustände zur Entstehung lokaler magnetischer Momente an der sauerstoffde-

fizienten LAO/STO-Grenzfläche beitragen. Insgesamt wurden sechs verschiedene Konfigurationen von Paaren von Leerstellen an der Grenzfläche untersucht. Unter den sechs untersuchten Konfigurationen beinhaltete die energetisch stabilste Konfiguration Sauerstoffleerstellen, die gebenüber einem Ti-Platz linear angeordnet waren.

Abstract

First-principles modeling techniques offer the ability to simulate a wide range of systems under different physical conditions, such as temperature, pressure, and composition, without relying on empirical knowledge. Density functional theory (DFT), a quantum mechanical method, has become an exceptionally successful framework for materials science modeling. Employing DFT makes it possible to gain valuable insights into the fundamental state of a system, enabling the reliable determination of equilibrium crystal structures. Over time, DFT has become an essential tool that can be incorporated into various schemes for predicting the properties of a material related to its structure, insulating/metallic behavior, magnetism, and optics. DFT is regularly applied in numerous fields, spanning from fundamental subjects in condensed matter physics to the study of large-scale phenomena in geosciences. In the latter, the effectiveness of DFT stems from its ability to simulate the properties found on the Earth, other planets, and meteorites, which may pose challenges for their direct study or laboratory investigation.

In this thesis, a comprehensive examination of a family of monosulfides and a perovskite heterostructure was conducted. These materials are relevant for their potential applications in technology, energy harvesting, and in the case of monosulfides, their speculated abundance on the planet Mercury.

Firstly, a DFT approach was used to analyze two non-magnetic monosulfides, CaS and MgS. We determined their structural properties and then focused on the modeling of their reflectivity in the infrared region. The calculation of the reflectivity considered both harmonic and anharmonic contributions. In the harmonic limit, the non-analytic correction was employed to accurately determine the LO/TO splitting, which is necessary to delimit the retstrahlend band, that

is, the maximum of the reflectivity. The anharmonic effects given by up to three-phonon and isotopic scatterings, which were included using perturbation theory, primarily smeared the reflectivity spectra edges in the high-wave region.

Secondly, four polymorphs of MnS were studied using a combination of first-principles methods to simulate their antiferromagnetic (AFM) and paramagnetic (PM) states. The integration of DFT+U with special quasirandom structures (SQS) supercells, and occupation matrix control techniques was crucial for achieving convergence, structural optimization accuracy, and obtaining finite energy band gaps and local magnetic moments in the PM phases. The addition of the Hubbard U correction was necessary to treat the highly-correlated Mn d-electrons. The success of our approach was clear based on our electronic structure predictions for the PM rock-salt B1-MnS polymorph. Experimentally this phase has been observed to be an insulator, but multiple *ab initio* works resulted previously in metallic behavior. Our computations, on the other hand, predicted insulating and magnetic properties that compare well with available measurements. Additionally, the pressure-field stability of the four MnS polymorphs was studied. In the case of the PM phases, B1-MnS was identified to be the most stable up to about 21 GPa, then transforming into the B31-MnS polymorph. This finding was in close agreement with high-pressure experiments reporting a similar phase transformation. The optical properties of B1-, B4-, and B31-MnS were also simulated. The SQS technique was used to obtain soft-mode-free phonon band structures within the harmonic approximation. Then, the anharmonic effects were included, and the reflectivity was calculated for B1-MnS and B4-MnS. In both cases, a good agreement for the LO/TO splitting was achieved in comparison to experimental results.

Lastly, the oxygen-deficient heterostructure of $LaAlO_{3-\delta}$ /$SrTiO_{3-\delta}$ was investi-

gated also employing DFT+U, with a particular emphasis on the potential impact of vacancy clustering at the interface. Six distinct configurations of pairs of vacancies were studied and their energies were compared to find the most stable one. The orbital reconstruction of Ti orbitals was also examined based on their location with respect to the vacancies and the local magnetic moments were calculated. The final results showed that linearly arranged vacancies located opposite to Ti ions give the most energetically stable configuration.

Chapter 1

Introduction

First-principles modeling techniques allow the simulation of a variety of systems under diverse physical conditions such as temperature, pressure, composition, etc., without resorting to any empirical knowledge. The bedrock for a considerable part of modeling in materials science is given by density functional theory (DFT) [1, 2]. DFT provides insights into the ground state of a system, from which reliable information about the crystal structure at equilibrium can be obtained. Over the years, DFT has become an indispensable tool that can be integrated into various frameworks for predicting structural, electronic, magnetic and optical properties. There several fields where DFT has found its use ranging from fundamental topics in condensed matter physics to large-scale phenomena in geosciences. In the latter, the success of DFT is derived from simulating the properties of the constituent materials of the Earth, other planets, and meteorites, which sometimes are difficult to study directly or in the laboratory.

Various physical properties such as optical and thermal properties can be studied through different types of excitations. For instance, atomic vibrations, or phonons, can describe the optical response of a material in the infrared (IR) region, whereas transition rates of different electronic states between the valence and conduction

band determine the optical properties in the visible region. It is worth noticing that although DFT does not allow direct access to the energy of excited states, it can still provide useful information to understand such properties [3].

The family of sulfide materials plays a vital role in various industries and applications, making it an important subject of study in chemistry and materials science. In addition to being one of the main sources of metals [4], various sulfide compounds have been investigated for their potential use as catalysts [5], thermoelectrics [6], in solar cells [7] and energy storage materials [8]. In this thesis, a series of binary non-magnetic and magnetic sulfides, specifically CaS, MgS, and MnS are investigated.

Perovskites are another extremely important class of materials that depending on the chemical composition can exhibit a great variety of physical properties. In recent years, heterostructures of various perovskites have become a topic of enormous interest [9, 10]. Such structures allow to create model systems with tailored exchange interactions at the atomic length scale, leading, for instance, to unique magnetic properties and potentially new applications [11]. A fascinating example is the observation of robust magnetism at the interface of two non-magnetic materials [12], as in the case of $LaAlO_3/SrTiO_3$ (LAO/STO). LAO/STO has been shown to exhibit coexistence of magnetism and superconductivity at the interface, which are generally mutually exclusive phenomena [13, 14].

1.1 Non-magnetic sulfides: CaS and MgS

CaS and MgS crystallize into the rock-salt structure (B1), space group $Fm\bar{3}m$, Fig. 1.1. Naturally, CaS is present in the mineral known as oldhamite [15]. It is found exclusively in enstatite-rich meteorites [15]. MgS is contained in the mineral niningerite [16]. This mineral is rare in the Earth and is usually found in

meteorites [16]. Both compounds are highly ionic, which determines their high melting temperatures, 2797 K and 2,499 K for CaS and MgS, respectively [17]. At ambient pressure and increasing temperature, these sulfides do not undergo any phase transitions and remain in the B1 structure up until their melting point. On the other hand, it has been recently suggested that at room temperature, CaS undergoes a pressure-induced structural transition from B1 to a CsCl-type (B2) structure at about 40 GPa [18]. CaS-based compounds are known for their

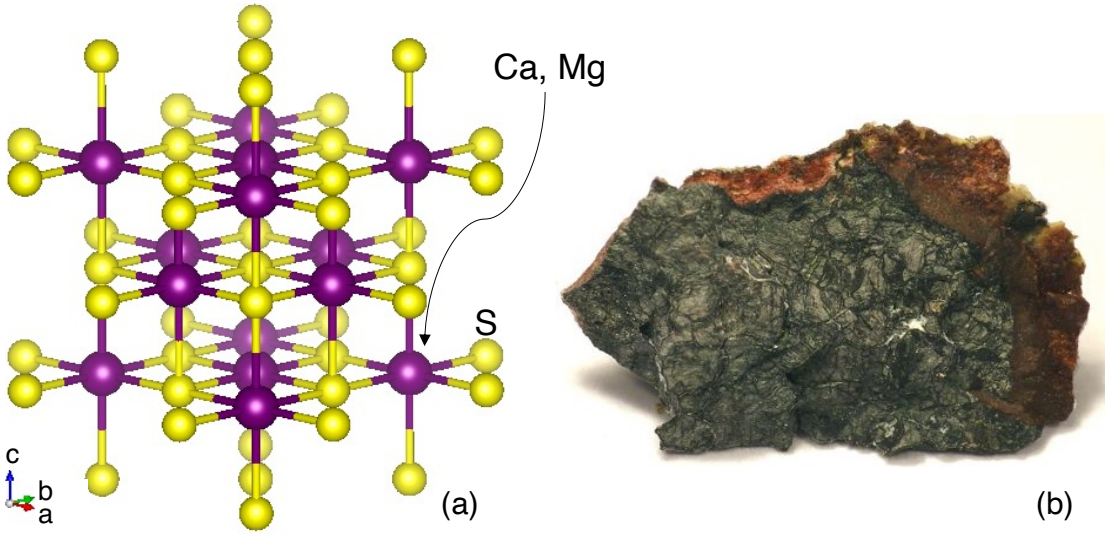

Figure 1.1: (a) Crystal structure and (b) naturally occuring CaS and MgS [19]. The crystal structure was generated by VESTA [20].

extensive use as host materials for highly efficient photoluminescents, cathodoluminescents, and X-ray phosphors [21–29]. The most common dopant centers include Sm^{3+} [21], Eu^{2+} [22], Ce^{3+} [25], Bi^{3+} [26] and Pb^{2+} [28, 29]. A recent attempt to search for efficient phosphors involves reduced dimensionality, i.e., nanoparticles of various shapes and sizes. To this end, "simple sulfides" like CaS have been considered [30–34].

MgS has been studied in the context of potential host materials for phosphors, albeit to a lesser extent than CaS [23, 35–37]. Some of the popular dopant centers

include Ce^{3+} [23], Sm^{3+} [35], Eu^{2+} [36], Bi^{3+} [37], etc. Finally, various compositions of $Ca_{1-x}Mg_xS$ have been studied as the host to tune the color coordinates [24, 27]. Lately, MgS has also attracted attention in the context of rechargeable batteries [38–44]. Reversible Mg batteries (RMB) are a promising substitute for Li-ion batteries. They offer almost a twofold increase in volumetric capacity as well as a dendrite-free Mg metal anode [38, 41]. However, the lack of high-performance cathodes severely limits any practical application of RMB [41]. Various candidates for cathode materials continue to be tested, one of which is S [41, 44]. Using S as a cathode could potentially improve the kinetics of Mg intercalation [41]. However, these systems (Mg/S) are plagued by the creation of electrochemically inactive MgS_x, and, up to now, no Mg/S batteries have been shown as fully reversible [39, 43]. Nevertheless, different strategies are being probed to enhance reversibility, e.g., by reactivating MgS_x with Li^+ [39]. Overall, the advantage of developing Mg-based rechargeable batteries is significant, thus reinforcing the need for MgS studies, as this compound plays an important role in the chemistry of RMB candidates.

Aside from energy and technological applications, CaS and MgS are of interest in the study of other planets. From 2011 to 2015, the MESSENGER mission collected spectral data of Mercury to construct a comprehensive mineralogical map of the planet's surface [45–50]. Currently, it is speculated that Mercury was created under extremely reduced conditions, which led to the planet's enrichment in S [47, 48]. The mineral oldhamite (CaS) is one of the bearers of S on Mercury's surface. MgS has also been identified as one of the sulfides present in hollow regions on Mercury [51]. In 2018, the BepiColombo mission to Mercury was launched, and it is due to enter Mercury's orbit in 2025 [49, 50]. In contrast to the spectrometers onboard the MESSENGER mission, which investigated the

planet's spectrum in the visible and X-ray range, the BepiColombo has also tools to study the infrared (IR) range [52]. Investigating the spectral characteristics of CaS and MgS in the IR region could complement the BepiColombo data to have a thorough understanding of Mercury.

1.2 Magnetic sulfides: MnS polymorphs

MnS is known to exist in several structural modifications. It most commonly crystallizes in the B1 structure, Fig. 1.2(a). Unlike CaS and MgS, MnS is mostly covalent [53], which determines its comparatively lower melting point of 1883 K [17]. In addition to the B1 structure, there are also zinc-blende (B3) and hexagonal wurtzite (B4) polymorphs of MnS [54].

B1-MnS occurs naturally in the mineral alabandite, Fig. 1.2(a). It can be found in various locations worldwide as a minor mineral, primarily in epithermal sulfide veins for base metals, in low-temperature manganese deposits [55, 56], and in marine sediments [57, 58]. Alabandite is also present in certain kinds of meteorites such as E chondrites [61, 62] and related achondritic aubrites [63]. Additionally, it has been documented in some ureilites [64] and winonaites [65]. Alongside CaS and MgS, MnS is another sulfide compound that is believed to be present on the surface of Mercury [49, 50]. B4-MnS occurs in the mineral rambergite [66], Fig. 1.2(b). B3-MnS does not exist naturally but can be grown in the laboratory [67].

MnS is a transition metal (TM) compound, therefore it exhibits different properties than both CaS and MgS. Mn unpaired d-electrons (d^5 configuration) give rise to local magnetic moments at Mn sites, which order according to the type of the exchange interaction. The resulting magnetic ordering also affects the crystal structure. MnS is an example of Anderson's superexchange, similar to its TM

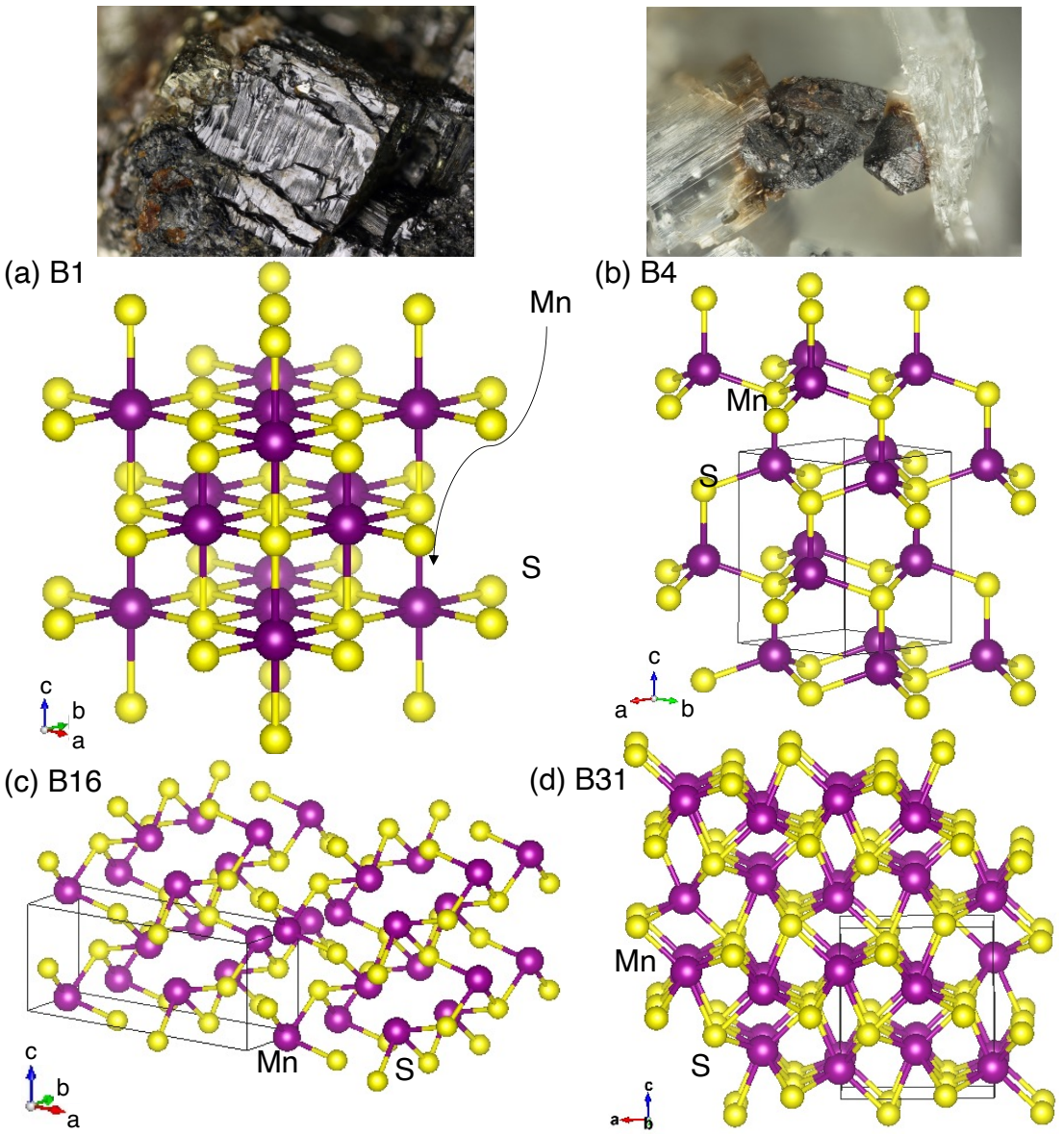

Figure 1.2: Crystal structures of MnS polymorphs and naturally occurring (a) B1-MnS [59] and (b) B4-MnS [60]. The crystal structures were generated by VESTA [20].

oxides counterparts (MnO, NiO, etc.) [68–71]. This type of interaction results in the antiferromagnetic order of the second type (AFM-II), i.e., sheets of ferromagnetically (FM) aligned moments couple antiferromagnetically along the [111] direction [54]. This arrangement causes a trigonal distortion, known as a magnetostriction effect [72]. The distortion disappears above 150 K when the system

undergoes a Neél transition from AFM to a paramagnetic (PM) state.

MnS is also considered a promising anode material in Li- and Na-ion batteries [73–77]. The main disadvantages of MnS are unfavorable electrical properties, a low rate of electron transfer, and significant changes in volume during Li^+/Na^+ uptake and release [76, 77]. However, these issues are not unique to MnS and plague various metal sulfides. A possible solution to mitigate them is to construct hollow/porous structures. Such structures contain numerous cavities, offering additional room for Li^+/Na^+ storage, which in turn boosts the capacity of electrode materials [78, 79]. In the case of MnS, coral-like MnS embedded in carbon and hollow-structured MnS-carbon nanocomposite powders have demonstrated an increased reversible capacity, good cycling stability as well as good specific capacity and rate capability [73–75]. Overall, MnS is a promising material, but further investigations about its properties are needed before it can emerge as a viable candidate for anode materials.

Lastly, a series of possible structural transitions under pressure have been reported for MnS [80–83]. X-ray diffraction and diamond-anvil cell (DAC) experiments describe a transition from the B1 to the orthorhombic GeS-type (B16) structure, Fig. 1.2(c), at about 7.2 GPa [80]. However, subsequent independent DAC experiments up to 21 GPa did not confirm this result [81], observing instead a transition from B1 to an unknown phase at approximately 26 GPa, which remained stable up to at least 46 GPa [82]. More recent DAC experiments reported the fabrication of MnS quenchable high-pressure nanostructures, identified as orthorhombic MnP-type (B31), Fig. 1.2(d). These MnS nanostructures exhibited a B1 to B31 transformation at a pressure of approximately 22 GPa, in agreement with previous findings in bulk MnS [83]. However, while the study identified B31-MnS as a stable nanostructure upon releasing pressure, it noted that in bulk, B31 returned

to B1-MnS. Therefore, the phase transformation sequence and whether there is another structural transition above 46 GPa need further investigation.

1.3 Perovskites: $LaTiO_3/SrTiO_3$ heterostructures

Perovskites are compounds with the general formula ABO_3. The perovskite crystal structure can be described as a network of corner-sharing octahedra BO_6^{2-} with the 12-coordinated A-cation [84], Fig. 1.3 (a). The A-cation is usually an alkaline-earth metal (Sr, Ca, Mg, etc.) or rare-earth element (La, Eu, etc.). The B-cation is often a TM element. The presence of d-electrons from TM elements, f-electrons from rare-earth elements, or a combination of the two is what determines a vast spectrum of electronic features characterizing perovskites.

Pure $LaAlO_3$ (LAO) and $SrTiO_3$ (STO) are both band insulators with no local

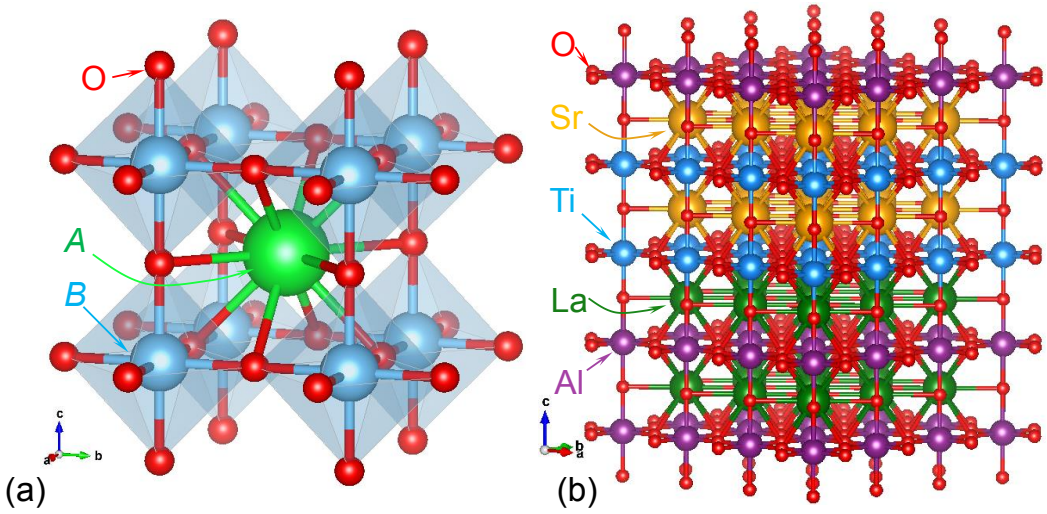

Figure 1.3: (a) A conventional perovskite crystal structure; and (b) heterostructure of $LaAlO_3/SrTiO_3$. The crystal structures were generated by VESTA [20].

magnetic moments [9]. However, the LAO/STO heterostructure, Fig. 1.3 (b), exhibits metallic behavior. This phenomenon is explained by the polar catastrophe mechanism [9, 10]. This catastrophe is characterized by an ionic polar

discontinuity at the interface between LAO and STO, which is compensated by a sudden electronic reconstruction at the interface, leading to unpaired $d-$ electrons. At the same time, experimentally LAO/STO heterostructures showed persistent magnetic signals [85, 86]. A net magnetization of 0.3-0.4 μB per interface Ti was determined from torque measurements in an external magnetic field [14]. However, measurements using superconducting quantum interference device (SQUID) found a state of local magnetic moments with null net magnetization [87]. These results were reconciled later by suggesting a model of a more complex spiral magnetic ordering [13].

Another crucial source of metallicity and magnetism in such TM perovskites is given by oxygen deficiency. In $SrTiO_{3-\delta}$, the oxygen vacancies effectively free up the Ti $3d$-electrons. These electrons occupy the Ti $3d_{xy}$ orbital, which is lowered with respect to the other e_g states because of the change in the local site symmetry at the Ti site [88, 89]. Oxygen vacancies are also an important factor in the interface physics of LAO/STO heterostructures. Here, they seem to stabilize the FM ordering [90]. However, this effect strongly depends on the concentration of oxygen vacancies. At low concentration, a Ruderman-Kittel-Kasuya-Yoshida (RKKY) coupling leads to FM ordering. Then, a double-exchange mechanism produces a different FM phase at larger concentrations. At intermediate concentrations, local AFM pairs lead to nearly absent net magnetization [91]. Understanding the intricate interplay of vacancy concentrations would allow the tailoring of magnetic ordering by defect manipulation for future materials functionalization.

1.4 Scope of the thesis

In this work, a combination of *ab initio* methods was used to model the structural, magnetic, and optical properties of CaS, MgS, and MnS. Additionally, the

effect of vacancy clustering in oxygen-deficient $LaAlO_3/SrTiO_3$ heterostructure was studied. In the case of sulfides, the main goal was to simulate the optical response in the infrared (IR) region. As a first step, the electronic structure of these systems was computed using a conventional DFT approach [1, 2]. CaS and MgS are relatively simple systems to model since they do not possess highly correlated d- or f-electrons. On the other hand, MnS has unpaired $3d$-electrons in its outer shell, which give rise to various magnetic properties. These $3d$-electrons add complexity to the modeling as various magnetic configurations have to be considered. DFT provides access to the ground state of the system, which is, strictly speaking, at 0 K. Nevertheless, its AFM configuration, present below MnS Neél temperature (T_N), and its PM state, observed above T_N, were both investigated. This PM state can be simulated as an assembly of randomly distributed magnetic moments, using the special quasirandom structure (SQS) technique [92].

In the IR region, the optical response is determined by atomic vibrations [93]. Atomic vibrational frequencies can be obtained using the finite displacement method (FDM) [94]. In FDM, DFT is used to calculate the total energy of a number of displaced configurations and then the forces acting on the atoms are extracted. These forces are used to set up a system of equations of motion for the atoms in the lattice to yield the resonance frequencies. However, in order to obtain an accurate optical response, it is necessary to go beyond the harmonic approximation and introduce various damping processes, i.e., phonon scatterings [93, 95, 96]. In this study, the three-phonon processes [95, 96] and scatterings due to isotopic disorder [97] were considered. After obtaining the harmonic frequencies as well as their dampings due to scattering processes, the dielectric function was calculated according to the Lorentz model. Knowing the dielectric function, and with it, various quantities that are directly measurable such as reflectivity, re-

flectance, emissivity, etc., can be derived. These properties are of interest for the upcoming BepiColombo mission [49, 50]. The interpretation of a planet's surface spectra that are detected remotely across a broad range of wavelengths is crucial to elucidate its building components [49]. The cooperation and combined efforts of simulations and experiments are imperative for a thorough understanding. For MnS, the DFT-SQS combination was also employed to provide new insights into the sequence of pressure-induced structural transitions observed at room temperature.

Finally, the clustering of oxygen vacancies in oxygen-deficient LAO/STO heterostructures was investigated. Several configurations with a pair of vacancies with varying distances between two vacancies were considered. The total energy was calculated using DFT, and the effect of various placements of vacancies on the local density of states (LDOS) and local magnetic moments at Ti ions was studied.

Chapter 2

Theoretical and computational methods

In this chapter, a detailed explanation of the computational methods used in this thesis is given. First, density functional theory (DFT) is explained in detail. This includes the Hohenberg-Kohn (HK) theorems as well as the variational derivation of the energy functional. Next, the Kohn-Sham (KS) equations are derived and various methods for solving them are discussed. Additionally, a concept of special quasirandom structures (SQS), which is used to model PM states of magnetic compounds is introduced. Lastly, the methods for modeling optical properties in different frequency regions are explained. The atomic units ($\hbar = m_e = e = 1$) are used throughout Sec. 2.1.

2.1 Density Functional Theory

Density functional theory (DFT) has become one of the most popular and successful quantum mechanical approaches in condensed matter. It has been employed to calculate binding energies of molecules, energy bands in solids, superconductiv-

ity, atoms in the focus of strong laser pulses, relativistic effects in materials with heavy elements and in atomic nuclei, classical liquids, and magnetic properties of alloys [98–100]. DFT applications in biology and geosciences have also become common [99, 101–103].

2.1.1 Hohenberg-Kohn approach

DFT takes a whole new approach to dealing with many-particle systems. It promotes the electron density from being just an observable to a key quantity in calculating the ground-state properties of a system. The electron density $\rho(\mathbf{r})$ is formally defined as [98]:

$$\rho(\mathbf{r}) = N \int \Psi(\mathbf{r}, \mathbf{r}_1, \ldots, \mathbf{r}_N)\Psi^*(\mathbf{r}, \mathbf{r}_1, \ldots, \mathbf{r}_N)d\mathbf{r}_1 d\mathbf{r}_2 ... d\mathbf{r}_N, \tag{2.1}$$

where $\Psi(\mathbf{r}, \mathbf{r}_1, \ldots, \mathbf{r}_N)$ is the true many-particle wave function, and N is the total number of particles. The foundations of DFT are the two Hohenberg-Kohn theorems [1] stated below:

Theorem 1 *The ground state density, $\rho_{GS}(\boldsymbol{r})$, determines the external potential $v(\boldsymbol{r})$ uniquely. Hence, given the ground state density $\rho_{GS}(\boldsymbol{r})$, it is possible, in principle, to calculate the corresponding true ground-state many-body wave function $\Psi_{GS}(\boldsymbol{r}_1, \ldots, \boldsymbol{r}_N)$.*

Any observable $\hat{O}$ is a functional of the ground-state wave function $\hat{O}[\Psi]$. The HK theorem establishes a one-to-one correspondence between the ground-state density $\rho_{GS}(\mathbf{r})$ and true ground-state wave function $\Psi_{GS}(\mathbf{r}_1, \ldots, \mathbf{r}_N)$. Thus, any observable is also a functional of the ground-state density $\hat{O}[\rho_{GS}(\mathbf{r})]$ [98].

Basically, the first HK theorem (HK-I) gives a new quantity, which depends only

on three spatial coordinates, to calculate the ground-state properties, which is much simpler than the real many-particle wave function. However, it does not specify how exactly to do it in practice. A way to obtain some definite expressions that can be used in the calculation is given by the second Hohenberg-Kohn (HK-II) theorem [1]:

Theorem 2 *The variational minimum of the energy of a system is the exact ground-state energy, i.e.,* $\frac{\delta E[\rho(\boldsymbol{r})]}{\delta \rho_{GS}(\boldsymbol{r})} = E_{GS}$

The HK-II restates a simple quantum mechanical variational principle with the only difference that one is able to obtain the exact ground state.

The total energy of a system as a functional of the electron density can be written as [1]:

$$E[\rho(\mathbf{r})] = T[\rho(\mathbf{r})] + U[\rho(\mathbf{r})], \tag{2.2}$$

where $T[\rho(\mathbf{r})]$ and $U[\rho(\mathbf{r})]$ are the kinetic and potential energy of the system, respectively. The term $U[\rho(\mathbf{r})]$ contains both the electron-electron interaction and the interaction with the external potential. The potential energy term can be split into three terms [1]:

$$U[\rho(\mathbf{r})] = E_H[\rho(\mathbf{r})] + E_{xc}[\rho(\mathbf{r})] + \int v_{ext}(\mathbf{r})\rho(\mathbf{r})d\mathbf{r}, \tag{2.3}$$

with the Hartree energy E_H given by:

$$E_H = \int \frac{\rho(\mathbf{r})\rho(\mathbf{r}')}{|\mathbf{r} - \mathbf{r}'|} d\mathbf{r}d\mathbf{r}', \tag{2.4}$$

where the Hartree term is the classical Coulomb electron-electron repulsive interaction. The exchange-correlation term E_{xc} can be interpreted as all of the higher-order perturbations to the electron-electron interactions. The general form

of E_{xc} does not exist, and further approximations are required. Working out the exchange-correlation contributions is a highly non-trivial task [98–100]. The last term in Eq. (2.3) is the potential energy due to the interaction of the electron density with the external potential $v_{ext}(\mathbf{r})$.

Using the variational principle (HK-II) and the method of Lagrange multipliers, with the constraint of a constant particle number,

$$\int \rho(\mathbf{r})d\mathbf{r} = N, \tag{2.5}$$

the variation of the energy functional in Eq. (2.2) with respect to $\rho(\mathbf{r})$ gives [98]:

$$\begin{aligned}\frac{\delta E[\rho]}{\delta\rho(\mathbf{r})} &= \frac{\delta T[\rho]}{\delta\rho(\mathbf{r})} + \frac{\delta}{\delta\rho(\mathbf{r})}\int\frac{\rho(\mathbf{r})\rho(\mathbf{r}')}{|\mathbf{r}-\mathbf{r}'|}d\mathbf{r}d\mathbf{r}' + \frac{\delta}{\delta\rho(\mathbf{r})}\int v_{ext}(\mathbf{r})\rho(\mathbf{r})d\mathbf{r} \\ &\quad + \frac{\delta E_{xc}[\rho]}{\delta\rho(\mathbf{r})} - \mu(\int\rho(\mathbf{r})d\mathbf{r} - N) = 0; \\ \frac{\delta E[\rho]}{\delta\rho(\mathbf{r})} &= \frac{\delta T[\rho]}{\delta\rho(\mathbf{r})} + \int\frac{\rho(\mathbf{r}')}{|\mathbf{r}-\mathbf{r}'|}d\mathbf{r}' + v_{ext}(\mathbf{r}) + \frac{\delta E_{xc}[\rho]}{\delta\rho(\mathbf{r})} - \mu = 0,\end{aligned} \tag{2.6}$$

where μ is the Lagrange multiplier. Eq. (2.6) states the general problem that needs to be solved. However, $T[\rho]$ and $E_{xc}[\rho]$ still need to be determined and different schemes can be followed.

For example, in the Thomas-Fermi approach [104–106], one assumes that $\rho(\mathbf{r})$ corresponds to the density of an electron gas, and the kinetic energy $T[\rho]$ is defined by

$$T[\rho] = C_k\int[\rho(\mathbf{r})]^{5/3}d\mathbf{r}, \tag{2.7}$$

where C_k is a normalization constant. Inserting (2.7) into (2.6) and ignoring the exchange-correlation effects, one obtains:

$$\frac{5}{3}C_k\rho(\mathbf{r})^{2/3} + \int\frac{\rho(\mathbf{r}')}{|\mathbf{r}-\mathbf{r}'|}d\mathbf{r}' + v_{ext} - \mu = 0, \tag{2.8}$$

which is the well-known Thomas-Fermi (TF) equation. However, there are several deficiencies in this model. Firstly, the charge density turns out to be infinite at the nucleus. Secondly, the TF theory does not predict atoms binding to form molecules or solids. Finally, another serious problem is the lack of a shell structure in the TF atom, which means that the periodic variation of many properties with changing atomic numbers cannot be reproduced [98, 100].

2.1.2 The Kohn-Sham scheme

Although Eq. (2.6) is formally exact and should be able to yield the true ground state of a system, it is not very practical. The main problem is the lack of a general expression for the kinetic energy as a functional of the electron density. Kohn and Sham suggested an elegant alternative route to search for the ground-state density [2]. Their core idea was to assume that the ground state of the interacting system can be described by that of some auxiliary system of non-interacting particles. The KS energy functional is defined as[1] [1, 2]:

$$E_{KS}[\rho(\mathbf{r})] = T_0[\rho(\mathbf{r})] + E_H[\rho(\mathbf{r})] + E_{xc}[\rho(\mathbf{r})] + \int v_{ext}(\mathbf{r})\rho(\mathbf{r})d\mathbf{r} + \sum_{A\neq B} \frac{Z_A Z_B}{|\mathbf{R}_A - \mathbf{R}_B|}, \tag{2.9}$$

where $T_0[\rho(\mathbf{r})]$ is the kinetic energy of the non-interacting particle system and $\mathbf{R}_{A(B)}$ denotes the position of atom $A(B)$ with the respective nuclei charge $Z_{A(B)}$. The last term in Eq.(2.9) is the nuclei-nuclei repulsion contribution to the total

[1] One can also think of it as a decomposition of the total kinetic energy into non-interacting and correlated parts: $T_{tot}[\rho] = T_0[\rho] + T_c[\rho]$. $T_0[\rho]$ corresponds to a non-interacting electron gas. $T_c[\rho]$ is a pure correlation effect that can be treated perturbatively together with v_{xc}

energy. The electron density in this case is given by [2]:

$$\rho(\mathbf{r}) = \sum_j |\psi_j(\mathbf{r})|^2, \tag{2.10}$$

where ψ_j are single-electron orbitals. The KS kinetic energy T_0 is different from the true kinetic energy, but it is of comparable magnitude [98] and is given by:

$$T_0 = -\frac{1}{2}\sum_j \int \psi_j^*(\mathbf{r})\nabla^2\psi_j(\mathbf{r})d\mathbf{r}. \tag{2.11}$$

Here, the density dependence is implicit through Eq. (2.10), and the constant particle number constraint is calculated as:

$$\sum_j \int |\psi_j(\mathbf{r})|^2 d\mathbf{r} = N. \tag{2.12}$$

The variation of Eq. (2.9) with respect to single-electron orbitals $\psi_j(\mathbf{r})$, under the constraint in Eq. (2.12), produces [107]:

$$\begin{aligned}\frac{\delta E_{KS}[\rho(\mathbf{r})]}{\delta\psi_j^*(\mathbf{r})} = \frac{\delta T_0[\rho(\mathbf{r})]}{\delta\psi_j^*(\mathbf{r})} + \left[\frac{\delta E_H[\rho(\mathbf{r})]}{\delta\rho(\mathbf{r})} + \frac{\delta E_{xc}[\rho(\mathbf{r})]}{\delta\rho(\mathbf{r})} + \frac{\delta\int v_{ext}(\mathbf{r})\rho(\mathbf{r})d\mathbf{r}}{\delta\rho(\mathbf{r})}\right]\frac{\delta\rho(\mathbf{r})}{\delta\psi_j^*(\mathbf{r})} - \\ -\frac{\delta}{\delta\rho(\mathbf{r})}\Big(\sum_j \mu_j \int \rho(\mathbf{r})d\mathbf{r} - N\Big)\frac{\delta\rho(\mathbf{r})}{\delta\psi_j^*(\mathbf{r})} + \frac{\delta}{\delta\rho(\mathbf{r})}\sum_{A\neq B}\frac{Z_A Z_B}{|\mathbf{R}_A - \mathbf{R}_B|} = 0.\end{aligned} \tag{2.13}$$

The last term in Eq. (2.13) does not contain the electron density and its variation is, therefore, equal to zero. Using the expressions

$$\frac{\delta T_0[\rho(\mathbf{r})]}{\delta\psi_j^*(\mathbf{r})} = -\frac{1}{2}\sum_j \nabla^2\psi_j(\mathbf{r}), \quad \text{and} \quad \frac{\delta\rho(\mathbf{r})}{\delta\psi_j^*(\mathbf{r})} = \psi_j(\mathbf{r}), \tag{2.14}$$

Eq. (2.13) can be transformed into [107],

$$\left\{\nabla^2 + V_{KS}(\mathbf{r})\right\}\psi_j(\mathbf{r}) = \mu_j\psi_j(\mathbf{r}), \tag{2.15}$$

where the KS potential $V_{KS}(\mathbf{r})$ is defined as:

$$V_{KS}(\mathbf{r}) = \int \frac{\rho(\mathbf{r}')}{|\mathbf{r}-\mathbf{r}'|}d\mathbf{r}' + v_{ext}(\mathbf{r}) + \frac{\delta E_{xc}[\rho(\mathbf{r})]}{\delta\rho(\mathbf{r})}. \tag{2.16}$$

The Lagrange multipliers μ in Eq. (2.13) are now understood to be the eigenvalues of the single-particle Schrödinger equation, Eq. (2.15). Renaming them by $\mu_j \rightarrow \varepsilon_j$, one finally obtains:

$$\left\{\nabla^2 + V_{KS}(\mathbf{r})\right\}\psi_j(\mathbf{r}) = \varepsilon_j\psi_j(\mathbf{r}). \tag{2.17}$$

Eq. (2.17) is actually a system of equations for a set of single-particle orbitals $\psi_j(\mathbf{r})$. They are known as the Kohn-Sham equations, which replace the problem of minimizing $E[\rho(\mathbf{r})]$ by that of solving a system of single-particle Schrödinger equations for an auxiliary system of non-interacting particles [2]. Treating the kinetic energy exactly removes many of the deficiencies of the Thomas-Fermi approach, such as the lack of a shell structure of atoms or the absence of chemical bonding in molecules and solids [98, 100].

Eq. (2.17) are solved self-consistently, Fig. 2.1 [107], starting with an appropriate guess for the electron density $\rho(\mathbf{r})$. The effective potential is constructed using Eq. (2.16), and then used to compute a set of Kohn-Sham orbitals $\psi_j(\mathbf{r})$ with Eq. (2.10). A new density is calculated and the self-consistent cycle is repeated. This process continues until convergence in energy and density is achieved. Numerous convergence-accelerating algorithms (such as mixing of old and new effec-

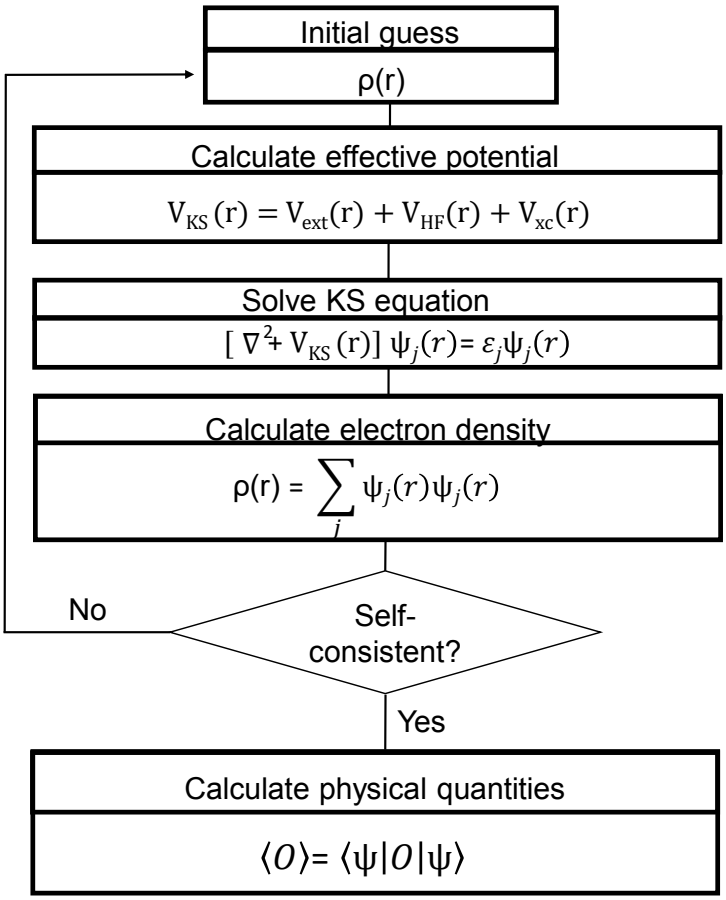

Figure 2.1: DFT self-consistent loop [107]. The terms for the effective potential V_{KS} correspond to the respective terms in Eq. (2.16).

tive potentials) are used to solve the KS equations more efficiently [108].

Before proceeding with the approximations to describe the exchange-correlation effects and methods for solving Kohn-Sham equations, a few remarks about DFT and the Kohn-Sham scheme need to be stated. DFT gives access only to the ground state of a system [1, 2, 98, 100]. Even though the HK theorem does not exclude the possibility of mapping to excited states, in practice such a scheme has not been developed yet. In the KS equations, the eigenenergies do not bear any physical meaning in the sense that they are not the energies of the original system [107]. The KS energies correspond to the eigenstates of the auxiliary

non-interacting system, which can be used to construct physically valid quantities. Nevertheless, the KS approach has proven to be a quite good starting point, owing its success to the possibility of the inclusion of correlation effects.

2.1.3 Exchange-correlation energy

The total energy within the KS scheme given by Eq. (2.9) can be written explicitly as [1, 2]:

$$E_{tot} = -\frac{1}{2}\sum_i \int \psi_i(\mathbf{r})\nabla^2\psi_i(\mathbf{r})d\mathbf{r} + E_{xc} + \frac{1}{2}\int \frac{\rho(\mathbf{r})\rho(\mathbf{r}')}{|\mathbf{r}-\mathbf{r}'|}d\mathbf{r}d\mathbf{r}' - \sum_A \int \frac{Z_A}{|\mathbf{r}-\mathbf{R}_A|}\rho(\mathbf{r})d\mathbf{r} + \sum_{A\neq B}\frac{Z_A Z_B}{|\mathbf{R}_A - \mathbf{R}_B|}. \tag{2.18}$$

The only contribution which remains unknown is the exchange-correlation energy E_{xc}. The exchange-correlation term is generally unknown, but reasonable approximations can be made as a local or semi-local functional of the density [109].

Local Spin Density Approximation

The simplest functionals are obtained within the local density approximation (LDA) or more generally the local spin-density approximation (LSDA). The spin-dependent exchange-correlation (XC) energy can be separated into exchange and correlation parts [107]:

$$E_{xc}[\rho_\uparrow, \rho_\downarrow] = E_x[\rho_\uparrow, \rho_\downarrow] + E_c[\rho_\uparrow, \rho_\downarrow] = \int \epsilon_x[\rho_\uparrow, \rho_\downarrow]\rho(\mathbf{r})d\mathbf{r} + \int \epsilon_c[\rho_\uparrow, \rho_\downarrow]\rho(\mathbf{r})d\mathbf{r}, \tag{2.19}$$

where ϵ_x and ϵ_c are the exchange and correlation energies per particle, respectively, and the total density ρ is the sum of its spin-polarized $\rho_\uparrow$, $\rho_\downarrow$ parts. Assuming a homogeneous unpolarized ($\rho_\uparrow = \rho_\downarrow$) electron gas, the exchange energy per electron

is given by [110]:

$$\epsilon_x^{LDA}[\rho] = -\frac{3}{2}\Big(\frac{3}{\pi}\Big)^{1/3}\rho^{4/3}(\mathbf{r}). \tag{2.20}$$

For the correlation energy $\epsilon_c[\rho]$, a widely used approximation within LSDA, is the parametrization given by Perdew and Zunger [111], using Monte Carlo simulation data obtained for homogeneous electron gas by Ceperley and Adler [112]. Another commonly used approximation for $\epsilon_c[\rho]$ is an analytic representation, which was proposed by Perdew and Wang [113]. Despite its conceptual simplicity, LSDA successfully describes the ground-state properties of multiple physical systems. For example, it accurately predicts the ground-state geometries of various types of molecules, from simple diatomic systems to infinite chains in polymers. LSDA is also reliable in handling the equilibrium geometries of many extended systems [98]. However, its main drawback is the tendency to overestimate the bond strength in solids. As a result, LSDA calculated lattice parameters are underestimated, cohesive energies are overestimated and band gaps are narrower than their measured counterparts [99].

Generalized Gradient Approximantion

A step further to improve LSDA is the generalized gradient approximation (GGA). In this scheme, for a slowly varying density $\rho(\mathbf{r})$, the exchange-correlation energy depends on the gradient of $\rho(\mathbf{r})$ [114–118]:

$$E_{xc}^{GGA} = \int \epsilon_{xc}(\rho(\mathbf{r}), \nabla\rho(\mathbf{r}))\rho(\mathbf{r})d\mathbf{r}, \tag{2.21}$$

where $\epsilon_{xc}(\rho(\mathbf{r}), \nabla\rho(\mathbf{r}))$ is some general function. Many parameterizations for ϵ_{xc} are known, but one of the most used was given by Perdew, Burke, and Ernzerhof

(PBE) [119]. In this PBE parameterization, the exchange energy is given by

$$\epsilon_x^{GGA} = \epsilon_x^{LDA}(\rho) F_x^{GGA}(\rho, \nabla\rho), \tag{2.22}$$

where, the function $F_x^{GGA}(\rho, \nabla\rho)$ is a dimensionless enhancement factor, that depends on the density and its gradient, and effectively indicates how much exchange is enhanced over LSDA value. Similarly, GGA correlation energy is expressed as a sum of the LSDA correlation energy ϵ_c^{LDA} and a function $H(\rho, \nabla\rho)$ [119]:

$$\epsilon_c^{GGA} = \epsilon_c^{LDA}(\rho) + H(\rho, \nabla\rho). \tag{2.23}$$

H is usually given by a gradient expansion, with the lowest terms being the most significant. For large $\nabla\rho$ the magnitude of correlation decreases as large gradients are connected to strong confining potentials that reduce the effect of interactions [119].

The GGA method usually improves the overbinding produced by the LSDA approach. However, it can sometimes go too far in the other direction, resulting in an overcorrection. For example, LDA lattice parameters tend to be underestimated by about 1%, while the PBE method usually overestimates them by a similar amount [120]. Additionally, properties such as bulk moduli, phonon frequencies, and magnetic moments, which are sensitive to the lattice constant, might also be overcorrected by the GGA [99, 120, 121]. It should be noted that LDA often fails to accurately predict the ground state of magnetic transition metals, while the GGA succeeds in doing so [99]. For example, within LDA Fe turns out to be hexagonal and nonmagnetic instead of body-centered cubic and ferromagnetic [122], whereas Cr is predicted to be nonmagnetic instead of antiferromagnetic [123]. An additional advancement in the accuracy of PBE is the

revised version of GGA/PBE for solids, often referred to as PBEsol [124]. The PBEsol exchange-correlation functional is conceptually identical to PBE, but the enhancement in exchange F_x and the additional correlation H are modified to describe solids more correctly.

Meta-GGA and Hybrid functionals

Next up the ladder of the hierarchy of the exchange-correlation functionals are the Meta-GGA and hybrid functionals. In the meta-GGA, in addition to local density and its gradient, the exchange-correlation functional depends also on the local kinetic energy $\tau(\mathbf{r})$ [99]:

$$E_{xc}^{meta-GGA} = \int \epsilon_{xc}^{meta-GGA}(\rho(\mathbf{r}), \nabla\rho(\mathbf{r}), \tau(\mathbf{r}))d\mathbf{r}, \tag{2.24}$$

with

$$\tau(\mathbf{r}) = \frac{1}{2}\sum_i |\nabla\psi_i(\mathbf{r})|^2, \tag{2.25}$$

and i running over all occupied KS orbitals. In general, meta-GGA schemes in the literature can be divided into two categories [99]: semi-empirical parametrized functionals [125] and those, that follow the GGA/PBE philosophy of eliminating adjustable parameters [126–129]. Practically, the meta-GGA offers a significant improvement for atomization energies in molecules [130], whilst for lattice constants and bulk moduli in solids its performance is similar to GGA [128, 131]. The computational cost of meta-GGA is slightly higher than that of LSDA and GGA.

Hybrid functionals combine nonlocal Hartree-Fock exchange with local or semilocal DFT exchange in a specific ratio [99, 132, 133]:

$$E_{xc}^{hyb} = \alpha E_x^{HF} + (1-\alpha)E_x^{GGA} + E_c^{GGA}, \tag{2.26}$$

where α is the mixing ratio. The idea behind hybrid functionals is to address the limitations of both DFT and HF methods. DFT tends to underestimate band gaps, whereas HF overestimates them. By blending these two methods, it is possible to obtain more accurate predictions for band gaps, as well as improved total energies and geometries [99].

2.1.4 DFT+U

DFT+U is a scheme designed to address highly correlated d- and f-electrons in systems by introducing the Hubbard interaction potential U. Similarly to hybrid functionals, DFT+U aims to solve the underestimation of the DFT band gap but at a lower computational cost than in a hybrid scheme.

As it was discussed before, the main issue is the exchange-correlation part of the effective potential, which needs to be approximated. Unfortunately, none of the known approximations (LSDA, GGA, etc.) seem to be able to fully resolve the problem of localization of d- and f-electrons in solids. Well-known correlated systems are the TM oxides (MnO, NiO, etc.) [134, 135] for which conventional DFT theory predicts metallic behavior when in reality they are insulators. The cause of the electron localization is known to be due to strong electron-electron repulsion [134].

DFT+U can be understood in terms of the tight-binding (TB) model [136]. The KS scheme recasts a many-body interacting problem onto a non-interacting single-particle problem, with all interactions included in the effective potential $V_{KS}(\mathbf{r})$. The Hamiltonian for this non-interacting system with the addition of a Hubbard interaction can be written (using second quantization notation [137]) as [138]:

$$H = \sum_{i,j,m,m',\sigma} \left(t_{ij,\sigma}^{m,m'} c_{im,\sigma}^{\dagger} c_{jm',\sigma} + h.c. \right) + U \sum_{i,m'',\sigma} n_{i,m''}^{\sigma} n_{i,m''}^{-\sigma}, \tag{2.27}$$

where $c^{\dagger}_{im,\sigma}(c_{jm',\sigma})$ is an operator that creates (destroys) an electron at site $i(j)$, orbital $m(m')$ with spin σ, and $t^{m,m'}_{ij,\sigma}$ are the hopping integrals. The spin index σ takes on $\uparrow$ (spin up) and $\downarrow$ (spin down) values, i.e., $\sigma = \{\uparrow, \downarrow\}$. U is the Hubbard-like interaction [138], and $n^{\sigma}_{i,m} = c^{\dagger}_{i,m,\sigma}c_{i,m,\sigma}$ is the number operator. In this Hubbard Hamiltonian given by Eq. (2.27), the hopping process from one atomic site to the other has amplitude t in the single-particle term. The two-particle Coulomb repulsion term is proportional to U, and occurs only on the same atomic site. To obtain the total energy of the system using Eq. (2.27), the interaction term needs to be decoupled using a mean-field (MF) approximation [137]. In this approach, the density operators deviate only slightly from their average values: $\langle n^{\sigma}_{i,m}\rangle$ and $\langle n^{-\sigma}_{i,m}\rangle$. Defining the deviation operators as:

$$\tilde{n}^{\sigma}_{i,m} = n^{\sigma}_{i,m} - \langle n^{\sigma}_{i,m}\rangle, \qquad \tilde{n}^{-\sigma}_{i,m} = n^{-\sigma}_{i,m} - \langle n^{-\sigma}_{i,m}\rangle, \tag{2.28}$$

and then substituting them into Eq. (2.27), one obtains [137]:

$$H_{MF} = H_0 + V_{MF} + U \sum_{i,m'',\sigma} \tilde{n}^{\sigma}_{i,m''}\tilde{n}^{-\sigma}_{i,m''}, \tag{2.29}$$

where H_0 is the single particle term of Eq. (2.27), and

$$V_{MF} = U \sum_{i,m'',\sigma} \Big(n^{\sigma}_{i,m''}\langle n^{-\sigma}_{i,m''}\rangle + n^{-\sigma}_{i,m''}\langle n^{\sigma}_{i,m''}\rangle - \langle n^{\sigma}_{i,m''}\rangle\langle n^{-\sigma}_{i,m''}\rangle \Big). \tag{2.30}$$

For small deviations, the last term in Eq. (2.29) can be neglected. The product $\langle n^{\sigma}_{i,m''}\rangle\langle n^{-\sigma}_{i,m''}\rangle$ in Eq. (2.30) is a constant, and can be set to zero by shifting the energy. Therefore, the final form of the Hubbard Hamiltonian within the MF

approximation is [137]:

$$H_{MF} = \sum_{i,j,m,m',\sigma} \left(t_{ij,\sigma}^{m,m'} c_{im,\sigma}^{\dagger} c_{jm',\sigma} + h.c. \right) + U \sum_{i,m'',\sigma} \left(n_{i,m''}^{\sigma} \langle n_{i,m''}^{-\sigma} \rangle + n_{i,m''}^{-\sigma} \langle n_{i,m''}^{\sigma} \rangle \right). \tag{2.31}$$

The MF-decoupled interaction adds $U\langle n_{i,m''}^{\sigma} \rangle$ to the on-site energy, which is reflected in the shift of the corresponding bands of the opposite spin by the same amount.

This effect of electron-electron interaction at the mean-field level on the band structure was first introduced by Anisimov *et al.* [136]. Here, the single-band Hamiltonian H_{MF} for the interaction is slightly different than Eq. (2.31):

$$H_{int}^{MF} = \frac{1}{2} \sum_{i} \Big\{ U[n_i(n_i^{\uparrow} + n_i^{\downarrow}) - m_i(n_i^{\uparrow} - n_i^{\downarrow})] - \frac{1}{4} U(n_i^2 - m_i^2) \Big\}, \tag{2.32}$$

where the average occupancy and moment are defined as $n_i = \langle n_i^{\uparrow} \rangle + \langle n_i^{\downarrow} \rangle$ and $m_i = \langle n_i^{\uparrow} \rangle - \langle n_i^{\downarrow} \rangle$, respectively. Then, the following multi-band energy functional can be formulated [136]:

$$\begin{aligned} E^U[n_i] = E^{DFT}[\rho(\mathbf{r})] + \frac{1}{2} \sum_{m,m',\sigma} U(n_{i,m}^{\sigma} - n^0)(n_{i,m'}^{-\sigma} - n^0) \\ + \frac{1}{2} \sum_{m,m',\sigma} (U - J)(n_{i,m}^{\sigma} - n^0)(n_{i,m'}^{\sigma} - n^0), \end{aligned} \tag{2.33}$$

where J is the Hund's coupling and n^0 is the average occupancy of orbitals m. This expression provides a noteworthy enhancement over standard DFT calculations for electron-electron correlations of localized orbitals within delocalized electron systems. The DFT+U method is an upgraded approximation for electron-removal and electron-addition spectra, and it is a crucial tool for interpreting many spectroscopy experiments [139]. Additionally, DFT+U requires only a minor increase in computational effort in comparison to standard DFT. This feature is partic-

ularly valuable in materials science where efficient formulations are essential for handling increasingly complex systems [139, 140].

Rotational invariance

One significant drawback of Eq. (2.33) is the definition of $E^U[n_i]$ with respect to a particular single-particle basis set [136]. A more general and basis-independent formulation of the DFT+U method was given by Lichtenstein [141, 142]. It departs from the assumption that the electron-electron interaction mostly retains its atomic nature. Therefore, one only needs to identify the regions of space where the atomic characteristics of the electronic states are preserved, i.e., regions around the atoms[2]. The generalized DFT+U functional can be formulated then in terms of the elements of the on-site density matrix defined as [143]:

$$n^{\sigma}_{m,m'} = \sum_{\nu,\mathbf{k}} f^{\sigma}_{\nu,\mathbf{k}} \left\langle \psi^{\sigma}_{\nu,k} \middle| \phi_m \right\rangle \left\langle \phi_{m'} \middle| \psi^{\sigma}_{\nu,\mathbf{k}} \right\rangle , \tag{2.34}$$

where $\left|\psi^{\sigma}_{\nu,\mathbf{k}}\right\rangle$ are the KS orbitals with band index ν, wavevector $\mathbf{k}$ and spin σ with occupation $f^{\sigma}_{\nu,\mathbf{k}}$, and $\{|\phi_m\rangle\}$ is a set of localized orbitals, e.g., atomic states. The energy functional suggested by Lichtenstein is given by [141]:

$$E[\rho(\mathbf{r}), \{n^{\sigma}\}] = E^{DFT}[\rho(\mathbf{r})] + E^{U}[\{n^{\sigma}\}] - E_{dc}[n^{\sigma}_{tot}]. \tag{2.35}$$

Here, $\{n^{\sigma}\}$ denotes the elements of the on-site density matrix with spin σ, and $n^{\sigma}_{tot} = \mathrm{Tr}(n^{\sigma}_{m,m'})$. The first term in Eq. (2.35) corresponds to the energy functional within conventional DFT approximations (LDA or GGA) as discussed in

[2]These regions are defined slightly differently depending on the basis set used to solve the KS equations. In various muffin-tin orbital (LMTO, EMTO, etc.) methods, these regions are referred to as atomic spheres. In plane-wave methods, these are known as augmentation regions.

Sec. 2.1.3. The Hubbard term $E^U[\{n^\sigma\}]$ is defined as [141]:

$$E^U[\{n^\sigma\}] = \frac{1}{2}\sum_{\{n^\sigma\}}\Big(\langle m,m''|\,V_{ee}\,|m',m'''\rangle\, n^\sigma_{m,m'}n^{-\sigma}_{m'',m'''} + \\ + \big(\langle m,m''|\,V_{ee}\,|m',m'''\rangle - \langle m,m''|\,V_{ee}\,|m''',m'\rangle\big)n^\sigma_{m,m'}n^\sigma_{m'',m'''}\Big). \tag{2.36}$$

The matrix elements in Eq. (2.36) are the screened Coulomb interactions among electrons. They can be expressed in terms of complex spherical harmonics Y and effective Slater integrals F^k as [144]:

$$\langle m,m''|\,V_{ee}\,|m',m'''\rangle = \frac{4\pi}{2k+1}\sum_k\sum_{q=-k}^{k}\langle lm|\,Y_{kq}\,|km'\rangle\,\langle lm''|\,Y^*_{kq}\,|km'''\rangle\,F^k, \tag{2.37}$$

where $0 \le k \le 2l$, with l being the orbital quantum number. The last term in Eq. (2.35) corrects for double counting and is given by:

$$E_{dc}[n^\sigma_{tot}] = \frac{1}{2}Un(n-1) - \frac{1}{2}J[n^\uparrow_{tot}(n^\uparrow_{tot}-1) + n^\downarrow_{tot}(n^\downarrow_{tot}-1)], \tag{2.38}$$

where $n = n^\uparrow_{tot} + n^\downarrow_{tot}$. Eq. (2.35) is rotationally invariant because the interaction parameters (matrix elements) in Eq. (2.36) transform as quadruplets of localized wavefunctions, which compensate any variations in the corresponding product of occupations [143]. At the same time the double counting correction given by Eq. (2.38) depends on the trace of the on-site density matrix, which is basis-independent. In practical applications, the interaction parameters of Eq. (2.36) are often treated as adjustable parameters to match experimental observations for specific properties such as magnetic moment, equilibrium volume, or band gap. The effective on-site Coulomb and exchange parameters denoted as U and J respectively, are typically used to specify these parameters. Alternatively, U and J can also be extracted from constrained-DFT calculations [145, 146].

The rotationally invariant formulation given by Eq. (2.36) is the most complete formulation of DFT+U, featuring electronically orbital-dependent interactions [143]. However, a simplified version of the Hubbard correction, proposed by Dudarev *et al.* [147], is also widely used in practice. This simpler form considers only the lowest order Slater integrals (F^0) and neglects all higher-order terms ($F^2 = F^4 = F^6 = 0$) [143]. Under these conditions the total energy functional given by Eq. (2.36) becomes [143, 147]:

$$\begin{aligned} E_{DFT+U} &= E_{DFT} + \frac{U_{eff}}{2} \sum_{\sigma} \Big[\Big(\sum_{m} n^{\sigma}_{m,m} \Big) - \Big(\sum_{m,m'} n^{\sigma}_{m,m'} n^{\sigma}_{m',m,} \Big) \Big], \\ &= \frac{U_{eff}}{2} \sum_{\sigma} Tr \big[n^{\sigma}_{m,m'} (\mathbf{1} - n^{\sigma}_{m,m'}) \big], \\ &= E_{DFT} + \frac{U_{eff}}{2} \sum_{\sigma} n^{\sigma}_{tot} (1 - n^{\sigma}_{tot}), \end{aligned} \tag{2.39}$$

where $U_{eff} = U - J$. It should be noted that the functional of Eq. (2.39) depends on the trace of the on-site density matrix, and, therefore, it is also basis-independent. This formulation connects Lichtensten's and Anisimov's functionals, Eq. (2.35) and Eq. (2.33), keeping the rotational invariance of the former and the simplicity of the latter [147]. Several studies have successfully employed the simplified form of the Hubbard correction, Eq. (2.39), which typically produces comparable results to the fully rotationally invariant version, Eq (2.35) for many materials [143]. However, some studies have shown that the explicit inclusion of the Hund's coupling J can be critical for describing systems with non-collinear magnetism [148, 149], or capturing correlation effects in multi-band metals [150].

2.1.5 Methods for solving the Kohn-Sham equations

The Kohn-Sham equations, Eq. (2.17), are used to describe a system with multiple electrons through a density built from independent-particle wave functions. These

wave functions can be expressed as a linear combination of predetermined basis functions, resulting in a matrix equation that, in principle, can be solved exactly. Developing numerical methods that are both accurate and efficient for solving KS equations is a major challenge in computational materials science. The solutions derived from the KS equations should be the same, independently of the form of the basis functions, as long as the basis set is complete [151]. The accuracy is particularly important when comparing results from different approximations used for the exchange-correlation functionals. Thus, the two main considerations for solving the KS equations are: 1) the choice of basis functions for the expansion of the KS orbitals ψ_j and 2) the approximation used for the effective potential, V_{KS} in Eq. (2.17). These two factors determine different implementations of DFT. A short summary of existing methods is given below. The projector-augmented wave method, which is used in this work, is explained in more detail.

Augmented plane waves (APW)

The central issue that all methods try to overcome is the different behavior of the wave functions of real materials in different space regions. In the bonding region, they show a rather smooth behavior, whereas close to the nuclei they oscillate rapidly due to the large attractive potential [152]. A very natural basis for calculating single-electron wave functions in solids is that of the plane waves (PW) corresponding to Bloch functions labeled by the **k**-vector of the first Brillouin zone (BZ) [153]. However, this basis is highly inefficient in describing rapidly varying wave functions close to the nuclei [154]. Therefore, a strategy is to divide the space into two distinct parts, namely the atom-centered sphere and the interstitial region outside of the atomic sphere. The single-electron wave functions are constructed separately for these regions and then matched at the boundary between them.

As mentioned before, a PW basis is not particularly suitable due to its inability to adequately describe rapid oscillations of the wave functions close to the nuclei. A possible solution is to improve this basis set with modified plane waves. The main idea, originally stated by Slater [155], is to keep the plane wave description in the interstitial region but to augment the wave functions inside the atomic sphere. In this augmented plane waves (APW) method, the basis functions are given by [154]:

$$\phi_{\mathbf{G}}(\mathbf{r}) = \begin{cases} \sum_L a_L^{\alpha\mathbf{G}} u_l^{\alpha}(r', \epsilon) Y_L(\theta, \varphi), & r' < R_\alpha, \\ \Omega^{-1/2} \exp(i(\mathbf{k} + \mathbf{G})\mathbf{r}), & r \in I, \end{cases} \tag{2.40}$$

where $u_l^{\alpha}(r', \epsilon)$ is the numerical solution to the radial Schrödinger equation at energy ϵ, $Y_L(\theta, \varphi)$ is the spherical harmonic, L is short for orbital (l) and magnetic (m) quantum numbers, Ω is the unit cell volume, $\mathbf{k}$ is a wave vector in the irreducible Brillouin zone (IBZ) and $\mathbf{G}$ is a reciprocal lattice vector. The coefficients $a_L^{\alpha\mathbf{G}}$ are chosen in such a way that the atomic functions for all L components match in value the PW at the boundary between the atomic sphere of radius R_α and the interstitial region I. The KS orbitals are then expressed as linear combinations of APWs $\phi_{\mathbf{G}}(\mathbf{r})$. Inside the atomic sphere, the KS orbital eigenvalue ε_i in Eq. (2.17) has to be equal to the energy ϵ of the basis function [154]. This means that for every KS eigenenergy ε_i a different energy-dependent basis set must be found, leading to a non-linear eigenvalue problem. Because of its high computational cost, the APW scheme is not very practical and it is usually used only for small systems with a few eigenvalues [154].

Linearized augmented plane waves (LAPW)

To solve the energy dependence problem of the basis set, a linearization of the energy of each radial function inside the atomic sphere was suggested by Andersen [156]. The linearization is achieved by taking a linear combination of a solution u at a fixed linearization energy and its energy derivative $\dot{u}$ computed at the same energy. This leads to the following linearized augmented plane wave (LAPW) basis functions [154]:

$$\phi_{\mathbf{G}}(\mathbf{r}) = \begin{cases} \sum_L \left[a_L^{\alpha\mathbf{G}} u_l^\alpha(r') + b_L^{\alpha\mathbf{G}} \dot{u}_l^\alpha(r')\right] Y_L(\theta,\varphi), & r' < R_\alpha, \\ \Omega^{-1/2} \exp(i(\mathbf{k}+\mathbf{G})\mathbf{r}), & r \in I, \end{cases} \tag{2.41}$$

where, as before, the coefficients $a_L^{\alpha\mathbf{G}}$ and $b_L^{\alpha\mathbf{G}}$ are determined from the matching conditions at the atomic sphere boundary. The LAPW method provides a flexible basis for an accurate description of eigenfunctions with eigenenergies near the linearization energy that can be held constant. Unlike in the APW approach, the computation of all eigenenergies can be accomplished with a single diagonalization procedure [154]. To this day, LAPW remains one of the most accurate and reliable schemes for solving the KS equations and is used widely [157, 158].

(Linear) Muffin-tin orbitals ((L)MTO)

Muffin-tin orbitals (MTO) are constructed similarly to APW. Inside the MT-sphere, MTO are expressed as partial waves, analogously to Eq. (2.40). In the interstitial region, instead of PW, screened spherical waves, solutions of the Helmholtz wave equation, are used [159]:

$$\{\nabla^2 - \kappa^2\}\phi_L(\kappa^2, \mathbf{r}) = 0, \tag{2.42}$$

where $\kappa^2 \equiv \epsilon - v_0$, with v_0 being a constant potential in the interstitial region. This basis set composed of partial and screened spherical waves, connected by matching conditions, suffers from the same energy-dependency problem as the original APW methods. Andersen's linearization procedure [156] can also be applied here to construct an energy-independent version of the MTO basis set, i.e., linearized muffin-tin orbitals (LMTO). LMTO methods in combination with the spherical approximation for the potential are, in general, computationally less expensive than full-potential LAPW schemes, but also less accurate. Full-potential and LMTO methods can be coupled (FP-LMTO), and a number of FP-LMTO techniques have been developed [160, 161]. They, however, lack the efficiency of the LMTO methods with the spherically symmetric potential. The non-MT (non-spherical) contributions to the electron density can, in principle, be recovered even from the spherically symmetric potential by the so-called full charge density (FCD) technique [162, 163]. Results obtained with this technique compare well to those of full-potential methods [110].

Full potentials (FP) and muffin-tin (MT) potentials

In full potential methods, the KS equations are solved for all electrons, including the core states. This approach results in very high accuracy but consequently, all-electron methods are the most computationally demanding [110]. The "muffin-tin" term is used to describe both the approximation to the effective potential and the basis set for the KS equations. Similarly to the space division described above, the MT-potential approximation originates from the observation that the one-electron potential is atomic-like close to the atomic sites and almost flat in between [159]. One important distinction from the FP methods is that within

the MT spheres, the potential is assumed to be spherically symmetric. More specifically, the one-electron potential can be expanded in the form [154]:

$$V(\mathbf{r}) = \begin{cases} \sum_{l,m} V_{l,m}(r') Y_{l,m}(\theta, \varphi), & \text{inside the sphere,} \\ \sum_{\mathbf{G}} V(\mathbf{G}) \exp(i\mathbf{G}\mathbf{r}), & \text{outside the sphere,} \end{cases} \tag{2.43}$$

where $V_{l,m}(r')$ is the radial part of $V(\mathbf{r})$. Then, the MT approximation for the full potential corresponds to keeping only spherical components $l = m = 0$ [157]. The MT potential can be used with various basis sets. The FP methods can provide an exact local density or gradient-level description of solid materials [156]. The aforementioned techniques have been utilized to determine the physical characteristics of ordered compounds and to investigate defects in these structures. While these methods are capable of producing highly accurate results, they are typically complex and have certain limitations owing to several numerical approximations [110].

Pseudopotentials (PP)

Pseudopotentials were originally introduced to simplify electronic structure calculations by eliminating the need to include atomic core states and the strong potentials responsible for binding them [164]. Thus, the full-potential description is kept only in the bonding (interstitial) region. Close to the nuclei, the true Coulomb-like potential is replaced by a weak pseudopotential. The pseudopotential corresponding to each atomic species is such that in a reference atomic system (usually the isolated neutral atom), the valence pseudo wavefunctions coincide outside the atomic core with the all-electron valence wavefunctions [165]. Combined with a plane-wave basis set, the PP method offered the advantage of formal simplicity. Unfortunately, this simplicity comes at a cost: first-row ele-

ments, systems with d- or f-electrons are computationally demanding to treat with standard PPs since a huge number of PWs is needed to correctly reproduce the rapidly oscillating wave function close to the nuclei [166–168]. A significant improvement in the performance of PPs came with the development of the ultrasoft PPs [169]. "Soft" PPs, as opposed to "hard" ones, require fewer Fourier components, and, thus, are more efficient. The pseudopotential technique offers a significant advantage over all electron DFT implementations in terms of transferability. By constructing PPs from a fixed electronic configuration of an isolated atom or ion, these models can accurately reproduce the scattering properties of a nucleus in that specific configuration, and be transferable to different atomic configurations and solid-state environments [170]. Another great advantage of the PP method is its ability to easily incorporate molecular dynamics [171].

Projector augmented-wave (PAW) method

The projector augmented-wave method was first derived by Blöchl [152]. The PAW method can be considered a bridge between linear methods, namely LAPW, and the pseudopotential approach. Indeed, the LAPW is a special case of the PAW method, and the PP formalism can be obtained by a well-defined approximation [152]. The PAW method can be regarded as an all-electron method, and its fundamentals are given below.

As before, the rapidly oscillating wave function in the core region is the primary issue to be addressed. The usual PP formalism requires a large number of plane waves to be included in the basis set. The main idea of PAW is to introduce a set of fictitious pseudo (PS) wave functions $|\tilde{\Psi}\rangle$, which do not carry any physical meaning themselves, but are computationally convenient. If one can, then, establish a clear mapping between the two, various observables can be calculated using

these computationally convenient PS wave functions and then transformed back to the physically relevant all-electron (AE) wave function $|\Psi\rangle$. More specifically, one seeks to construct a transformation as follows [152]:

$$|\Psi\rangle = T|\tilde{\Psi}\rangle, \tag{2.44}$$

which should satisfy the following criterion: in the interstitial region the wave function can be described well by plane waves and needs to be augmented only in the core region. Such transformation can be shown to have the following form [152, 172]:

$$\begin{aligned} T &= 1 + \sum_i \big(|\phi_i\rangle - |\tilde{\phi}_i\rangle \big) \langle \tilde{p}_i|, \\ |\Psi_{n,\mathbf{k}}\rangle &= |\tilde{\Psi}_{n,\mathbf{k}}\rangle + \sum_i \big(|\phi_i\rangle - |\tilde{\phi}_i\rangle \big) \langle \tilde{p}_i|\tilde{\Psi}_{n,\mathbf{k}}\rangle, \end{aligned} \tag{2.45}$$

where index i is a shorthand for the atomic site R, and quantum numbers l and m. The PS orbitals $|\tilde{\Psi}_{n,\mathbf{k}}\rangle$ are identical to the AE $|\Psi_{n,\mathbf{k}}\rangle$ outside the PAW spheres (interstitial region), where they are expanded in PW as:

$$\langle \mathbf{r}|\tilde{\Psi}_{n,\mathbf{k}}\rangle = \frac{1}{\Omega^{1/2}} \sum_{\mathbf{G}} C_{n,\mathbf{k},\mathbf{G}} \exp(i(\mathbf{G}+\mathbf{k})\mathbf{r}), \tag{2.46}$$

where Ω is the volume of the Wigner-Seitz cell, and $C_{n,\mathbf{k},\mathbf{G}}$ is the normalization constant. The transformation inside the PAW sphere is determined by three quantities, namely the AE partial waves $|\phi_i\rangle$, PS partial waves $|\tilde{\phi}_i\rangle$ and projector functions $|\tilde{p}_i\rangle$. In principle, there is an infinite number of ways to construct them [152]. In this work, the AE partial waves are the solutions of the radial Schrödinger equation for a non-spinpolarized reference atom at a specific energy

ε_i and for a specific angular momentum l_i [172],

$$\langle \mathbf{r} \, | \phi_i \rangle = \frac{1}{\mathbf{r} - \mathbf{R}_i} u_{l_i,\varepsilon_i}(|\mathbf{r} - \mathbf{R}_i|) Y_{l_i,m_i}(\mathbf{r} - \mathbf{R}_i). \tag{2.47}$$

The PS partial waves are defined similarly, under the condition that they must coincide with the AE partial waves outside the PAW sphere of radius, r_c,

$$\langle \mathbf{r} | \tilde{\phi}_i \rangle = \tilde{\phi}_i(|\mathbf{r} - \mathbf{R}_i|) Y_{l_i,m_i}(\mathbf{r} - \mathbf{R}_i), \tag{2.48}$$

where [173]:

$$\tilde{\phi}_i(|\mathbf{r} - \mathbf{R}_i|) \equiv \tilde{\phi}_i(r) = \begin{cases} \sum_{a=1}^{2} \alpha_a j_i(q_a r), & r < r_c^i, \\ u_{l_i,\varepsilon_i}(r), & r > r_c^i, \end{cases} \tag{2.49}$$

where j_i are spherical Bessel functions, and α_a and q_a are chosen such that the PS partial wave is two times continuously differentiable. The projector functions are dual to the PS partial waves,

$$\langle \tilde{p}_i | \tilde{\phi}_j \rangle = \delta_{i,j}. \tag{2.50}$$

They are constructed using a two-step procedure [99, 172]. First, trial functions $|\chi_i\rangle$ are calculated via

$$|\chi_i\rangle = \left(\varepsilon_i + \frac{\nabla^2}{2} - \tilde{v}_{eff}\right) |\tilde{\phi}_i\rangle, \tag{2.51}$$

where ε_i is the reference energy, $\tilde{v}_{eff}$ is the spherical component of the effective PS potential, which can be chosen arbitrarily inside the augmentation region of radius r_c, but must match the exact effective potential v_{eff} outside. Next, the

projector functions are taken to be linear combinations of $|\chi_i\rangle$ under the constraint of Eq. (2.50),

$$|\tilde{p}_i\rangle = \sum_j \langle\tilde{\phi}_i\,|\chi_j\rangle\,|\chi_j\rangle\,. \tag{2.52}$$

Using Eq. (2.45), various observables can be calculated as expectation values of the corresponding operators $\langle\Psi_n|A\,|\Psi_n\rangle$, or using the PS wave functions $\langle\tilde{\Psi}_n|A^\dagger|\tilde{\Psi}_n\rangle$, with $A^\dagger = T^\dagger A T$. For example, the one-electron density that enters the HK variational principle is given as the expectation value of the real-space projection operator $|\mathbf{r}\rangle\langle\mathbf{r}|$ [152], i.e.,

$$\rho(\mathbf{r}) = \tilde{\rho}(\mathbf{r}) + \rho^1(\mathbf{r}) + \tilde{\rho}^1(\mathbf{r}), \tag{2.53}$$

with

$$\begin{aligned}
\tilde{\rho}(\mathbf{r}) &= \sum_n f_n \langle\tilde{\Psi}_n|\mathbf{r}\rangle\langle\mathbf{r}|\tilde{\Psi}_n\rangle, \\
\rho^1(\mathbf{r}) &= \sum_{n,i,j} f_n \langle\tilde{\Psi}_n|\tilde{p}_i\rangle\langle\phi_i|\mathbf{r}\rangle\langle\mathbf{r}|\phi_j\rangle\langle\tilde{p}_j|\tilde{\Psi}_n\rangle, \quad \text{and} \\
\tilde{\rho}^1(\mathbf{r}) &= \sum_{n,i,j} f_n \langle\tilde{\Psi}_n|\tilde{p}_i\rangle\langle\tilde{\phi}_i|\mathbf{r}\rangle\langle\mathbf{r}|\tilde{\phi}_j\rangle\langle\tilde{p}_j|\tilde{\Psi}_n\rangle,
\end{aligned} \tag{2.54}$$

where f_n is the occupation of the n-th KS state.

DFT+U can also be implemented within the PAW formalism [174, 175]. The Hubbard U correction to the total energy is given by Eq. (2.39). This energy functional depends on the occupation of the set of localized orbitals. The occupations are defined as the elements of the on-site density matrix by projecting the KS states onto a set of atomic-like orbitals in the region close to the nuclei, Eq. (2.34). Within the PAW formalism, a convenient set of orbitals are the AE partial waves, given by Eq. (2.47). Thus, the on-site density matrix is obtained

by projecting the KS wave function onto the augmentation region [174]:

$$n^{\sigma,\alpha}_{m,m'} = \sum_{\nu,\mathbf{k}} \sum_{l,l',n,n'} f^{\sigma}_{\nu,\mathbf{k}} \langle \Psi^{\sigma}_{\nu,\mathbf{k}} | \phi_{l,m,n} \rangle \langle \phi_{l',m',n'} | \Psi^{\sigma}_{\nu,\mathbf{k}} \rangle. \tag{2.55}$$

In (2.55) the indices i and j are written explicitly as l, m, n and l', m', n', respectively, with n being the reference energy used in (2.47) to construct the partial waves. The index α denotes the atomic site R_α, for which the on-site density matrix is calculated. Computationally, it is more convenient to obtain the occupancies directly from the PS wave function via [175]

$$n^{\sigma,\alpha}_{m,m'} = \sum_{n,n'} \rho^{PAW}_{(lmn),(l'm'n')} \left\langle \phi_{l,m,n} | \phi_{l',m',n'} \right\rangle, \tag{2.56}$$

where the occupancies of the augmentation channels are defined as

$$\rho^{PAW}_{(lmn),(l'm'n')} = \sum_{n} f_n \langle \tilde{\Psi}_\nu | \tilde{p}_{l,m,n} \rangle \langle \tilde{p}_{l'm'n'} | \tilde{\Psi}_\nu \rangle. \tag{2.57}$$

The occupancies in Eq. (2.56) can be obtained either self-consistently, recalculating the occupational matrix at each iteration, or they can be constrained to a desired configuration [176].

2.1.6 Disorder, special quasirandom structures (SQS)

Many real systems do not possess a perfectly ordered crystalline structure. Examples include alloys, mixed crystals, doped semiconductors, liquid crystals, etc [177]. Unlike the perfect single crystals, these systems do not have periodic structures, which poses a serious challenge in modeling them. The problem of the disorder

can be modeled by a TB-Hamiltonian [177]:

$$H = \sum_i \varepsilon_i c_i^\dagger c_i + \sum_{i \neq j} t_{ij} c_i^\dagger c_j, \tag{2.58}$$

where the on-site and hopping terms are separated, and only one state (orbital) per site is considered, i.e., a single-band model. Eq. (2.58) describes disorder when the on-site energies ε_i, or the hopping integrals t_{ij}, or both are not fixed values, but instead acquire values according to some probability distribution. For example, in the simplest case of a binary alloy $A_{1-x}B_x$, the probability of the on-site energy would take on the values [177]

$$P(\varepsilon_i) = (1-x)\delta(\varepsilon_i - \varepsilon_A) + x\delta(\varepsilon_i - \varepsilon_B), \tag{2.59}$$

where ε_A and ε_B are the on-site energies if the site i is occupied by the element A or B, respectively. This is a case of diagonal disorder, i.e., only on-site energies are subjected to disorder, and the hopping integrals have fixed values. The case of off-diagonal disorder as well as the combination of the two are also possible [177]. As in the case with the on-site interaction in Eq. (2.27), due to the presence of disorder the Hamiltonian given by Eq. (2.58) cannot be diagonalized, since the translation symmetry is broken, which makes the Bloch theorem inapplicable. The equilibrium properties of such systems are usually discussed in terms of the ensemble-averaged Green's function G, which determines all the macroscopic properties of interest [177]:

$$G(z) \equiv \langle G(z) \rangle = \langle (z - H)^{-1} \rangle, \tag{2.60}$$

where z is the complex energy, and H is given by Eq. (2.58). The averaged Green's function is usually found using perturbation theory; $G(z)$ is determined as an expansion in powers of a perturbation parameter V and averaging each term of the expanded series. In many cases, it is quite difficult to calculate $G(z)$ exactly, and further approximations are necessary to truncate the expansion [177].

An alternative approach is to consider a single realization of disorder, which exhibits certain macroscopic properties of interest. In other words, instead of considering an ensemble average of a set of configurations, the aim is to design a single configuration, which will exhibit the macroscopic properties of the ensemble average. Such an object is known as a special quasirandom structure (SQS) [92, 178]. To illustrate the method, consider a binary $A_{1-x}B_x$ alloy (although it can be formulated for more components [179]). The alloy is characterized by the multisite correlation function borrowed from statistical lattice theory [180]. Any given arrangement of A and B atoms on a lattice (configuration σ) is discretized into its "figures" $f = (k, m)$, where k is the number of vertices in the figure (pairs, triplets, etc.), and m is the interaction distance (nearest neighbor, next-nearest neighbor, etc.). Fig. 2.2 shows different figures in a lattice of "up" and "down" spins S_i. This "spin" variable S_i, assigned to each lattice site i, can take the value -1 if this site is occupied by atom A and +1 if by atom B. The product of spin variables for figure f at location l is defined as [92]

$$\Pi_f(l, \sigma) = \prod_i S_i. \tag{2.61}$$

A lattice average of the spin product over all locations of symmetry-related figures of type f is [92]

$$\overline{\Pi}_f(\sigma) = \frac{1}{ND_f} \sum_l \Pi_f(l, \sigma), \tag{2.62}$$

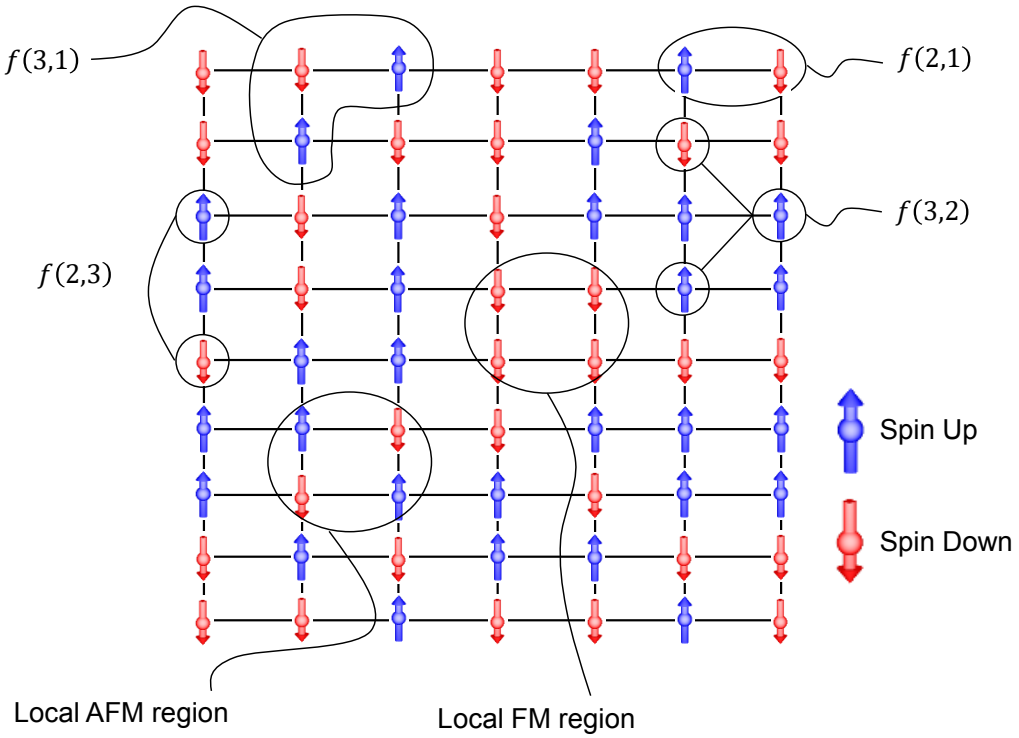

Figure 2.2: Special quasirandom structure construction. Examples of figures f of different order (k, m).

where N is the number of atoms, and D_f is the number of figures per site. The ensemble average of a physical property P over configurations is given as [180]:

$$\langle P \rangle = \sum_{k,m} D_{k,m} \langle \overline{\Pi}_{k,m} \rangle p_{k,m}, \tag{2.63}$$

where $p_{k,m}$ are the "interaction parameters" of figures (k, m). For a perfectly random configuration, the ensemble averages of the products $\overline{\Pi_f}$ are known analytically [181]:

$$\langle \overline{\Pi}_{k,m} \rangle_R = (2x - 1)^k. \tag{2.64}$$

The core idea of the SQS approach is to design a special N-atom periodic structure S whose correlation functions $\langle \overline{\Pi}_{k,m} \rangle$ best match the analytically known correla-

tion functions of a perfectly random alloy $\langle \overline{\Pi}_{k,m} \rangle_R$. Thus, the natural way to select a special structure S is to minimize the following difference [92]:

$$\langle P \rangle_R - P(S) = \sum_{k,m}{}' D_{k,m} \big[(2x-1)^k - \overline{\Pi}_{k,m} \big] p_{k,m}, \tag{2.65}$$

where the prime sign in the summation means that the terms with $k = 0$ and $k = 1$ are omitted.

The SQS method is easily incorporated with the known DFT methods and has been used extensively in the study of random and disordered alloys [181–183]. It has also been used to model PM systems [184–187]. A PM system is modeled as an array of randomly placed "up" and "down" magnetic moments. This description has been shown to produce energy gaps in TM compounds, overcoming the metallic behavior exhibited when they are modeled as non-magnetic systems [187, 188].

2.2 Optical properties

Optical spectra of materials provide a rich source of information on their electronic and atomic properties. Fig. (2.3) shows some of the processes that occur when a system is subjected to incoming light. A fraction of the incident light is reflected at the surface of the medium, while the remaining light is transmitted. Within the medium, some of the radiation may undergo absorption or scattering, while the rest continues its path through the sample. Absorbed electromagnetic waves can either be dissipated as heat or reemitted at a different frequency. Typically, reflection and absorption are the most dominant optical phenomena since they involve the simplest level of interaction between electromagnetic waves and elementary excitations within the medium [93].

In a dielectric medium an external electromagnetic wave $\mathbf{E}(\mathbf{r}, t)$ will induce a

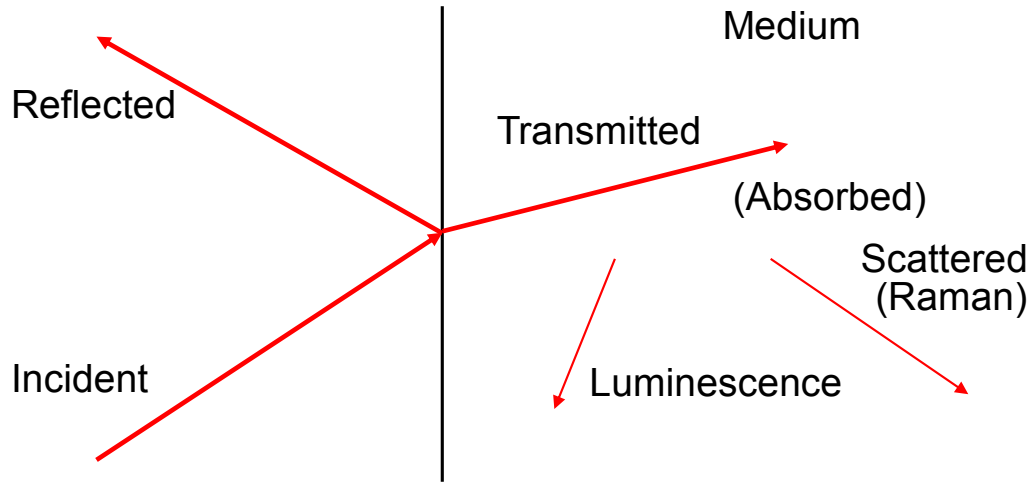

Figure 2.3: Optical processes that take place at the surface and in the interior of a medium [93].

polarization $\mathbf{P}(\mathbf{r}, t)$ [93]

$$P_\alpha(\mathbf{r}', t') = \sum_\beta \varepsilon_0 \int \chi_{\alpha\beta}(\mathbf{r}, \mathbf{r}'; t, t') E_\beta(\mathbf{r}, t) d\mathbf{r} dt, \tag{2.66}$$

where $\chi_{\alpha\beta}(\mathbf{r}, \mathbf{r}'; t, t')$ is the complex electric susceptibility tensor and ε_0 is the vacuum permittivity. In the absence of time-dependent perturbations, time is homogeneous, and the susceptibility depends only on the difference $t - t'$. In the case of a periodic medium, such as crystals, the system is translation-invariant up to the lattice vector. Thus, the polarization can be Fourier transformed in both time and coordinate domains to give [93]:

$$P_i(\mathbf{q}, \omega) = \sum_j \varepsilon_0 \chi_{ij}(\mathbf{q}, \omega) E_j(\mathbf{q}, \omega), \tag{2.67}$$

where $\mathbf{q}$ is the crystal wave vector belonging to the first BZ and ω is the light frequency. In principle, all optical properties of a system are determined by its susceptibility χ_{ij}. It is often more convenient to work with the dielectric function defined as [93]:

$$\epsilon_{ij}(\mathbf{q},\omega) = 1 + \chi_{ij}(\mathbf{q},\omega). \tag{2.68}$$

In many cases, the wavelength of light is much larger than the relevant dimensions of the crystal. In such cases the spatial dispersion, i.e., the $\mathbf{q}$-dependence in Eq. (2.68) can be suppressed. Knowing the dielectric function, Eq (2.68), allows us to determine other optical functions that can be measured experimentally, such as reflectivity [93]:

$$r(\omega) = \left| \frac{\sqrt{\epsilon(\omega)} - 1}{\sqrt{\epsilon(\omega)} + 1} \right|^2 \tag{2.69}$$

Other useful optical functions such as transmittance T and reflectance R can also be obtained from the reflectivity as:

$$R(\omega) = r(\omega)[1 + \tau(\omega)T(\omega)]; \qquad T(\omega) = \frac{\tau(\omega)[1 - r(\omega)]^2}{1 - r^2(\omega)\tau^2(\omega)}, \tag{2.70}$$

where the power-loss factor τ is defined as:

$$\tau(\omega) = \exp\big(-2d\mathrm{Im}(\sqrt{\epsilon})\omega/c\big), \tag{2.71}$$

with d and c being the thickness of a slab and the speed of light, respectively.

2.2.1 Atomic contribution

In the infrared region, a crystal's optical properties are mostly determined by its atomic response to incident electromagnetic waves. The simplest form for the

dielectric function is given by the Lorentz model:

$$\epsilon(\omega) = \epsilon_\infty + \sum_j \frac{S_j}{\omega_{0,j}^2 - \omega^2 + i\gamma}, \tag{2.72}$$

where ϵ_∞ is the high-frequency dielectric constant, S_j and $\omega_{0,j}$ are the strength and frequency of the j-th oscillator, respectively. The damping constant γ is introduced in order to achieve a better agreement with the experiment as depicted in Fig. 2.4. Usually, all parameters in Eq. (2.72) are determined by fitting the mea-

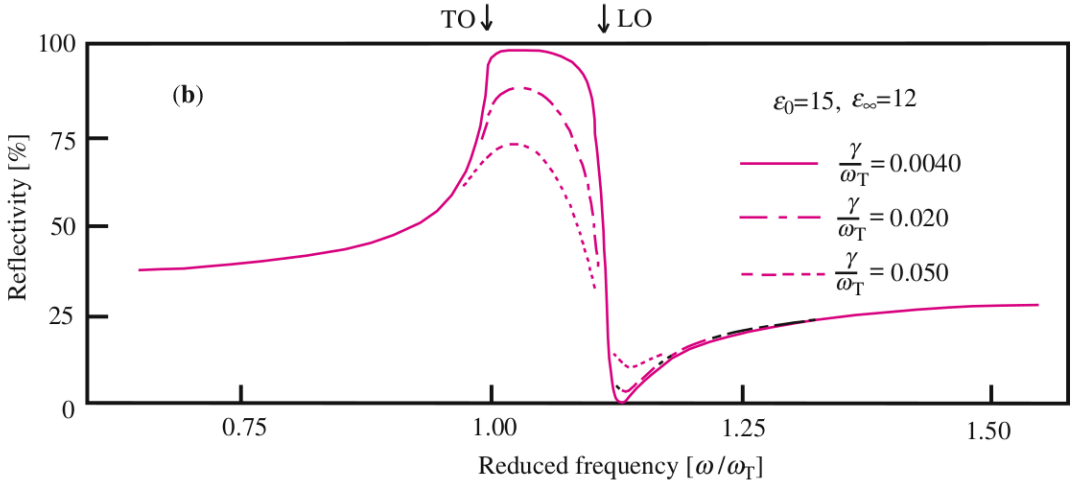

Figure 2.4: Schematic reflectivity [93]. The damping coefficient γ lowers the reflectivity in the reststrahlen band between the TO and LO frequencies, which otherwise would be a plateau of maximum reflectivity of width proportional to the oscillator strength S_j.

sured reflectivity to Eq. (2.69) with the dielectric function defined by Eq. (2.72). The dielectric function in Eq. (2.72) can also be determined *ab initio* using DFT. Essentially, it involves the calculation of the resonant frequencies $\omega_{0,j}$, which are inferred from the atomic vibrations in the crystal. Whenever an atom is displaced from its equilibrium position, there is an increase of potential energy, which induces a restoration force that tries to bring the atom back to its equilibrium

position. For small displacements u, the potential energy can be written as [94]:

$$\begin{aligned} V = &\sum_{l,l',\kappa,\kappa'} \sum_{\alpha,\beta} \Phi_{\alpha\beta}(l\kappa, l'\kappa') u_\alpha(l\kappa) u_\beta(l'\kappa') + \\ &+ \sum_{l,l',\kappa,\kappa'} \sum_{\alpha,\beta} \Phi_{\alpha\beta\gamma}(l\kappa, l'\kappa', l''\kappa'') u_\alpha(l\kappa) u_\beta(l'\kappa') u_\gamma(l''\kappa'') + \ldots, \end{aligned} \tag{2.73}$$

where $\Phi_{\alpha\beta}$ and $\Phi_{\alpha\beta\gamma}$ are the second- and third-order interactomic force constants (IFC), κ and κ' are the atoms in the primitive cells (PC) l and l', and α, β and γ are the Cartesian indices. Keeping only the first term in Eq. (2.73) corresponds to the harmonic approximation. To obtain the atomic vibrational frequencies, a system of equations of motion for each atom in the unit cell needs to be solved, with the periodic conditions determined by the translational symmetry of the underlying primitive cell [153]. Finding the solution of the equations of motion implies the determination of the IFCs and performing an FT to build the dynamical matrix, which is then diagonalized to yield the vibrational frequencies. The dynamical matrix is defined as [94]:

$$D_{\alpha\beta}(\kappa\kappa', \mathbf{q}) = \frac{1}{\sqrt{m_\kappa m_{\kappa'}}} \sum_{l'} \Phi_{\alpha\beta}(l_1\kappa, l'\kappa') \exp(i\mathbf{q}[\mathbf{r}(l'\kappa') - \mathbf{r}(l_1\kappa)]), \tag{2.74}$$

where $\mathbf{r}(l'\kappa')$ denotes the position of the κ'-th atom in the l'-th primitive cell. In Eq. (2.74) one primitive cell l_1 is chosen among all PC comprising the unit cell, with respect to which the dynamical matrix is defined. This cell is omitted from the summation. The dynamical matrix in Eq. (2.74) is diagonalized to yield the vibrational eigenfrequencies:

$$\omega^2_{\mathbf{q}j} \delta_{jj'} = \sum_{\alpha,\beta,\kappa,\kappa'} e^*_\alpha(\kappa', \mathbf{q}j) D_{\alpha\beta}(\kappa\kappa', \mathbf{q}) e_\beta(\kappa', \mathbf{q}j'), \tag{2.75}$$

where $e_\alpha(\kappa, \mathbf{q}j)$ and $\omega^2_{\mathbf{q}j}$ are the eigenvector and eigenfrequency, respectively, which correspond to the phonon mode of the j-th branch with wavevector $\mathbf{q}$. As can be seen, the problem of determining the vibrational spectra of a crystal is reduced to the evaluation of the IFCs. There are two main approaches to accomplishing this task. The IFCs can be obtained using density functional perturbation theory (DFPT), and are expressed in terms of the changes in the electron density $\rho(\mathbf{r})$ [189]. Alternatively, the IFCs can be obtained using the finite displacement method (FDM). The second-order IFCs are given by the second-order derivative of the potential energy, Eq. (2.73), with respect to atomic displacements [94], i.e.:

$$\Phi_{\alpha\beta}(l\kappa, l'\kappa') = \frac{\partial^2 V}{\partial r_\alpha(l\kappa)\partial r_\beta(l'\kappa')} = -\frac{\partial F_\beta(l'\kappa')}{\partial r_\alpha(l\kappa)}, \tag{2.76}$$

where $F_\beta(l'\kappa')$ is the β-th component of the force acting on the κ'-th atom in the l'-th primitive cell, when the κ-th atom in the l-th primitive cell is displaced in the direction α. The force gradient in Eq. (2.76) can be approximated by its finite difference expression:

$$\Phi_{\alpha\beta}(l\kappa, l'\kappa') \approx \frac{F_\beta(l'\kappa')}{\delta r_\alpha(l\kappa)}. \tag{2.77}$$

In the FDM approach, to construct the full IFC matrix, Eq. (2.77), each atom $l\kappa$ needs to be displaced. The forces acting on atoms $l'\kappa'$ are then extracted from DFT calculation using the Hellmann-Feynman theorem [190]. To obtain accurate IFCs supercells containing several PCs need to be checked for convergence with respect to the supercell size. Depending on the size of the supercell, the calculation of the IFC might require a large number of displacement configurations to construct the full IFC matrix, Eq. (2.77). This number can be greatly reduced by using the site symmetries, which show that only the IFC between inequivalent atoms in the PC need to be determined and the rest can be reconstructed by

employing site symmetry operations [94, 191].

An accurate description of the optical response requires the knowledge of the damping processes of atomic vibrations. In order to include these processes, it is necessary to go beyond the harmonic approximation in Eq. (2.73). In order to introduce anharmonic contributions, the dielectric function can be written in a more general way using perturbation theory as [96, 192]:

$$\epsilon(\omega) = \epsilon_\infty + \sum_j \frac{S_j \omega_{0,j}^2}{\omega_{0,j}^2 - \omega^2 + 2\omega_{0,j}\Pi_j(\omega)}, \tag{2.78}$$

The oscillator strength is related to the Born effective charges Z, as $S_j = 4\pi Z^2/(v\mu_j\omega_{0,j}^2)$, where v is the unit-cell volume and μ is the reduced mass of the oscillator [193]. Here, unlike the constant damping factor γ in Eq. (2.72), the damping is given by $\Pi_j(\omega)$ which is the complex self-energy of the j-th vibrational mode. This phonon self-energy can be expressed as a sum of different terms, each corresponding to a particular type of interaction that causes damping. The main contributions are due to anharmonic phonon-phonon scattering processes. Generally, the anharmonic Hamiltonian can be expressed as [95]

$$H = H_0 + H_A = H_0 + H^{(3)} + H^{(4)}, \tag{2.79}$$

with H_0 as the harmonic part given by:

$$H_0 = \sum_{\mathbf{q},j} \omega(\mathbf{q}, j) a_{\mathbf{q},j}^\dagger a_{\mathbf{q},j}, \tag{2.80}$$

where $a_{\mathbf{q},j}^\dagger$ and $a_{\mathbf{q},j}$ are the creation and destruction operators for the phonon mode with wave vector $\mathbf{q}$ and branch j, $\omega(\mathbf{q}, j)$ is the frequency of the phonon mode $(\mathbf{q}, j)$. The anharmonic part H_A corresponds to the phonon-phonon scattering

processes. It can be split into different parts, each corresponding to the order of the processes included. For example, three- and four-phonon processes are defined as [95, 194]:

$$H^{(3)} = \sum_{\mathbf{q}_1,\mathbf{q}_2,\mathbf{q}_3} \sum_{j_1,j_2,j_3} V^{(3)}(\mathbf{q}_1 j_1; \mathbf{q}_2 j_2; \mathbf{q}_3 j_3)(a^{\dagger}_{-\mathbf{q}_1,j_1} + a_{\mathbf{q}_1,j_1})(a^{\dagger}_{-\mathbf{q}_2,j_2} + a_{\mathbf{q}_2,j_2}) \times \\ \times (a^{\dagger}_{-\mathbf{q}_3,j_3} + a_{\mathbf{q}_3,j_3}), \tag{2.81}$$

and

$$H^{(4)} = \sum_{\mathbf{q}_1,\mathbf{q}_2,\mathbf{q}_3,\mathbf{q}_4} \sum_{j_1,j_2,j_3,j_4} V^{(4)}(\mathbf{q}_1 j_1; \mathbf{q}_2 j_2; \mathbf{q}_3 j_3; \mathbf{q}_4 j_4)(a^{\dagger}_{-\mathbf{q}_1,j_1} + a_{\mathbf{q}_1,j_1}) \times \\ \times (a^{\dagger}_{-\mathbf{q}_2,j_2} + a_{\mathbf{q}_2,j_2})(a^{\dagger}_{-\mathbf{q}_3,j_3} + a_{\mathbf{q}_3,j_3})(a^{\dagger}_{-\mathbf{q}_4,j_4} + a_{\mathbf{q}_4,j_4}), \tag{2.82}$$

where $V^{(n)}(\mathbf{q}_1 j_1; \ldots; \mathbf{q}_n j_n)$ is the n-th order interaction term involving n phonon modes $(\mathbf{q}_1 j_1), \ldots, (\mathbf{q}_n j_n)$. The interaction term $V^{(n)}$ is defined as the Fourier transform of the interatomic force constants [194]:

$$V^{(n)}(\mathbf{q}_1 j_1; \ldots; \mathbf{q}_n j_n) = \frac{1}{\sqrt{N}} \frac{1}{n!} \sum_{\kappa_1,\ldots,\kappa_n} \sum_{\alpha_1,\ldots,\alpha_n} e_{\alpha_1}(\kappa_1, \mathbf{q}_1, j_1) \times \ldots \times e_{\alpha_n}(\kappa_n, \mathbf{q}_n, j_n) \\ \sqrt{\frac{\hbar}{2m_{\kappa_1}\omega_{\mathbf{q}_1,j_1}}} \times \ldots \times \sqrt{\frac{\hbar}{2m_{\kappa_n}\omega_{\mathbf{q}_n,j_n}}} \sum_{l_2,\ldots,l_n} \Phi_{\alpha_1,\ldots,\alpha_n}(l_1\kappa_1; \ldots; l_n\kappa_n) \times \\ \times \exp\Big(i\mathbf{q}_1[\mathbf{r}(l_2\kappa_2) - \mathbf{r}(l_1\kappa_1)]\Big) \times \ldots \times \exp\Big(i\mathbf{q}_n[\mathbf{r}(l_n\kappa_n) - \mathbf{r}(l_1\kappa_1)]\Big)\delta(\mathbf{q}_1 + \cdots + \mathbf{q}_n). \tag{2.83}$$

Here, κ runs over all atoms in the primitive cell, summation l over all primitive cells in the supercell except the central one l_1, and $\alpha_1 \ldots \alpha_n$ are the Cartesian indices. Vector $\mathbf{e}(\kappa_n, \mathbf{q}_n, j_n)$ is the eigenvector of the phonon mode $(\mathbf{q}_n, j_n)$. $\Phi_{\alpha_1,\ldots,\alpha_n}(l_1\kappa_1; \ldots; l_n\kappa_n)$ are the interatomic force constants. The phonon self-

energy for these processes can be obtained using perturbation theory. It involves the calculation of Feynman diagrams such as the ones shown in Fig. 2.5(a)−(c). These diagrams correspond to the lowest order of the perturbation expansion in powers of H_A [95, 96]. In this work, only the bubble diagram is taken into account. The complex self-energy can be decomposed as:

$$\Pi_{\mathbf{q},j}(\omega) = \Delta_{\mathbf{q},j}(\omega) + i\Gamma_{\mathbf{q},j}(\omega), \tag{2.84}$$

where Δ and Γ are the real and imaginary parts of the phonon self-energy, respectively. The imaginary part of the bubble diagram is given by [194]:

$$\begin{aligned}\Gamma_{\mathbf{q},j}(\omega) = 18\pi \sum_{\mathbf{q}_1 j_1, \mathbf{q}_2 j_2} \left|V(-\mathbf{q}j, \mathbf{q}_1 j_1, \mathbf{q}_2 j_2)\right|^2 \Big\{ &(n_{\mathbf{q}_1 j_1} + n_{\mathbf{q}_2 j_2} + 1) \times \\ &\times \delta(\omega - \omega_{\mathbf{q}_1 j_1} - \omega_{\mathbf{q}_2 j_2}) + (n_{\mathbf{q}_1 j_1} - n_{\mathbf{q}_2 j_2}) \big[\delta(\omega + \omega_{\mathbf{q}_1 j_1} - \omega_{\mathbf{q}_2 j_2}) - \\ &- \delta(\omega - \omega_{\mathbf{q}_1 j_1} + \omega_{\mathbf{q}_2 j_2})\big] \Big\},\end{aligned} \tag{2.85}$$

where $n_{\mathbf{q}j}$ is the Bose-Einstein function defined as:

$$n_{\mathbf{q}j} = \frac{1}{\exp(\omega_{\mathbf{q}j}/k_B T) - 1}, \tag{2.86}$$

with k_B and T being the Boltzmann constant and the temperature. The real part of the self-energy can be obtained using the Kramers-Kronigs relation [194]:

$$\Delta(\omega) = \frac{1}{\pi} \int_{-\infty}^{+\infty} \frac{\Gamma(\omega')}{\omega' - \omega} d\omega'. \tag{2.87}$$

In addition to phonon-phonon processes, the isotope-disorder scattering is also considered, Fig. 2.5(c). This contribution can be estimated by using perturbation theory too, where the atomic mass deviation is treated as perturbation [97]. The

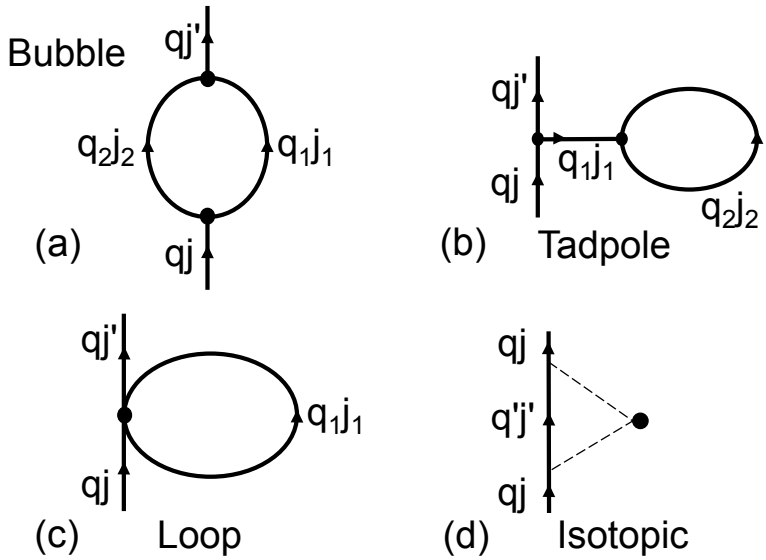

Figure 2.5: Diagrammatic anharmonic contributions considered in this work. Diagrams (a) and (b) represent three-phonon scattering processes known as "bubble" and "tadpole" contributions [95]. Diagram (c) shows a four-phonon scattering process known as "loop" [95]. In our study, the only process entering in our model, as explained in the main text, is the bubble contribution. Diagram (d) represents isotope-disorder scattering, the dashed lines represent phonon scatterings by the isotope shown here as the black dot [97].

self-energy of this contribution is given by [97, 194]:

$$\Gamma^{iso}(\omega) = \frac{\pi}{2N}\omega_{\mathbf{q}j}^2 \sum_{\mathbf{q}_1 j_1} \delta(\omega - \omega_{\mathbf{q}_1 j_1}) \sum_{\kappa} g_\kappa \left| \sum_{\alpha} e_\alpha(\kappa_1, \mathbf{q}, j) e_\alpha^*(\kappa_1, \mathbf{q}_1, j_1) \right|^2, \quad (2.88)$$

where the mass parameter g_κ is defined as:

$$g_\kappa = \sum_i f_i (1 - m_{i\kappa}/\tilde{m}_\kappa)^2, \quad (2.89)$$

with f_i and $m_{i\kappa}$ being the mole fraction and relative atomic mass of the i-th isotope, respectively. $\tilde{m}_\kappa$ is the average mass given by: $\tilde{m}_\kappa = \sum_i f_i m_{i\kappa}$.

High-frequency dielectric constant

The electronic contribution to the dielectric function of a system is usually calculated using linear response theory [137]. The effect of the applied electric field $\mathbf{E}(\mathbf{r}, t)$ is treated as a perturbation. The response of the system is constructed using perturbation theory with reference to a system for which the dielectric response is known exactly, for instance, a system of non-interacting particles. The electron polarizability of non-interacting electrons is known analytically [195–197]:

$$\chi_0(\mathbf{q}+\mathbf{G}, \mathbf{q}+\mathbf{G}') = -\frac{4}{(2\pi)^3} \sum_{v,c} \int_{BZ} d\mathbf{k} \frac{\langle \mathbf{k}+\mathbf{q}, c | e^{i(\mathbf{q}+\mathbf{G})\cdot\mathbf{r}} | \mathbf{k}, v \rangle \langle \mathbf{k}, v | e^{-i(\mathbf{q}+\mathbf{G}')\cdot\mathbf{r}} | \mathbf{k}+\mathbf{q}, c \rangle}{E_c(\mathbf{k}+\mathbf{q}) - E_v(\mathbf{k})}, \tag{2.90}$$

where the summation is taken over all Bloch states in the valence (v) and conduction (c) bands, with energies E_v and E_c, respectively. The integration runs over the entire BZ. The simplest approximation for the dielectric function is given within the random phase approximation (RPA) as [197, 198]:

$$\epsilon_{RPA}(\mathbf{q}+\mathbf{G}, \mathbf{q}+\mathbf{G}') = \delta_{\mathbf{G},\mathbf{G}'} - 4\pi \frac{\chi_0(\mathbf{q}+\mathbf{G}, \mathbf{q}+\mathbf{G}')}{|\mathbf{q}+\mathbf{G}|^2}, \tag{2.91}$$

where the term $\frac{1}{|\mathbf{q}+\mathbf{G}|^2}$ is the reciprocal space representation of the Coulomb interaction. In the context of DFT, Eq. (2.91) is equivalent to neglecting all exchange effects, and it can be shown to be [197, 199]:

$$\epsilon_{DFT}(\mathbf{q}+\mathbf{G}, \mathbf{q}+\mathbf{G}') = 1 - V_c \tilde{\chi} (1 - V_x \tilde{\chi})^{-1}, \tag{2.92}$$

where

$$\begin{aligned} V_c(\mathbf{q}+\mathbf{G}, \mathbf{q}+\mathbf{G}') &= \delta_{\mathbf{G},\mathbf{G}'} \frac{1}{\Omega} \int d\mathbf{r} \frac{e^{-i(\mathbf{q}+\mathbf{G}')\cdot\mathbf{r}}}{|\mathbf{r}-\mathbf{r}'|}, \\ V_x(\mathbf{q}+\mathbf{G}, \mathbf{q}+\mathbf{G}') &= \frac{1}{\Omega} \int e^{-i(\mathbf{q}+\mathbf{G}')\cdot\mathbf{r}} \frac{\delta V_{xc}[\rho]}{\delta \rho} e^{-i(\mathbf{q}+\mathbf{G}')\cdot\mathbf{r}}. \end{aligned} \tag{2.93}$$

The symbol $\tilde{\chi}$ in Eq. (2.92) is used to indicate that the Bloch states are obtained using the KS self-consistent method. The RPA limit is obtained from Eq. (2.93) where the exchange term V_x is put equal to zero. Finally, the high-frequency dielectric constant ϵ_∞ is obtained as a long-wavelength limit of the $\mathbf{G} = \mathbf{G}' = 0$ element of the inverse of the dielectric matrix in Eq. 2.92:

$$\epsilon_\infty = \lim_{\mathbf{q}\to 0} \frac{1}{\epsilon^{-1}(\mathbf{q}, \mathbf{q})} \tag{2.94}$$

2.3 Hardware and software

For all computer simulations, the very well-established and widely-used electronic structure VASP code in its latest version 5.4.4 is used [190, 200]. VASP is based on density functional theory (DFT) [1, 2] using the projector-augmented wave method [152] and a plane wave basis. SQS supercells were generated using the Alloy Theoretic Automated Toolkit (ATAT) software package [201]. Additionally, the Occupation matrix control algorithm was used to fix the issue of d-electrons delocalization [176]. In addition, Phonopy version 2.9.1 and Phono3py version 1.22, open source codes [94, 194] written in Python, are used to prepare sets of supercells with displaced atoms to be input to VASP for force computations of second- and third-order. Phonopy and Phono3py make extensive use of symmetry analysis, which allows for a reduction in the number of displacements needed. Finally, also with Phonopy and Phono3py force sets are collected and phonon frequencies and imaginary part of the self-energy are calculated.

All of the calculations were done on the GCS Supercomputer JUWELS at Jülich Supercomputing Centre (JSC) under projects **abinitiomodmatsgeo** and **geopressmagphon**, and on the GFZ Linux cluster GLIC. A standard compute node on the GCS Supercomputer JUWELS consists of 2× Intel Xeon Platinum 8168

CPU, 2× 24 cores, 2.7 GHz. VASP runs well on super-scalar processors, vector computers, and parallel computers. In particular, it has support for MPI-based parallelization with good scaling on multicore machines. To estimate resources for a VASP run, three fundamental numbers have to be taken into account: 1) number of **k**-points, 2) number of bands (determined indirectly by the number of atoms and electrons) and 3) size of the basis set (i.e., number of plane waves, which corresponds to the number of grid points in the fast Fourier transform (FFTs). To find the most optimal values, test simulations for every system of interest were performed with different tasks-per-node settings in the workload manager and tuning the corresponding VASP parameters. In terms of the number of nodes, in most cases, it was found that using 2 nodes (96 cores) for a job was the most optimal solution.

Chapter 3

Non-magnetic sulfides: CaS and MgS

In this chapter, the topic of optical properties of CaS and MgS is investigated with the main focus on calculating reflectivity in the IR region. The results presented in this chapter have previously been published [202]. The content appears either verbatim or slightly adjusted to this thesis.

There have been a few experimental and theoretical studies of the optical properties in the infrared region of CaS and MgS. From experimental investigations, data obtained from absorption spectra are used to determine various physical quantities such as reflectivity, emissivity [203, 204], etc. On the other hand, theoretical studies based on density functional theory (DFT) within the local density approximation (LDA) [112] have only modeled the atomic dynamics of these systems in the limit of the harmonic approximation [205, 206]. Unfortunately, the lack of neutron scattering studies on these sulfides makes impossible a direct comparison of the predicted phonon dispersions with their experimental counterparts. The only physical quantity directly comparable between experimental and modeling results is the splitting of the longitudinal and transverse optical modes, i.e., the

LO/TO splitting. This mode separation originates from the degeneracy elimination between the LO and TO phonons at the Brillouin-zone center [207]. In this regard, there is an overall reasonable agreement of reported measurements with predicted data (Table 3.1). However, the harmonic approximation predicts a reflectivity with a step-like behavior and sharp edges at both ends of the spectrum [93]. This predicted reflectivity is in drastic disagreement with experimental spectra, which appear with smeared edges, especially at the high-wavenumber tail. This inconsistency is a direct consequence of the simplifications made in the harmonic approximation and can be remedied by the inclusion of anharmonic effects. It has long been desired to introduce anharmonic effects in the first-principles atomic and molecular dynamics (MD) simulations. However, due to computational limitations, the explicit treatment of the phonon-phonon interactions has been limited, even though the analytical base has been available for a long time [95, 96]. But in the last decade, the significant increase in computational power and efficiency has made it possible to include anharmonic effects explicitly on a rigorous basis. One way to consider anharmonic effects in an MD simulation is by coupling the system to a thermostat of a given temperature [208, 209]. The consequent normal modes of motion contain the frequencies renormalized by the temperature, i.e., anharmonic interactions. Such an approach has been shown to remedy the negative frequencies persistent within the harmonic approximation in a few elemental systems [209]. The vibrational eigenfrequencies calculated in this way are "dressed" by anharmonic phonon-phonon interactions up to, formally speaking, all orders. Therefore, to estimate individual contributions, a mapping scheme onto an effective model, containing all the contributions separately needs to be constructed [210]. Alternatively, one might wish to introduce anharmonicity in a progressive and more controlled way. This implementation is achieved in a

perturbative manner based on the Cowley expansion [96]. At the lowest order, one obtains two three-phonon and one four-phonon contributions to the total energy as shown in Fig. 2.5(a)-Fig. 2.5(c). The main computational challenge to evaluate these Cowley diagrams is the calculation of their force constants of various orders. Nowadays, it is possible to compute them completely *ab intio* using density functional theory (DFT) [1, 2] by following one of two main approaches. The first method employs density functional perturbation theory [189], and the FC are expressed directly in terms of the electron density and its derivatives [211]. In the second one, the finite displacement method [191, 212], the FC are extracted by performing a series of self-consistent calculations for different atomic displacement patterns and using the Hellman-Feynman theorem. However, the main issue in this approach is computations growing rapidly, as a large number of configurations is needed for higher-order FC. The calculation of the FC of the m-th order requires $(6Nn_b)^m$ configurations, where n_b is the number of atoms in the lattice basis, and N is the number of primitive cells in the supercell [213]. Although this number can be substantially reduced by identifying equivalent displacement patterns using crystal symmetries [213, 214], it is still quite large, especially for the fourth-order FC.

In addition to the Cowley contributions to the anharmonicity, the effects derived from isotope-disorder scatterings have been shown to play an important role at low temperatures [193]. This isotopic scattering can also be formulated within the second-order perturbation theory [97]. In this framework, the unperturbed Hamiltonian, H_0, for the crystal is defined in the harmonic approximation with the atomic mass replaced by an averaged mass that depends on the number of unit cells in the crystal and the fraction of a given atomic isotope. Then, the perturbation, H_I, which depends on the deviation of the isotope mass from the average

mass, has its main contribution from the second-order term shown in Fig. 2.5(d). The first-order and other higher-order diagrams derived from H_I have either zero contribution (due to the average mass definition) or are not significant in comparison to the second-order term [97]. Therefore, to study the most substantial anharmonic effects in MgS and CaS, the FDM including only three-phonon processes and the isotopic scattering shown is used.

The rest of this chapter is structured as follows. In Section 3.1 the necessary elements to model the infrared response as well as the means to calculate them are summarized. The results on optical properties are presented in Section 3.2 and compared to available theoretical and experimental findings. Finally, in Section 3.3 the conclusions are made and the applicability of the approach used in this work to model infrared optical properties of other materials is argued.

3.1 Computational details

The main goal is to calculate the optical response of MgS and CaS in the infrared region using the generalized Lorentz model, with the dielectric function given by Eq. (2.78). The self-energy $\Pi_{j,0}(\omega)$ can be improved gradually according to the Cowley perturbative approach [96]. In this work, its expansion is restricted to the following form:

$$\Pi_{tot}(\omega) = \Pi_{3ph}(\omega) + \Pi_{isot}(\omega), \tag{3.1}$$

where Π_{3ph} is the anharmonic contribution to the total self-energy due to three-phonon scattering processes, and Π_{isot} is the isotope-disorder induced scattering (Figs. 2.5(a)-(b) and 2.5(d)). The three-phonon part of the self-energy consists of two terms known as the "bubble" and "tadpole" diagrams. The bubble term has both real and imaginary parts whereas the tadpole has only the real part. Thus,

the finite lifetime of the phonons due to the phonon-phonon interaction is solely determined by the imaginary part of the bubble (B) diagram, $\mathrm{Im}\left[\Pi^{B}_{3ph}(\omega)\right]$, which is the only term considered in our calculation. In general, the bubble diagram is not diagonal in branch indices jj', however, for the purpose of calculating optical properties, it is sufficient to consider only the diagonal terms [95]. The second term in Eq. (3.1) also contributes to the broadening of the harmonic frequencies. $\Pi_{isot}(\omega)$ is mostly visible at low frequencies and temperatures and, as shown in the next section for the sulfide systems in question, it becomes smeared out by the phonon-phonon interaction at high temperatures [97, 193].

The goal of this study is to model the reflectivity, which is characterized by a frequency band of high reflectivity, i.e., the reststrahlen band [207]. The top and bottom of this band are defined by the transverse (ω_{TO}) and longitudinal (ω_{LO}) optical modes, respectively. These frequencies can be calculated from the harmonic approximation alone by employing the non-analytical correction (NAC) at *almost* zero $\mathbf{q}$-vector [215]. It also means that the summation in Eq. (2.78) is reduced to only those modes that fall within the reststrahlen band, i.e., the transverse optical (TO) mode.

All calculations are performed using DFT and the projector-augmented plane wave method (PAW) [152] as implemented in the VASP code (version 5.4.4) [190, 200]. The valence configurations are $3p^6 4s^2$ for Ca, $2p^6 3s^2$ for Mg, and $3s^2 3p^4$ for S. The exchange-correlation (XC) term in the effective Kohn-Sham potential is approximated according to the Perdew-Burke-Ernzerhof parameterization for solids (PBEsol) [216] of the generalized gradient approximation (GGA) [115]. This election is based on previous studies on MnS [217] for which, LDA and PBE functionals were also tested but PBEsol was found to render the best structural properties. Both CaS and MgS crystallize into rock-salt (RS) cubic structure, and

their conventional unit-cells with 8 atoms are used. Integration in the Brillouin zone is done on a Γ-centered grid of uniformly distributed k-points with a spacing of $2\pi\times0.3$ Å^{-1}. The selected plane-wave kinetic energy cutoff is 500 eV and convergence of the structural optimizations is assumed when the total energy changes are less than 10^{-8} eV and the forces on each atom smaller than 10^{-3} eV/Å. The fully relaxed crystal structures (in unit-cell shape and ionic degrees of freedom) are used as the underlying unit-cells for the generation of atomic displacements. The displacement configurations are generated in accordance with the crystal symmetry as implemented in the *Phonopy* code [94]. The $2\times2\times2$ supercells are used, which contain 64 atoms, and to obtain second-order FC, two displacement configurations are sufficient. Then, the harmonic eigenfrequencies are calculated. The NAC is employed to estimate the size of the reststrahlen band. To compute the third-order FC necessary to calculate the self-energy, i.e., $\Pi^{B}_{3ph}(\omega)$ [95], the FDM method is used as implemented in the *Phono3py* code [194]. Unlike for the second-order FC, for the third-order case every pair of atoms in the supercell needs to be displaced, but in this instance, the crystal symmetry once again helps reduce the overall number of required configurations. The phonon interaction distance cutoff, i.e., the minimum distance allowed between displaced atoms in the original configuration, is determined to be 9.8 Å and 9.0 Å for CaS and MgS, respectively. These parameters allow us to achieve the maximum number of displacement patterns possible, that is, 146 unique displacement configurations for both systems. This condition of maximal displacement configurations is necessary to converge the self-energy. Finally, the self-energy is computed on a uniform $12\times12\times12$ $\mathbf{q}$-point grid, resulting in the overall number of 720 $\mathbf{q}$-points in the first Brillouin zone.

3.2 Optical properties

3.2.1 Harmonic approximation limit

Table 3.1: Lattice parameter (a), transverse and longitudinal optical modes (ω_{TO} and ω_{LO}), Born effective charge (Z) and high frequency dielectric constant (ϵ_∞) calculated in this work [*]. Theoretical and experimental data available in the literature are compared: †-Ref. [203], ♭-Ref. [204], ‡-Ref. [218], ⋆-Ref. [205], ⋄-Ref. [206], •-Ref. [219], ◁-Ref. [220], ▷-Ref. [221]. Note that in the Ref. [203], the so-called Szigeti effective charge, Z_S, is given instead of Z. The Born effective charge reported here can be obtained using the relationship [222, 223] $Z = \frac{(\epsilon_\infty+2)}{3} Z_S$. The high-frequency dielectric constant ϵ_∞ used in Ref. [203] and Ref. [205] was obtained from a semiempirical (SE) model in Ref. [220]. PP: Pseudopotential.

System	Method	a(RS) (Å)	ω_{LO} (cm^{-1})	ω_{TO} (cm^{-1})	$Z_{\mathrm{Ca,Mg}}$ (e)	ϵ_∞
CaS	PBEsol/FDM*	5.633*	341.6*	228.7*	2.350*	5.21*
	LDA/PP/FDM⋆,SE◁	5.67⋆	354⋆	284⋆	1.802•	4.15◁
	EXP1♭		417♭	232♭		4.58▷
	EXP2†	5.697†	342†	229†	2.111†	4.15◁
MgS	PBEsol/FDM*	5.18*	393.0*	240.6*	2.314*	5.54*
	LDA/PP/DFPT⋄	5.18⋄	397⋄	241⋄	2.35⋄	5.66⋄
	EXP1♭	5.200‡	435♭	240♭		4.80◁

Firstly, the dynamical properties of CaS and MgS within the harmonic approximation are analyzed. As was discussed above, it is imperative to establish correctly the bounds of the reststrahlen band needed subsequently to calculate the reflectivity. In Table 3.1, the predicted values for the lattice parameter a, the transverse ω_{TO} and longitudinal ω_{LO} optical modes, the Born effective charge Z, and the high frequency dielectric constant ϵ_∞ for CaS and MgS are summarized. Their computed phonon band spectra are shown in Fig. 3.1(a) and Fig. 3.1(b), respectively. The calculated phonon band structure for CaS is in good qualitative agreement with a previous LDA/Pseudopotential/FDM study [205] using the SIESTA implementation [224] as shown in Fig. 3.1(a). The main quantitative dif-

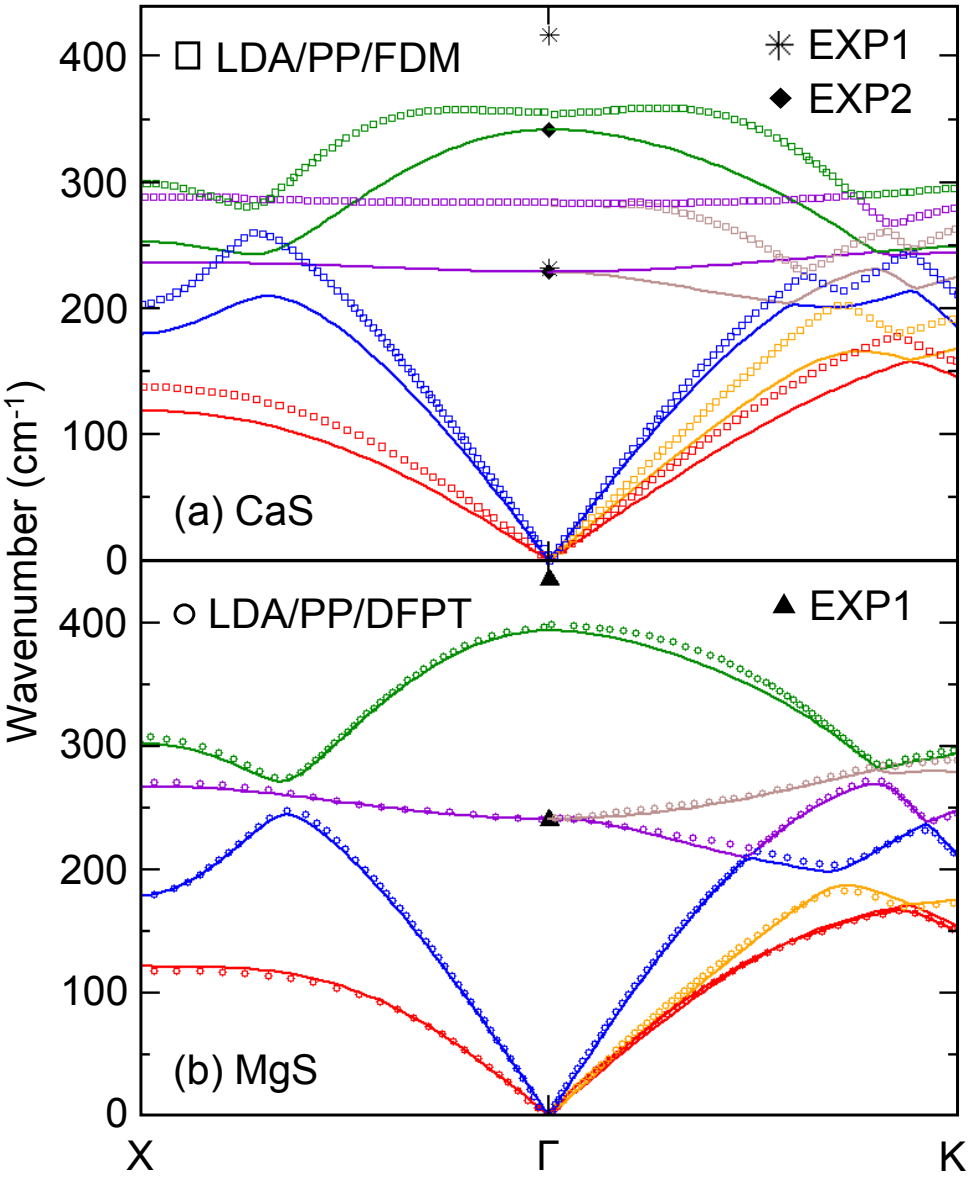

Figure 3.1: Our simulated phonon bands within the harmonic approximation are shown in solid lines for (a) CaS and (b) MgS. Different colors correspond to individual normal modes of motion: three acoustic bands (red, orange, and blue), and three optical bands (violet, brown, and green are the two TO and one LO mode, respectively). Hollow squares [205] (CaS) and hollow circles (MgS) [206] represent data taken from previous modeling studies. Experimental values shown in solid symbols for the TO and LO modes are denoted by EXP1 [204] and EXP2 [203].

ferences are due to lower frequencies predicted in our work for all phonon bands. This inconsistency in frequency magnitudes could be partially attributed to our slightly smaller lattice parameter $a_{\mathrm{CaS}} = 5.633$ Å with respect to $a_{\mathrm{CaS}} = 5.67$ Å of Ref. [205], which is in slightly better agreement with single crystal measurements [203] of $a_{\mathrm{CaS}} = 5.697$ Å. However, the calculated phonon band structure seems to be more consistent with experimental data [203, 204], as our predicted LO/TO splitting of 113 cm^{-1} agrees well with reported values of 113 cm^{-1} by Ref. [203]. From Table 3.1, it can be noticed that the two experimental studies find nearly the same value for ω_{TO}, but they differ in the magnitude of ω_{LO}. An apparent reason for this discrepancy could be traced back to the method employed to extract ω_{TO} and ω_{LO} from experiments. Both studies use a single oscillator model in their dispersion analysis and adopt an expression virtually identical to Eq. (3.1), but they treat the self-energy as frequency independent, giving it the role of a *damping constant*. In EXP1 [203] (in combination with ϵ_∞ taken from Ref. [221], the real and imaginary parts of the dielectric function, $\mathrm{Re}(\epsilon)$ and $\mathrm{Im}(\epsilon)$, are constructed from reflectivity data, then ω_{TO} and ω_{LO} are taken as the maxima of $\mathrm{Re}(\epsilon)$ and $\mathrm{Inv}[\mathrm{Im}(\epsilon)]$, respectively. On the other hand, in EXP2 [204] the TO and LO frequencies are treated as adjustable parameters to parameterize the reflectivity and fit the data. Thus, although the resolution of ω_{TO} seems to be independent of the method, the latter seems to be in better agreement with the current computation. Nevertheless, the calculated LO/TO splitting of 70 cm^{-1} by Ref. [205] is underestimated by at least 38% with respect to both measurements. This underestimation could be linked to their Born charge of $Z_{\mathrm{Ca}} = 1.802e$ and high-frequency dielectric constant $\epsilon_\infty = 4.15$ taken from Ref. [219] and Ref. [220], respectively. In contrast, the Born charge of this work $Z_{\mathrm{Ca}} = 2.350e$, calculated directly from the relaxed CaS structure, is much closer to the experimental value

of 2.111e. Here, it is clearly observed that a self-consistency among the required elements entering in the calculation of ω_{TO} and ω_{LO} is highly desirable, in particular, the LO/TO splitting is rather sensitive to the Born effective charge, as it enters the NAC as Z^2. An accurate determination of the TO mode is rather significant for the modeling of the reflectivity as it controls the edge of the reststrahlen band [207].

In the case of MgS, the predicted lattice parameter $a_{\mathrm{MgS}} = 5.180$ Å (Table 3.1) and phonon band spectrum, (Fig. 3.1(b)) are in excellent agreement with an earlier LDA/Pseudopotential/DFPT study [206] as implemented in the quantum espresso code [225]. The Born effective charge $Z_{\mathrm{Mg}} = 2.314e$ and high-frequency dielectric constant $\epsilon_\infty = 5.54$ are also in close agreement with the values found in Ref. [206] of $Z_{\mathrm{Mg}} = 2.35e$ and $\epsilon_\infty = 5.66$. These findings further support the idea that the main reason for the significant difference between our results and Ref. [205] in the case of CaS stemmed from the sizeable difference in the values of Z_{Ca} and ϵ_∞. However, the LO/TO splitting of 152 cm^{-1} obtained in this work, and the other *ab initio* value of 156 cm^{-1} are both, about 20% smaller than absorption spectra data [204] reporting a LO/TO splitting of 195 cm^{-1}. But, as discussed previously for the CaS system, the method used by Ref. [204] to determine ω_{TO} and ω_{LO} seems to give an overestimated value for ω_{LO} (Table 3.1), which could be the main source of divergence between the calculated and the experimental values.

3.2.2 Anharmonic effects

Next, the anharmonic effects and their role in the optical properties of CaS and MgS are discussed. As explained in the previous section, the only contributions to the self-energy that are considered are the three-phonon Π_{3ph} scattering processes

and the isotopic disorder Π_{isot}.

It can be noticed that the Π_{isot} contribution is only prominent at very low temperature, and its effect can be seen clearly in the imaginary part of the dielectric function, Im(ϵ), as shown in Fig. 3.2. More specifically, the isotope-disorder scattering manifests itself as an oscillatory behavior of the imaginary part of the dielectric constant, more prominently for MgS than for CaS, but distinctly evident for both compounds in the region between 150 and 220 cm^{-1}. Three-phonon processes are essentially absent at low temperature and low wavenumbers, thus the isotopic disorder is the leading term in this region. But as temperature increases, the three-phonon processes become dominant and smear out the isotope-disorder part. In addition, one can also observe the Im(ϵ) peak slightly shifting towards lower wavenumbers. Higher-order scattering processes (e.g., four-phonon contributions) are expected not to have a drastic effect on the computed Im(ϵ) of MgS and CaS. This assumption is in line with modeling results for MgO [193], as it was demonstrated that the four-phonon processes start being substantial at relatively high wavenumbers when the three-phonon contributions vanish.

The calculated reflectivity at three different temperatures for CaS and MgS is shown in Fig. 3.3. Here, one can immediately see the importance of the precise prediction of the ω_{TO} value, as it defines the reflectivity maximum. The width of the plateau at low temperature is mostly determined by the high-frequency dielectric constant ϵ_∞ and the Born effective charge Z. As temperature increases, both edges of the plateau smear out, although the change is much more obvious at the higher-wavenumber end. This effect is due to the anharmonic interactions, which become more notorious with increasing temperature. For MgS, Fig. 3.3(b), characteristic shoulders are observed between $\sim$325 cm^{-1} and $\sim$425 cm^{-1}. These features appear in MgO [193, 207] as well. It can also be noticed that for MgS,

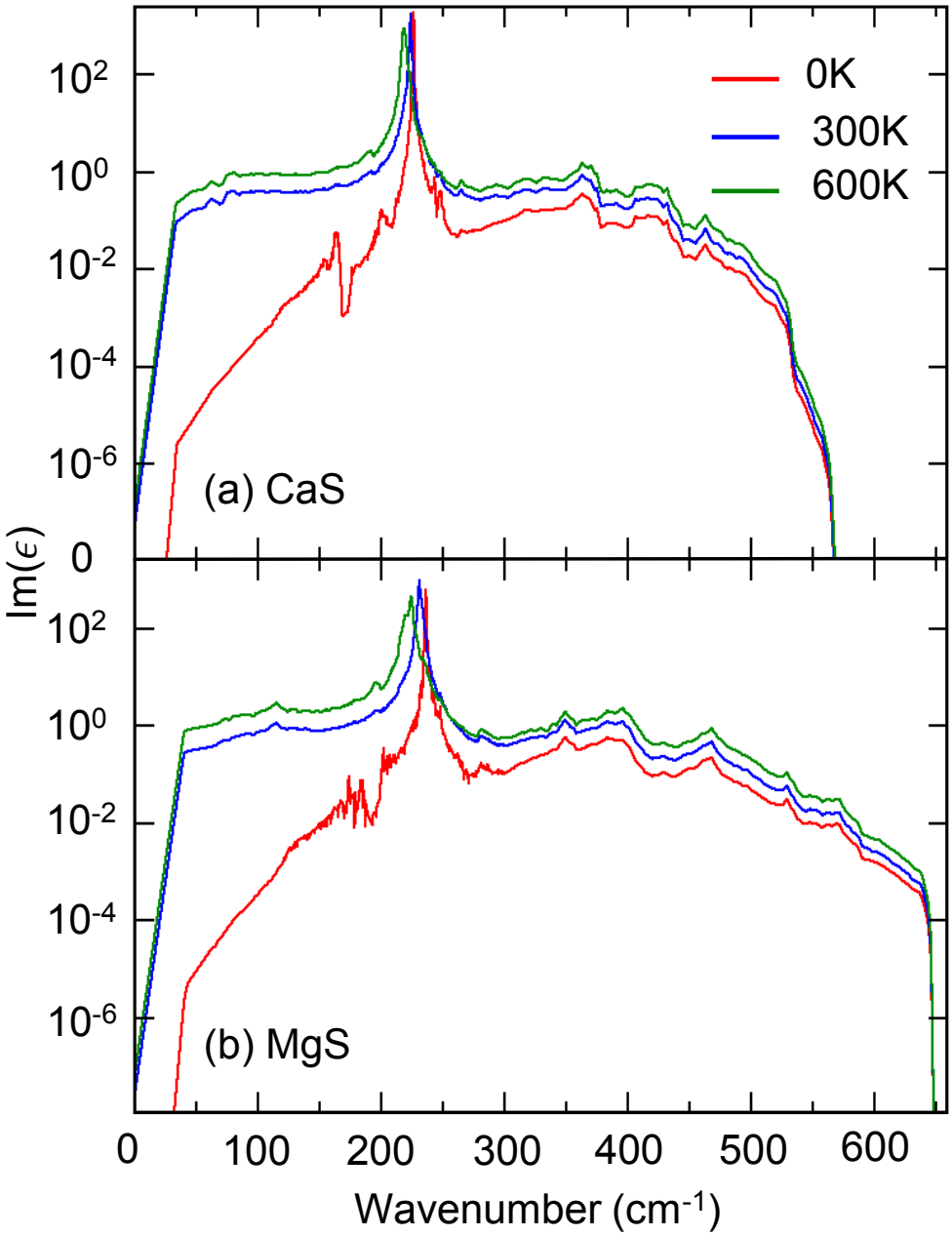

Figure 3.2: Calculated imaginary part of the dielectric function, Im[ϵ], for (a) CaS and (b) MgS at three different temperatures. The isotope-disorder scattering effects are responsible for the oscillatory behavior in the region 150-220 cm^{-1} and are only visible at sufficiently low temperature. The three-phonon processes prevail over Π_{isot} at higher temperatures.

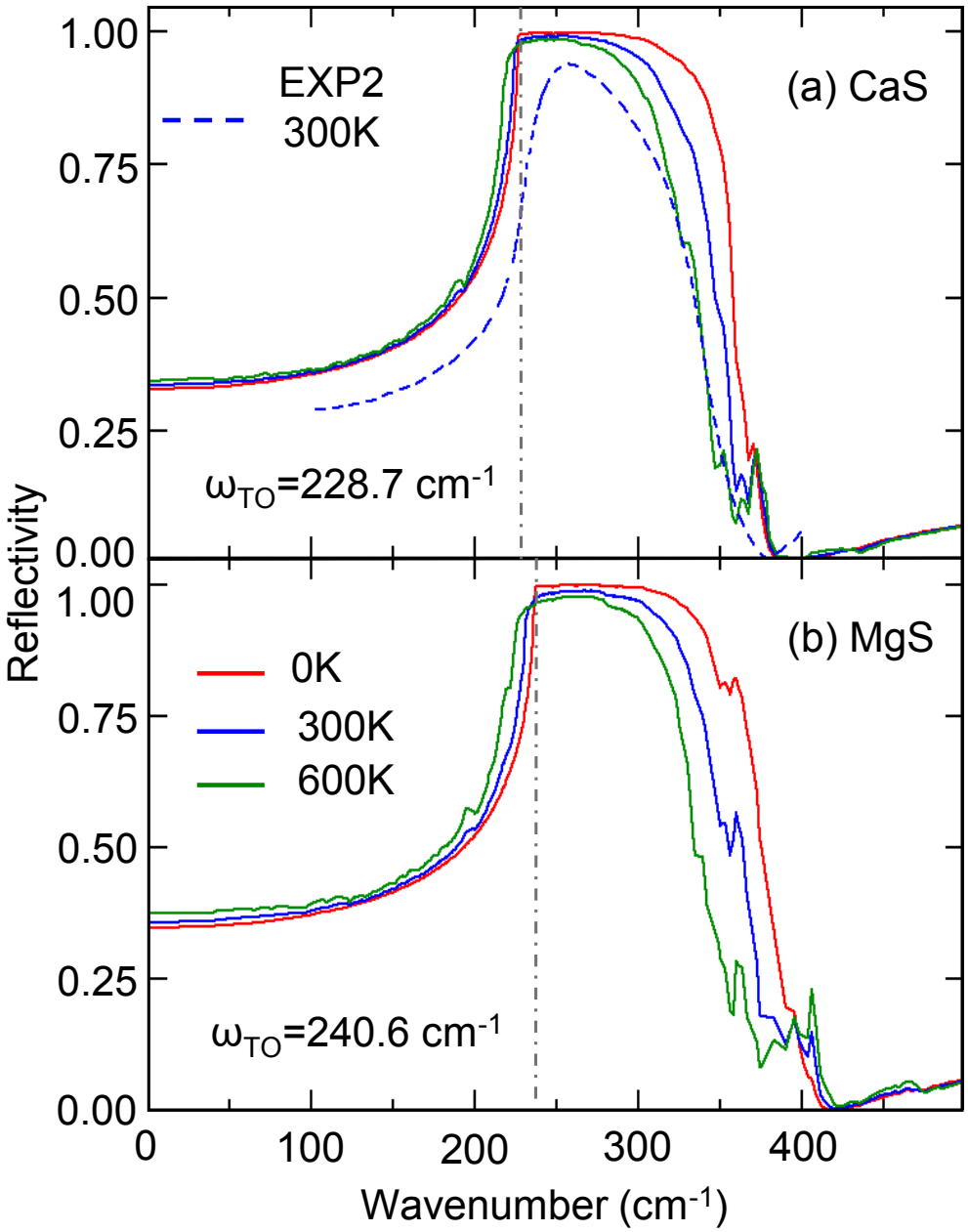

Figure 3.3: Predicted reflectivity (solid lines) for (a) CaS and (b) MgS at three different temperatures. For CaS, the results are compared to an experimental trend [203] (dashed line) at 300 K. The dotted-dashed gray lines indicate the position of our predicted ω_{TO} modes.

these shoulders show a somewhat spiky structure. For CaS, these shoulders are more prominent as temperature increases, that is, $\geq$ 300 K. The only available experimental report is on the reflectivity of CaS [203] as shown in Fig. 3.3(a). Compared to the reflectivity computed at 300 K, there is a good qualitative agreement with some systematic quantitative deviation. The predicted position of the TO peak is only 0.14% lower than the measured one at 229 cm^{-1}. In general, the experimental reflectivity values seem to be smaller than the simulation results in the region considered. It is highly unlikely that the inclusion of additional anharmonic terms in the Cowley expansion of Eq. (3.1) would reduce the overall magnitude of our predicted reflectivity. Namely, it is possible that the main cause for the overestimation of the reflectivity has its roots in the calculated force constants, and consequently, the estimated strength of the anharmonic effects. Perhaps, larger supercells could improve the overall FC values because they would allow for larger interaction distances between phonons, however, the computational cost would increase significantly. The other peculiar feature of the predicted reflectivity curves for CaS and MgS is the presence of several peaks in the high-wavenumber shoulders. Such structures are not observed in the experimental study on CaS [203], where all possible anharmonic effects are, of course, present. It is conceivable that the inclusion of higher-order phonon processes could remove these spiky structures in that region as it is shown in the case of MgO [193], in which both three- and four-phonon processes were included and a smooth computed reflectivity is achieved. Therefore, it can be argued that at the level of present simulations, both CaS and MgS seem to be more anharmonic in the sense that, more anharmonic terms are needed to be included in order to reach a better agreement with the experimentally observed reflectivity, but such studies are outside of our current resources and are left for future explorations.

At this point, it is worth mentioning that the experimental results used for comparison in the previous discussion are from single-crystal measurements. However, there are experiments in which, powdered (pressed pellets) samples are studied also with the infrared spectroscopy technique. This experimental approach is particularly relevant in planetary investigations, as *dust* is likely to be studied directly on the planet's surface thanks to spectrometers in missions or in simulated conditions in the laboratory [226]. However, the use of pressed pellets leads to scattering, and diffused reflection or refraction, resulting in an overall weaker reflectivity measurement [227]. It has been also observed that, sometimes, reflectivity spectra from powdered samples retain qualitative features of the reflectivity of single crystals, that is, the measured peaks do not shift in wavenumber but only decrease in magnitude [228]. In such a scenario, the harmonic modeling using the generalized Lorentz model can still be expected to be applicable but adjusted to measurements from sulfide powders, by modifying the number of oscillators and the damping coefficient. Thus, the self-energy (which plays the role of the damping factor) in Eq. (3.1) would be dominated not by anharmonic contributions but by processes specifically differentiating between single crystal and pressed pellets, e.g., scatterings, grain sizes, etc.

In recent years, a spectral library of sulfide minerals was initiated to support investigations of Mercury's surface chemistry, a study [226] reported reflectance (R) measurements of synthetic CaS and MgS powders in the range from far infrared (FIR) until visible (VIS), at Mercury's day surface temperature ($\sim$773 K). Reflectance is related to reflectivity in that the latter is the reflectance of a semi-infinite slab [193]. Therefore, a direct and straight comparison between their reflectance magnitudes is not possible, nonetheless, the position of their maxima, which should coincide, can still be investigated. The measured R maximum in

the FIR region for MgS (sample denoted "MgS-2" in Ref. [226]) occurs at the wavelength of 40 μm, equivalent to a wavenumber of 250 cm^{-1}. In comparison, the predicted maximum of the reflectivity is at 240 cm^{-1} and 300 K. Finally, for CaS, the reflectance measurements [226] position its peak at a wavelength of about 8 μm, that is, a wavenumber of about 555 cm^{-1}, this value is in drastic disagreement with our calculated position for the reflectivity peak at 228.7 cm^{-1} and the single crystal measurements [203, 204] of 229 and 232 cm^{-1}. This sharp difference in the position of the maxima from reflectance and reflectivity could be due to the use of CaS powder in the case of the reflectance experiment [226], however, further experiments would be necessary to clarify the discrepancy.

3.3 Conclusions

In summary, a full first-principles study of the reflectivity of CaS and MgS in the infrared region has been conducted. Both harmonic and anharmonic contributions have been considered. Within the harmonic limit, the non-analytic correction was used to obtain the correct LO/TO splitting. An accurate determination of the TO and LO peaks is highly desirable as they provide the boundaries of the rest-strahlen band, i.e., the low- and high-frequency edges of the maximum reflectivity. The effects of the anharmonicity have been included by considering three-phonon scatterings and isotope-disorder processes at the lowest perturbation level. The anharmonic terms' main influence occurred in the smear of the reflectivity spectra's edges, being more prominent in the higher-wavenumber region.

Although higher-order anharmonic terms have not been included, e.g., four-phonon scatterings, it is reasonable to assume that these processes would be only noticeable in the high-wavenumber region of our study, outside of the maximum reflectivity peak, as it has been shown to be the case for MgO [193]. However,

these higher-order anharmonic terms could eliminate the spiky structures in the predicted reflectivities. Finally, it might be worthwhile to try to incorporate the anharmonic terms into the modeling of the polycrystalline and powder samples. Although, in this case, they are expected to play a secondary role since the self-energy, i.e, the damping constant would be dominated by processes that are characteristic of powder pellets such as diffused reflection and refraction.

Chapter 4

Magnetic sulfides: MnS polymorphs

Some of the results presented in this chapter, in particular Sec. 4.2, have been published [217].

The main goal of this chapter is to model the optical response of a series of PM MnS polymorphs in the FIR region. As before, this requires the calculation of a set of forces, which are extracted from DFT calculations for displaced configurations. However, in the case of MnS the electronic structure modeling is complicated by the presence of $d-$electrons, which give rise to local magnetic moments. As was mentioned previously, modeling PM state as non-magnetic is often inadequate and leads to qualitatively wrong behavior, e.g., a system exhibits metallic features instead of insulating [187, 188]. An incorrect electronic ground state would undoubtedly produce interatomic forces, which cannot be considered reliable. In order to model the PM state of MnS polymorphs, a combination of DFT and SQS is employed. The goal here is to show that without resorting to specialized theories of highly correlated materials beyond on-site corrections (DFT+U), the insulating PM phase of MnS can be achieved by introducing magnetic disorder

using SQS. Also, occupation matrix control methodology to handle localization of Mn d-states is used [176]. In this way, comparable physical properties such as lattice parameter, energy gap, and local magnetic moment to those observed experimentally are produced. Additionally, using different PM MnS polymorphs' ground states as candidates for high-pressure phases, their enthalpies as a function of pressure are calculated in order to pinpoint possible structural transformations of B1-MnS. The PM MnS polymorphs' structures are constructed and optimized following the SQS formalism previously described.

Having confirmed that DFT+SQS method is able to produce PM states with physical properties comparable to those measured in the experiment, this method can be used to calculate interatomic forces for displaced atomic configurations, which are then used to calculate the phonon band structure. The main difficulty here is that the phonon bands can be very sensitive to various magnetic orderings, and might produce soft modes. This issue can be overcome by considering progressively more complex SQS constructs, i.e., structures with higher-order figures and larger interaction distances, Fig. 2.2. This procedure is explained in great detail in Sec. 4.3. After finding stable SQS for each of the polymorphs of interest, the anharmonic effects can be introduced in the same fashion as in the previous chapter for CaS and MgS.

The remainder of this chapter is structured as follows. The computational details regarding both the electronic structure calculations, phonon bands, and reflectivity are given in Sec. 4.1. In Sec. 4.2, the electronic structure of MnS polymorphs is discussed. Finally, the optical properties of B1-, B4 and B31-MnS are presented in Sec. 4.3.

4.1 Computational details

All of the calculations were performed within DFT+U, using the projector-augmented plane wave method (PAW) [152] as implemented in the VASP (version 5.4.4) code [190, 200]. The valence configurations were $4s^1 3d^6$ for Mn, and $3s^2 3p^4$ for S, respectively. The exchange-correlation (XC) term in the effective Kohn-Sham potential was approximated according to the Perdew-Burke-Ernzerhof parameterization for solids (PBEsol) of the generalized gradient approximation (GGA) [216]. To treat the Coulomb repulsion of the Mn d-electrons, the Hubbard-U correction [136] was added within the rotationally invariant Dudarev prescription, Eq. (2.39), which can also be written as [147]:

$$E_U = \frac{U}{2} \sum_{I,\sigma} \sum_{i} \lambda_i^{I,\sigma} (1 - \lambda_i^{I,\sigma}). \tag{4.1}$$

As it is well known, E_U represents a penalty energy proportional to U (here U represents the effective difference between the on-site Coulomb and exchange interactions) for atom I and spin channel σ. $\lambda_i^{I,\sigma}$ are the eigenvalues (with values between 0 and 1) of the occupation matrix (OM) $n_{m,m'}^{I,\sigma}$ for an orthogonal set of localized orbitals i, which, in general, are the linear combinations of the atomic d-orbitals m. For all simulations a value of $U = 3$ eV was chosen, as it was already tested for the AFM B1-MnS phase at 0 GPa [175]. The local density approximation (LDA) [112] and the standard PBE [119] XC functionals +U were also assessed, but it was found that PBEsol+U produced structural parameters that were in better agreement with available experimental values for both AFM and PM phases of MnS. Therefore, only results within this scheme are presented in the remaining sections.

Integration in the Brillouin zone was done on a Γ-centered grid of uniformly dis-

tributed k-points with a spacing of $2\pi\times0.3$ Å^{-1}. The selected plane-wave kinetic energy cutoff was 500 eV and convergence of the structural optimizations was assumed when the total energy changes were less than 10^{-8} eV and the forces on each atom smaller than 10^{-3} eV/Å.

To simulate magnetic ordering (AFM below T_N) and disordering (in PM phases at T_R) large enough supercells have to be built in order to accommodate the appropriate AFM orderings as well as to allow for multiple relaxation patterns. These two features have been shown to lead to gap opening in TM oxides and perovskites [187, 188]. Overall, four MnS polymorphs were considered, namely, RS (B1, $Fm\bar{3}m$), wurtzite (WZ or B4, $P6_3mc$), GeS-type (B16, $Pnma$) and MnP-type (B31, $Pnma$).

To model the structures below T_N, the AFM-II and AFM-III orderings observed experimentally in the B1 and B4 polymorphs, respectively, were imposed [54]. For the B16- and B31-MnS structures there is no experimental or computational data on their precise magnetic ordering, except for one report stating that the B31 polymorph is PM above 5 K [83]. Consequently, several possible AFM arrangements were tested and the lowest energy configurations were adopted. All MnS polymorphs structures were optimized using 64-atom $2\times2\times2$ supercells, except for B4-MnS, for which a 36-atom $3\times3\times1$ supercell was sufficient to realize the experimentally observed AFM-III ordering.

On the other hand, to model the PM MnS polymorphs, SQS supercells were constructed using the ATAT software package [201]. Under this scheme, the PM state is created as a disordered alloy of *up* $\uparrow$ and *down* $\downarrow$ moments located at different sites. As the construction of an SQS is based on the computation of the correlation function between the species that constitute the alloy ($\uparrow$ and $\downarrow$ moments in this case), the size of the supercell (number of atoms) used is vitally important

to obtain magnetic configurations whose components are not spatially correlated among themselves. The SQS *degree of randomness* is improved by the number of atomic figures (pairs, triplets, quadruplets, etc.) included in the calculation of the correlation function and by the interaction distance between the atoms in a given figure. For example, one could start by only considering nearest neighbors for atomic pairs, then gradually add more pairs (increasing the interaction distance), and/or higher order figures into consideration. The larger the interaction distance and the more figures are considered, the larger the supercell becomes to achieve *total randomness*, and the SQS generation quickly becomes computationally demanding. Because the creation of an SQS is purely configurational, in order to save resources, for this study a previously produced SQS supercell for the B1 structure of TM oxides [187] with 64 atoms was used. For the B16- and B31-MnS polymorphs, pairs and triplets were included to obtain 64-atom 2×2×2 SQS's supercells. Similarly, for the B4 structure, 2×2×2, 3×3×2 and 4×4×1 supercells with 32, 72 and 64 atoms, respectively, were tested resulting in ground state energy differences among them of less than 10^{-3} eV per formula unit (f.u.), thus, the 32-atom supercell was taken.

Finally, under pressure (P) it turned out to be impossible to converge some PM MnS structures to stable ground states. In order to deal with this obstacle, it has been noticed that non-integer occupancies in Eq. 4.1 may lead to local minima and not allow a system to achieve its true ground state. Thus, by *controlling* orbital filling explicitly in $n^{I,\sigma}_{m,m'}$, one can *help* a non-converging trapped system circumvent a metastable OM ill-setup. This method was shown to find stable states, previously inaccessible, for d and f oxides [176]. Therefore, in the current collinear magnetism approach, to keep the magnetic ordering as determined at 0 GPa, and at the same time isolate energy changes due only to structural trans-

formations for $P > 0$ GPa, for a given Mn ion in all polymorphs the same diagonal unitary occupation of its d_m orbitals ($m = -2, -1, \ldots, 2 \Rightarrow 5{\times}5$ matrices) was specified using the "occupation-matrix-control-in-VASP" algorithm [176]. In this way, the formerly problematic cases were able to converge.

4.2 Electronic structure

4.2.1 AFM ordering in MnS

First, DFT+U optimized MnS polymorphs with the AFM ordering considered for each structure are shown in Fig. 4.1. The predicted lattice parameter $a_0 =$ 5.172 Å for B1-MnS (Fig. 4.1(a)) is only ∼0.8% smaller than its experimental counterpart of 5.212 Å [54]. As it was mentioned in Chapter 1, the AFM-II onset in the B1-MnS structure leads to a trigonal distortion, the degree of this distortion can be estimated by the magnitude of the cube corner angle given by $\frac{\pi}{2}+\Delta$, where Δ measures the deviation from the ideal cubic symmetry. For the relaxed B1-MnS polymorph the distortion was found to be $\Delta \approx 0.095°$, which is in good agreement with the observed deviation of $0.099° \pm 0.015°$ [72]. For the hexagonal B4-MnS polymorph the lattice parameters $a_0 = 3.963$ Å and $c_0 = 6.437$ Å were obtained, which are in excellent agreement with experimental values of $a_0 = 3.987$ Å and $c_0 = 6.438$ Å [54]. The optimized volumes per f.u. for each MnS polymorph are listed in Table 4.1 for comparison and show that B4-MnS is the least dense.

As it is well known, computed DFT band gap energies (Eg) are ordinarily underestimated, but from the simulations in this work it was found that all MnS polymorphs are clearly insulating, as can be seen from E_g values in Table 4.1. For B1-MnS a band gap value of $E_g = 2.0$ eV was obtained, which is to some extent, in better agreement with the experimental value of about 3.1 eV [229], than reports

Table 4.1: Computed volume V per formula unit (f.u.), energy gap E_g, and local magnetic moment m_{loc} of MnS polymorphs with AFM configurations.

Magnetic Ordering	Polymorph		V/f.u. (Å^3)	E_g (eV)	m_{loc} (μB)
AFM-II	RS	B1	34.58	2.0	4.45
AFM-III	WZ	B4	43.76	2.4	4.43
AFM	GeS	B16	34.66	2.1	4.45
AFM	MnP	B31	34.38	1.6	4.42

of $E_g = 1.36$ eV as predicted from KKR-CPA [230], $\sim$1 eV from Perdew-Wang (PW) GGA without U [231], and $\sim$1.5 eV from GGA-PW+U, with $U = 3$ eV [175]. Overall, these findings imply that the magnitude of E_g increases with V/f.u., with the hexagonal B4-MnS polymorph having the largest energy band gap, while the orthorhombic B31-MnS structure the most narrow (Table 4.1).

The projected density of states of Mn s and d orbitals for all MnS polymorphs are shown in Fig. 4.2. The band characters are assigned roughly by looking at the m, l orbital quantum numbers and considering the crystal-field splitting observed for the point group symmetries of the respective structures. For simplicity in this symmetry analysis, spin and magnetic anti-unitary operators are not considered. Of course, one could do a complete formal analysis using magnetic point groups and magnetic irreducible co-representations [232] if one were after a thorough understanding of the bands, but for the purpose of this study it is not necessary. It should be noted, however, that the onset of the AFM ordering lowers the site symmetry, leading to additional lifting of orbital degeneracies. For example, the d-states of octahedrally coordinated Mn^{2+} in B1-MnS split into two levels, a high energy doublet (e_g^2) and a low energy triplet (t_{2g}^3). Here, the band gap is opened between e_g–majority and t_{2g}–minority bands, Fig. 2(a). However, the onset of AFM-II ordering lowers the symmetry from octahedral O_h to rhombohedral D_{3d}, resulting in the additional splitting of the t_{2g} states into a singlet and a doublet.

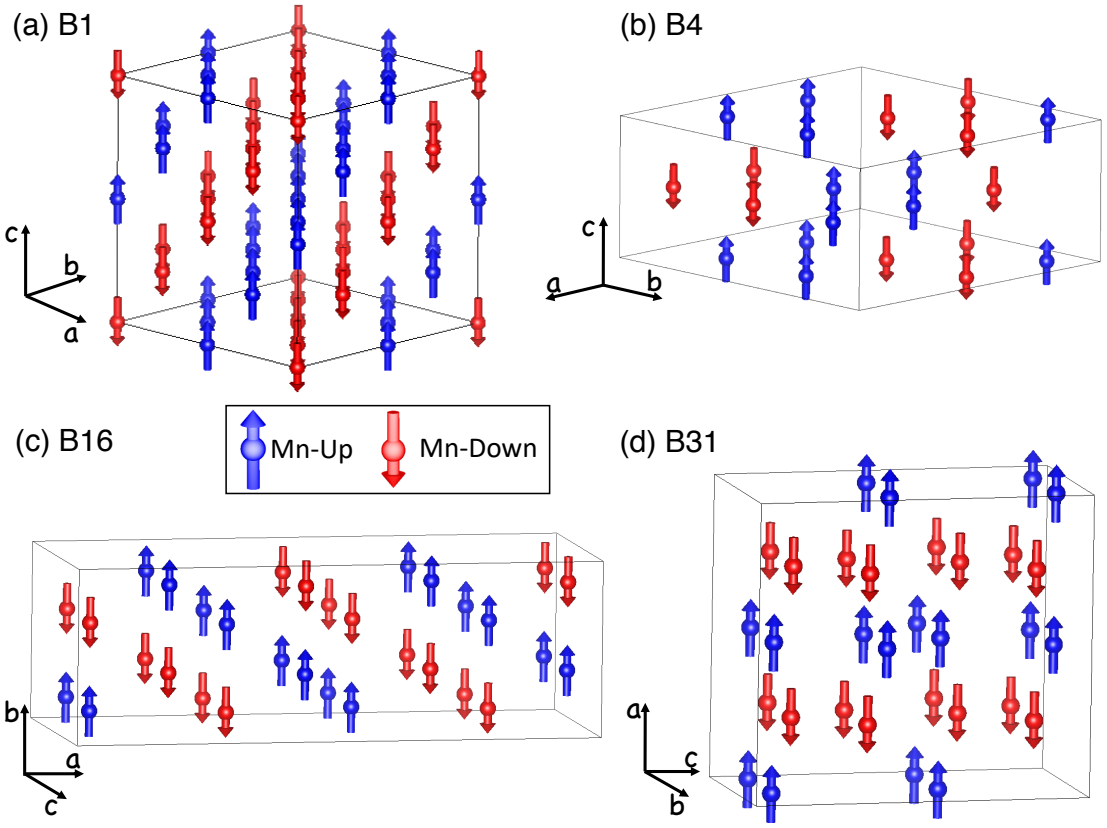

Figure 4.1: AFM arrangements in the MnS polymorphs investigated in this work. (a) B1 with AFM-II ordering and (b) B4 with AFM-III ordering were observed experimentally [54]; AFM configurations for the (c) B16 and (d) B31 polymorphs were generated in this study for comparison. S atoms are not shown for simplification. Structures are visualized using VESTA [20]

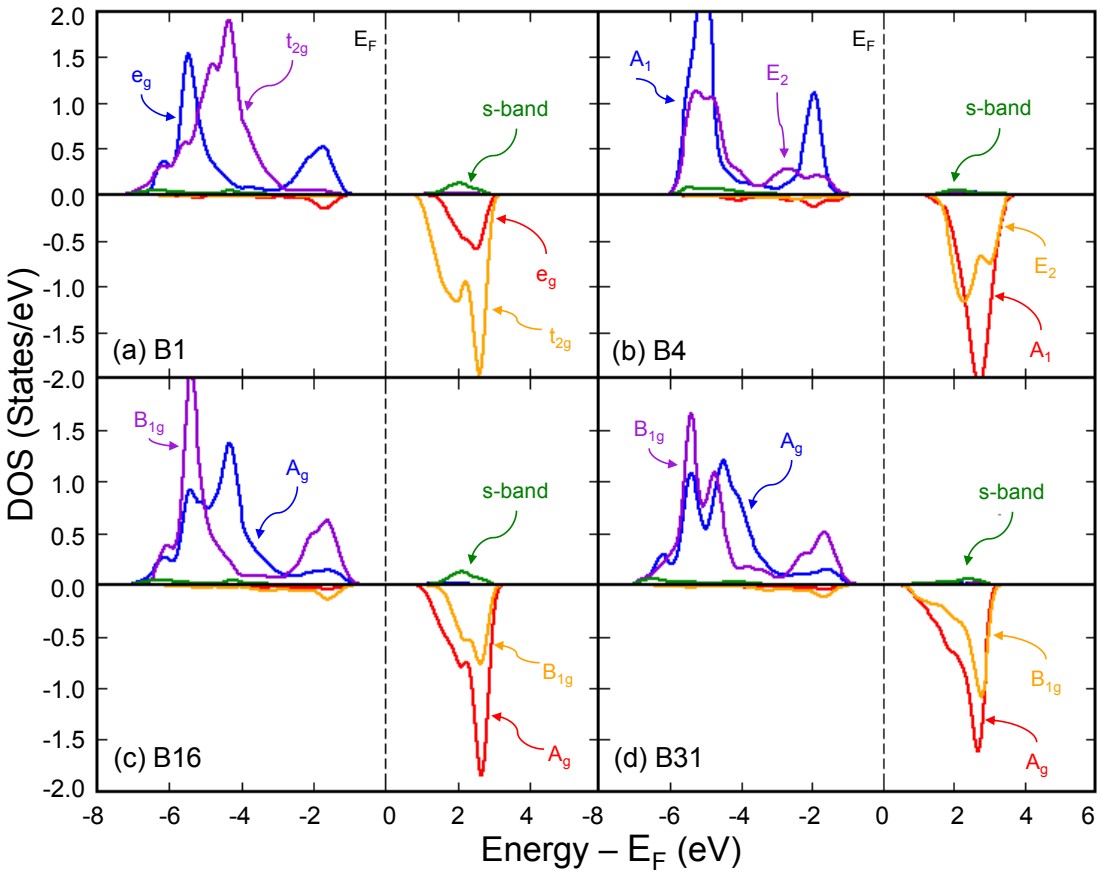

Figure 4.2: DFT+U local density of states (LDOS) for an Mn ion projected on the majority spin (positive) and minority spin (negative) channels with $U =$ 3 eV within AFM configurations for (a) B1, (b) B4, (c) B16 and (d) B31 MnS polymorphs. The Fermi energy (E_F) level is represented by the dashed line at zero. The characters of the d-states are interpreted through group theory analysis of the corresponding crystal-field surroundings before the onset of the AFM order. This is done for the purpose of comparison with the PM case. AFM ordering lowers the symmetry as follows: in B1 $O_h \rightarrow D_{3d}$, in B4 $C_{6v} \rightarrow C_{1h}$, in B16 $D_{2h} \rightarrow C_{2h}$, and in B31 $D_{2h} \rightarrow C_{2h}$.

In B4-MnS the hexagonal crystal field splits the d-shell into a singlet A_1 and two doublets E_1 and E_2. According to the calculation, in this structure the band gap is opened between the A_1–majority singlet and the E_2–minority doublet, Fig. 2(b), while the AFM-III ordering lowers the original C_{6v} site symmetry to C_{1h}. Lastly, both B16- and B31-MnS structures belong to the same D_{2h} point group. The orthorhombic crystal field of this symmetry lifts the five-fold degeneracy of the spherical d-shell leading to five singlets. Fig. 4.2(c) and (d) show that the band gap is opened between B_{1g}–majority and A_g–minority bands in both phases.

As can be seen from Table 4.1, the calculated local magnetic moments of the four AFM-MnS polymorphs are very similar in magnitude. For B1-MnS we find a $m_{loc} = 4.45$ μB, which is in much better agreement with experimental observations of 4.54 μB [53] than earlier calculations of 4.92 μB under a Hartree-Fock scheme [233], 4.39 μB from KKR-CPA [230], and 4.082 μB within GGA-PW [231].

4.2.2 Magnetically disordered PM MnS

The calculated MnS polymorphs in PM states as modeled by the construction of SQS are shown in Fig. 4.3. It is worth emphasizing the fact that in the calculations all degrees of freedom (lattice parameters and ionic positions) were allowed to relax, unlike other studies using SQS structures for TM oxides in which the symmetry and volume were kept fixed [187]. At first sight, these constrictions may appear reasonable to apply, as experimentally, there is no observable distortion from the cubic symmetry of the PM B1-MnS polymorph. Yet, allowing full relaxations in ionic coordinates and lattice parameters of the SQS structures and comparing them to their respective ideal symmetry could be a criterion to judge how *well* the created SQS represents its polymorph. For example, for PM B1-

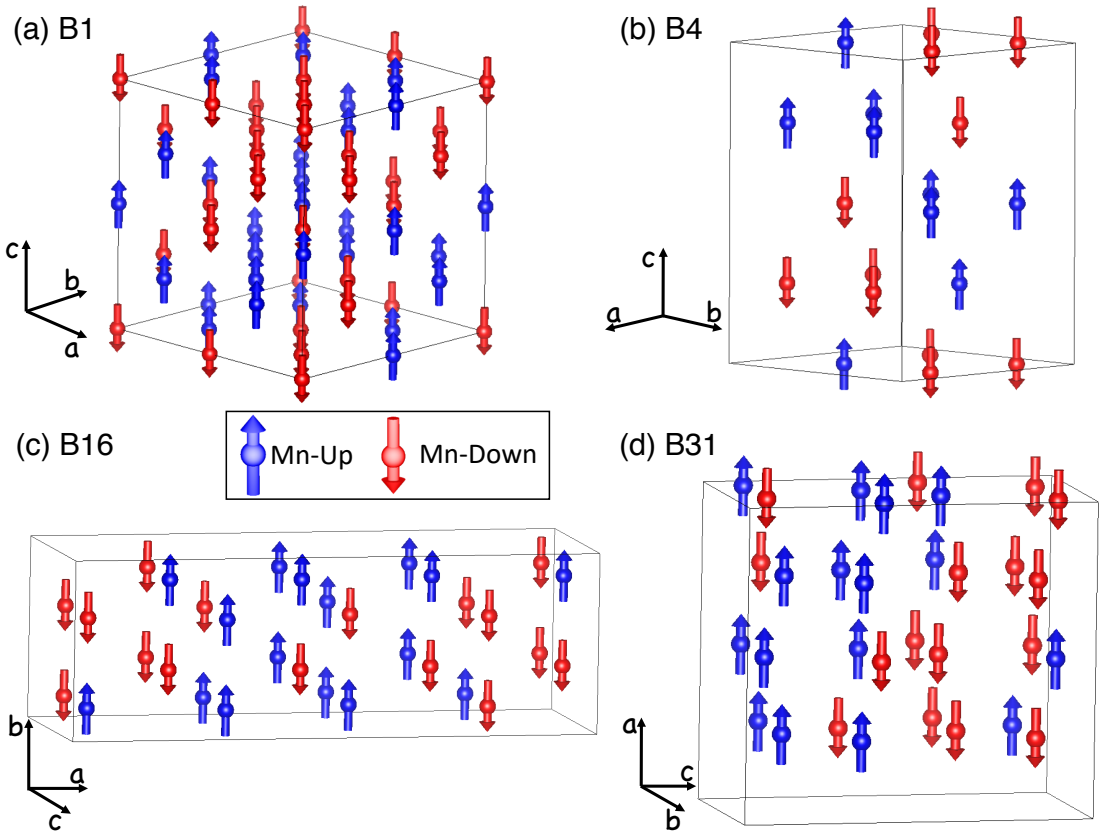

Figure 4.3: Generated SQS supercells representing the PM state of MnS polymorphs as an alloy of randomly distributed Mn ↑ and ↓ magnetic moments for (a) cubic B1, (b) hexagonal B4, and orthorhombic (c) B16 and (d) B31 structures. S atoms are not shown for simplification. Structures are visualized using VESTA [20].

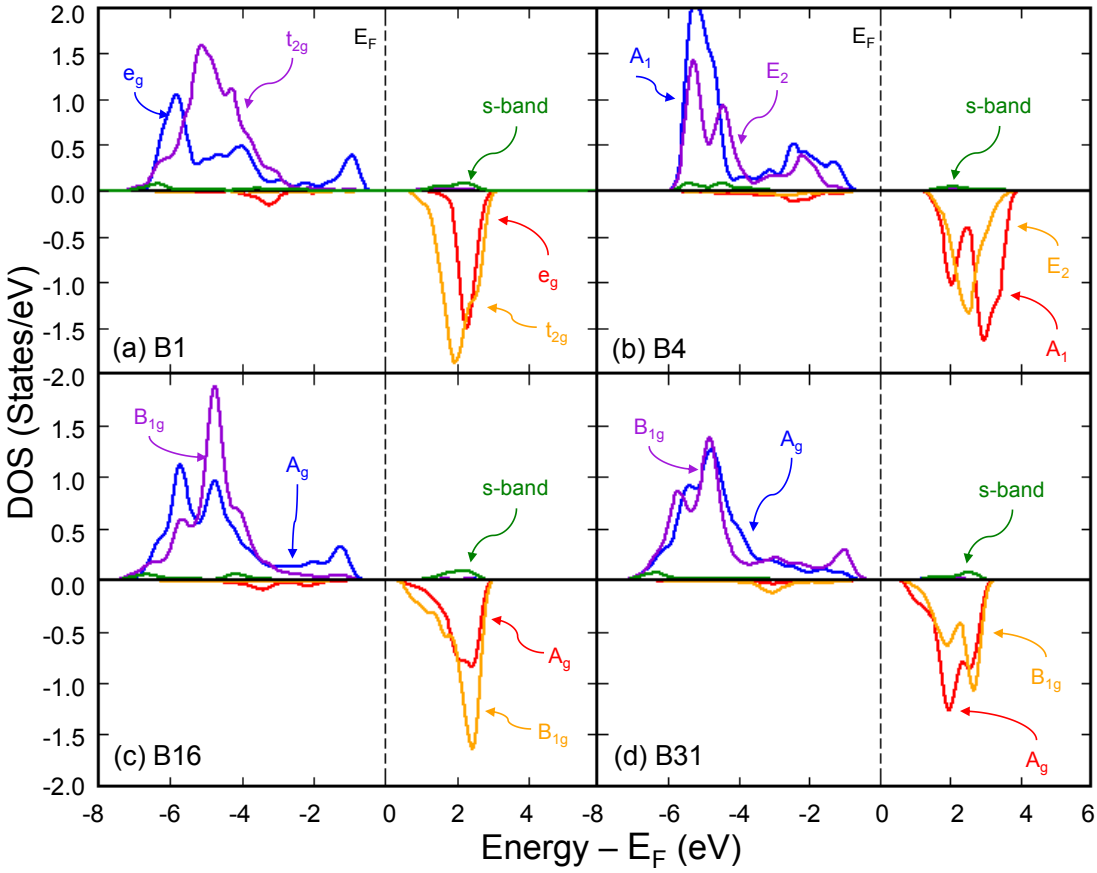

Figure 4.4: DFT+U partial density of states (DOS) for a Mn ion projected on the majority spin (positive) and minority spin (negative) channels with $U = 3$ eV within PM SQS's for (a) B1, (b) B4, (c) B16 and (d) B31 MnS polymorphs. The Fermi energy (E_F) level is represented by the dashed line at zero.

MnS (Fig. 4.3(a)) it was found that, as in the case of AFM order, there is a small trigonal distortion. The computed deviation from the ideal cubic angle for the used 64-atom SQS supercell is $\Delta \approx 0.024°$, whereas for a 216-atom SQS supercell the deviation with $\Delta \approx 0.003°$ was obtained, one order of magnitude smaller than for the 64-atom SQS supercell. Using the B1 64-atom and 216-atom SQS's the lattice parameters of $a_0 = 5.181$ Å and 5.1807 Å were found, respectively. These values are somewhat underestimated, but still in good agreement, with respect to measurements of 5.225 Å [81], 5.225 Å [82], and 5.29 Å [83]. Similarly to the AFM-ordered MnS phases, all PM MnS polymorphs were found to be insulators,

although with smaller energy band gaps (Table 4.2) than their AFM counterparts (Table 4.1). The PM E_g values (Table 4.2) suggest, however, that magnetic disorder affects the least the energy band gap of the hexagonal B4-MnS polymorph in comparison to its AFM analog, while B16-MnS shows the largest E_g reduction. It should be highlighted that even though for B1-MnS the predicted $E_g = 1.4$ eV is fairly underestimated as compared to the observed values of 2.7 eV [234] and 2.8 eV [229], PM B1-MnS phase is insulating, unlike other calculations in which it was found to be metallic [230, 235].

Finally, examining the calculated local magnetic moments in the PM phases listed in Table 4.2, a slight increase in magnitude can be seen when compared to the results in the AFM structures (Table 4.1). For the PM B1-MnS, the predicted value is 4.50 μB.

Table 4.2: Computed volume V per formula unit (f.u.), energy gap E_g, and local magnetic moment m_{loc} of MnS polymorphs in PM state.

Magnetic Ordering	Polymorph		V/f.u (Å^3)	E_g (eV)	m_{loc} (μB)
PM	RS	B1	34.76	1.4	4.50
	WZ	B4	44.06	2.3	4.44
	GeS	B16	36.94	1.2	4.50
	MnP	B31	34.94	0.9	4.46

To understand better the decrease in the magnitude of the PM energy band gaps with respect to the AFM cases, the projected density of states of an Mn ion in the PM state of the four MnS polymorphs are shown in Fig. 4.4. The calculations show that the introduction of magnetic disorder in the MnS polymorphs *spreads and produces* new spin-majority and spin-minority states in the E_g range of the AFM ordered phases (Fig. 4.2). Consequently, magnetic disorder exclusively (as the occupation matrix is constrained) *forces* a shift of the Fermi energy level in reference to the ordered AFM cases, but in such a way that the resulting PM MnS

phases remain insulating and hence with smaller energy band gaps. In principle, different magnetic disorder given by distinct SQS's would give rise to different energy band gap openings. This effect was reported in the context of NbMnSb by disordering Mn and Ni with respect to the sites they occupy in the ordered phase [236]. Additionally, in Fig. 4.4(a) and (c) one can see that for PM B1- and B31-MnS phases, the energy band gap opens, as in their AFM analogs, between the e_g–majority and the t_{2g}–minority bands, and between B_{1g}–majority and A_g–minority, respectively. However, for PM B4- and B16-MnS phases, magnetic disorder changes the character of the band gap openings in reference to their AFM counterparts, to be between A_1–majority and A_1–minority (Fig. 4.4(b)), and A_g–majority and B_1–minority (Fig. 4.4(d)), respectively.

4.2.3 AFM to PM evolution of the band gap

More insights into the narrowing of the band gap of PM MnS can be gained by introducing the magnetic disorder gradually. This task is accomplished by studying in more detail the projected Mn DOS for a couple of configurations slightly departing from the original AFM ordering.

Below, the results focusing solely on the B1-MnS structure are presented, although for the other three polymorphs a similar analysis would also apply. Two cases of *slight disorder* in the AFM-II 64-atom supercell of B1-MnS are investigated before achieving a fully disordered PM structure. First, a structure in which a couple of Mn atoms with antiparallel magnetic moments (D1-disorder) are swapped in a 180^o chain is considered, and then a structure with two of such swaps (D2-disorder) is studied, as shown in Fig. 4.5. For simplification, long-range interaction effects between neighboring unit cells are excluded. To isolate the system's reaction to disorder, all relaxation effects are also suppressed and only the Γ-point is used

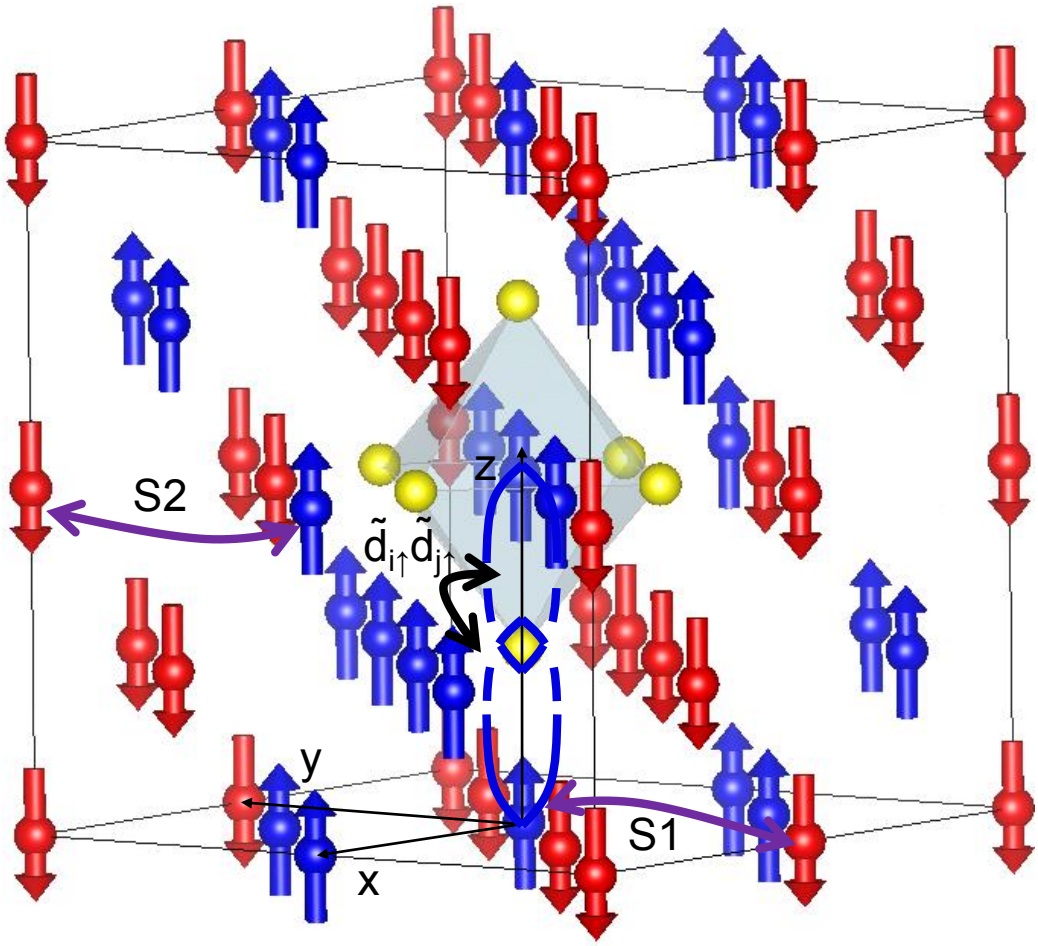

Figure 4.5: Representation of *slight* deviations from the AFM-II ordering. Blue-up and red-down arrows are Mn atoms with ↑- or ↓-magnetic moment, yellow balls are S atoms. The violet lines indicate two cases of introducing "magnetic disorder" by swapping Mn atoms of opposite magnetic moments. In the text, a structure with D1-disorder corresponds to having only one pair of Mn-↑ and Mn-↓ swapped (S1), whereas a structure with D2-disorder has swaps S1 and S2 as indicated. Half-solid-half-dashed loops depict *p*-*d* hybridized orbitals. When two Mn atoms with parallel magnetic moments are coupled through a 180^o Mn↑-S-Mn↑ bond, an additional coupling between *d*-derived orbitals also occurs $\tilde{d}^{\dagger}_{i\uparrow}\tilde{d}_{j\uparrow}$.

in the self-consistent calculation cycle. Taking the converged ground state for the AFM-II B1-MnS phase as the reference state, in which the largest non-zero hybridization integrals in Eq. 2.31 arise between Mn *d*-orbitals, and *s*- and *p*-orbitals of S (Fig. 4.6(a)), it is observed that upon introducing D1-disorder (i.e., after the creation of an FM coupling in one of the 180^o chains, Fig. 4.5), there

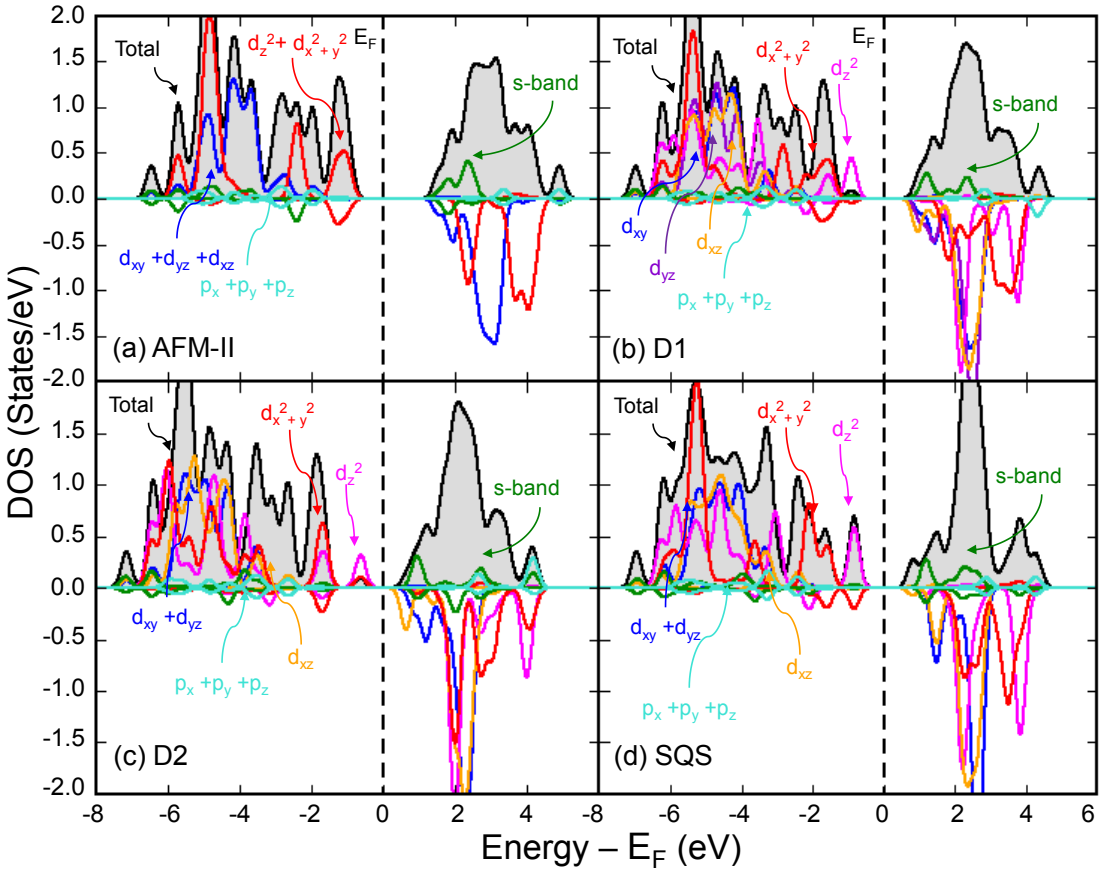

Figure 4.6: Orbital-projected density of states on the majority spin (positive) and minority spin (negative) channels with $U = 3$ eV of four different configurations of the B1-MnS with increasing level of disorder. The magnitude of the p-states is magnified by a factor of three for visibility. (a) The DOS of the AFM state is largely determined by the p-d and s-d hybridizations between S and Mn-centered orbitals. (b) and (c) The shrinkage of the band gap in the spin-majority channel is mainly caused by the formation of a 180^o Mn-↑-S-Mn-↑ chain that is absent in the AFM case. Additionally, there is also splitting in the t_{2g}-derived states. This is mostly determined by the overall number of Mn atoms with parallel magnetic moments in a given plane. For example, the structure D2 has the same number of Mn-↑ atoms in xy and yz planes which is why degeneracy in these states is observed, whilst this number is different in all planes in D1. (d) The fully random SQS structure exhibits the features of D1 in the e_g splitting whilst retaining the $xy + yz$ degeneracy shown in D2.

is now a possibility of additional combination between p-d hybridized orbitals of neighboring Mn sites with parallel magnetic moments. This *re-hybridization* seems to greatly contribute to the lift of the degeneracy of the t_{2g}- and e_g-derived

states and the spreading and pushing of the latter at the top of the valence band, effectively shrinking the energy gap as shown in Fig. 4.6(b). The effect of this re-hybridization in the *shift* of e_g states is more pronounced when D2-disorder (with S1 and S2 swaps) is considered (Fig. 4.6(c)). However, once that a number of swaps occur randomly and the PM state is reached in the SQS of B1-MnS, the energy band gap reaches its final magnitude. Another possible mechanism of re-hybridization, also partially responsible for the lift of the t_{2g} degeneracy, can take place within planes. In the AFM-II Mn d-orbitals hybridize with p-orbitals of S ions located at 90^o. That is, according to SK rules, in octahedral geometry d_{xy} orbitals hybridize only with p_x and p_y in the (010) and (100) directions, as shown in Fig. 4.7(a). However, when the nearest Mn neighbors have parallel magnetic moments, there is an additional coupling between the p-d hybridized orbitals as depicted in Fig. 4.7(b). Such re-hybridization is made possible through the admixture of p-states that provide the necessary *spatial extension* of the otherwise highly localized d-states. These re-hybridized $\tilde{d}$-orbitals centered on the Mn atoms can further mix with each other provided there is enough spatial overlap between them. In such a case, the t_{2g} degeneracy is predominantly determined by the number of Mn atoms with parallel magnetic moments in xy, yz, and xz planes, i.e., if this number is different for two given planes the degeneracy between the respective orbitals is lifted, Fig. 4.6(b)-(c).

4.2.4 High-pressure landscape of MnS polymorphs

As discussed before, room-temperature experimental studies of the stability of the B1-MnS polymorph under pressure, have reported a structural change to a new phase. However, the results were not conclusive as the transition pressure and the new phase were not uniquely determined [80–82]. Therefore, in order to examine

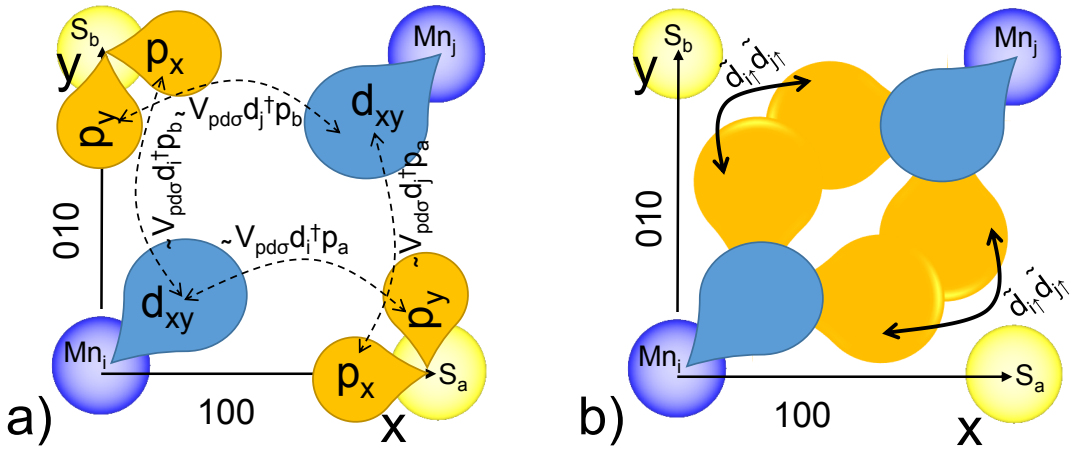

Figure 4.7: Schematic coupling between d-derived orbitals of neighboring Mn sites. (a) In AFM-II B1-MnS, d-orbitals hybridize with p-orbitals of sulfur ions S_a and S_b in the (010) and (100) directions, respectively. (b) Nearest Mn neighbors with parallel magnetic moments allow for an additional coupling between p-d hybridized orbitals ($\tilde{d}_{i\uparrow}\tilde{d}_{j\uparrow}$). When the number of Mn atoms with parallel magnetic moments in the xy-, yz- or xz-plane is changed through disorder, the respective orbital degeneracy is lifted.

the likelihood of a pressure-induced structural phase transformation of B1-MnS, for each MnS polymorph the enthalpy (H) as a function of pressure (P), volume (V), and internal energy (E) were computed, namely:

$$H(P) = E[V(P)] + PV(P). \tag{4.2}$$

The relative enthalpy ΔH per f.u. of the MnS polymorphs studied here with respect to the B1-MnS structure, i.e., $\Delta H = H(\text{MnS-phase}) - H(\text{B1})$, as a function of pressure between 0 and 60 GPa is shown in Fig. 4.8. Although high-pressure experiments at T_R deal with the PM phases of MnS results for both AFM and PM polymorphs are presented. On one hand, the computed static ΔH values suggest that if we were at a sufficiently low temperature to achieve AFM ordering for all MnS polymorphs, B31-MnS would be the most stable phase at 0 GPa, and

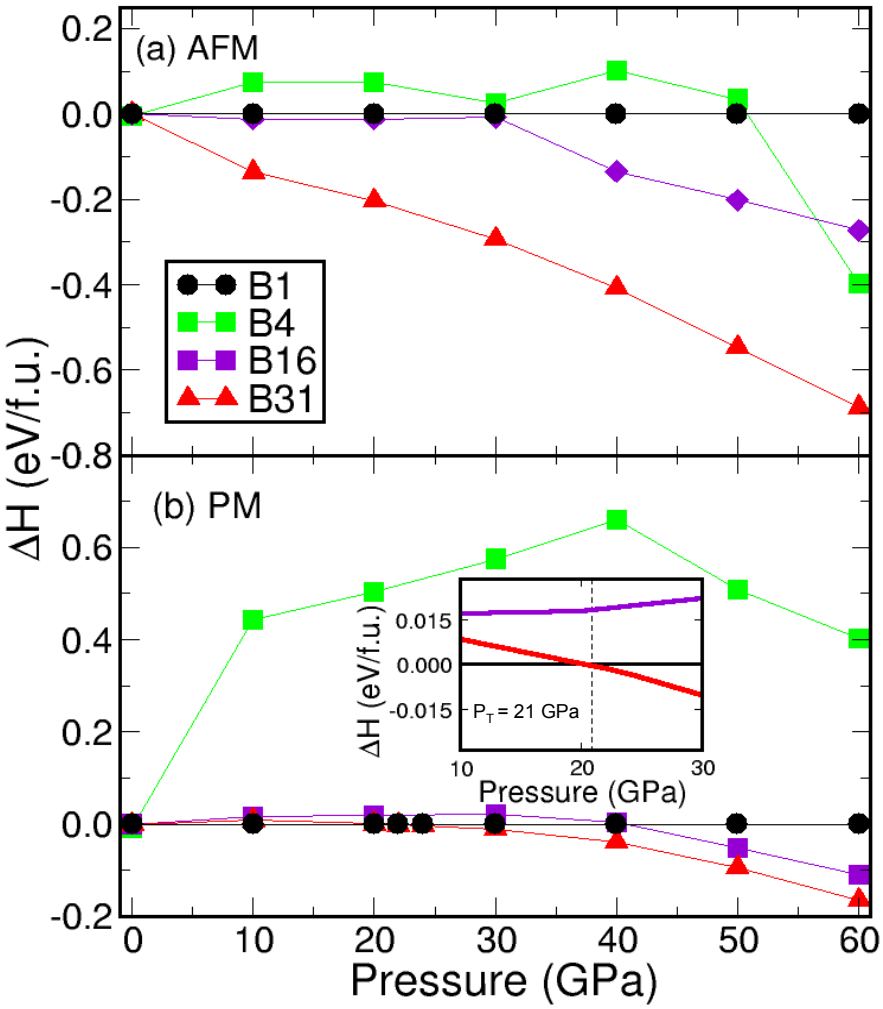

Figure 4.8: Static PBE+U relative enthalpy ΔH per f.u. between different (a) AFM and (b) PM states of MnS polymorphs. All results are given in reference to the B1 structure.

it would remain so up to 60 GPa, Fig. 4.8(a). On the other hand, from our static calculations of the enthalpy in PM phases of MnS, Fig. 4.8(b), it can be concluded that the RS structure B1-MnS is the most stable phase at ambient conditions, but as pressure increases, it undergoes a transformation to the orthorhombic B31-MnS polymorph at $P_T \approx 21$ GPa, as illustrated for clarity by the inset in Fig. 4.8(b). The predicted P_T in bulk B1-MnS is in close agreement with the experimentally observed structural transformation of B1-MnS to an unidentified phase with lower symmetry than hexagonal (B4-MnS) at ∼26 GPa [82]. Our determined B1→B31

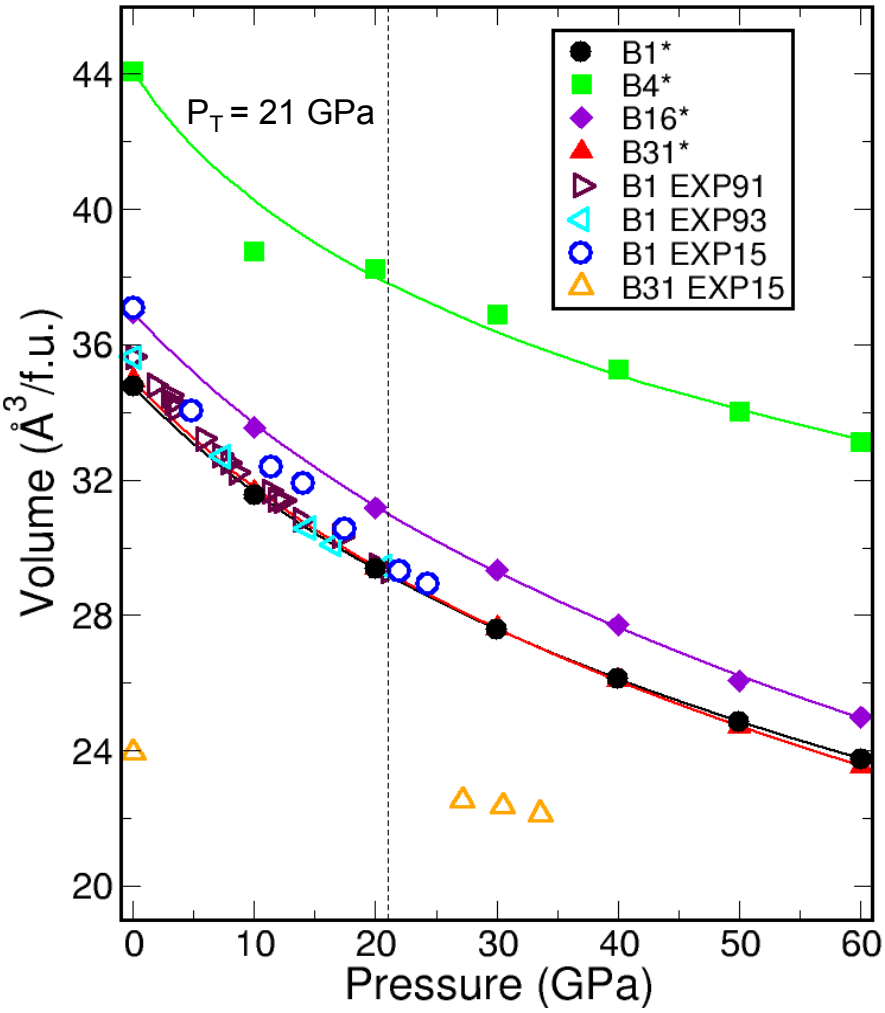

Figure 4.9: Pressure dependence of volume per f.u. for all PM MnS polymorphs as predicted by the computations. The PM MnS results [⋆] are compared to experimental values: EXP91 [81], EXP93 [82], and EXP15 [83]. The dashed line indicates the predicted transition pressure (P_T = 21 GPa) at which B1→B31. Solid lines are fits of the 3rd order Birch-Murnaghan's equation of state to the calculated volumes.

transformation was also established at about 22.3 GPa in experiments synthesizing high-pressure MnS nanorods [83], in which these B31-MnS nanorods were quenchable to 0 GPa. Furthermore, static LDA+U DFT calculations (with an effective U = 5.13 eV) performed alongside the experimental study found that, although the B1- and B31-MnS polymorphs are energetically very close below 8 GPa, B31 is the most stable at all pressures between 0 and 40 GPa. However, unlike in our

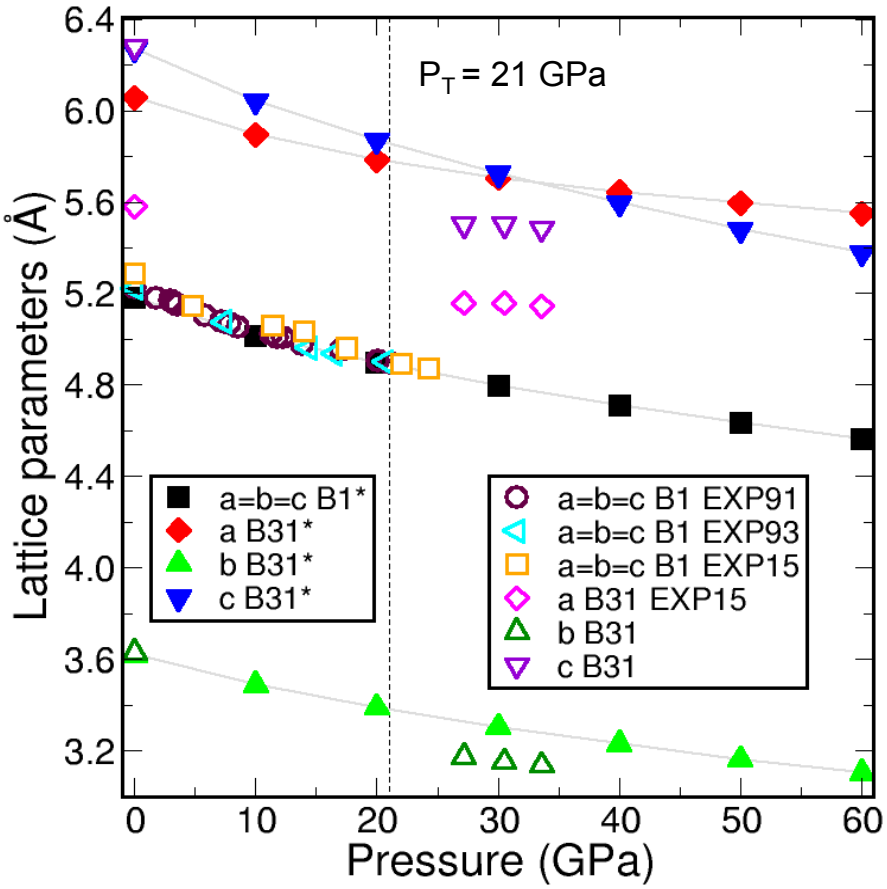

Figure 4.10: Lattice parameters as a function of pressure for cubic B1- and orthorhombic B31-MnS structures. Static PBE+U results [$\star$] of our magnetically disordered PM polymorphs are compared to experimental values: EXP91 [81], EXP93 [82], and EXP15 [83]. The dashed line indicates our predicted transition pressure ($P_T = 21$ GPa) at which B1$\rightarrow$B31.

static PBEsol calculations using the constructed magnetically disorder SQS PM states of MnS, the former LDA+U modeling [83] does not specify how the PM was simulated. It should be noticed as well, that the four PM polymorphs considered here, at the level of current calculations, are remarkably close in energy at 0 GPa, but the B1 possesses the absolute lowest energy per f.u., and as pressure increases, B16 and B31 enthalpies increase slightly and then decrease to start competing for stability against the B1-MnS structure, with B31-MnS eventually becoming more stable at $P_T \approx 21$ GPa. The predicted behavior from the computations for the

AFM MnS polymorphs' enthalpy trends are surprisingly in qualitative agreement with the LDA+U modeling of the B1- and B31-MnS phases [83]. The predicted change in volume per f.u. with increasing pressure for the PM MnS structures modeled in this study is shown in Fig. 4.9. As can be seen, the experimental volumes for cubic B1-MnS [81, 82] are exceptionally consistent with the findings of this work. The largest deviation from the computed V/f.u. occurs for B31-MnS with respect to measurements provided from high-pressure experiments on MnS nanorods [83]. As a consequence of the B1→B31 structural transformation, from the calculated trends a decrease in volume of MnS of only approximately 2% at P_T is obtained. This volume reduction, however, is one order of magnitude smaller in contrast to the one observed in the B31 nanorods [83].

A closer look at the pressure dependence of the predicted lattice parameters for the B1-MnS shows that the values calculated in this work are in excellent agreement with available experimental data [81–83], as can be seen in Fig. 4.10. In the case of B31-MnS, the calculated a, b, and c lattice constants are systematically overestimated by about ∼10%, ∼5% and ∼4%, respectively, in comparison to experimental values at high pressures [83]. At 0 GPa, the agreement between the results obtained in this work and the experimental values becomes much better for a_0 and b_0, but curiously the calculated value of c_0 is ∼8% larger than the only measurement reported up to date [83].

Lastly, the bulk modulus at 0 GPa (K_0) was obtained from Birch-Murnaghan's third-order equation of state (EOS) fittings to the $P - V$ data between 0 and 60 GPa. The predicted $K_0 \approx 92$ GPa (with its pressure derivative $K_0' = 3$) for PM B1-MnS is in reasonable agreement with the experimental value reported of 88±6 GPa as fit with a variable K_0' [82]. Our result is, however, overestimated by almost 20%, when the experimental data is fit using a constant $K_0' = 4$. A

comparison between the computed bulk moduli indicates that B1-, B16-, and B31-MnS polymorphs oppose almost indistinguishable resistance against volume compression under hydrostatic pressure, while B4 is the easiest to compress with a $K_0 \approx 57$ GPa.

4.3 Optical properties

In this section, the results on the optical properties of the B1-, B4-, and B31-MnS polymorphs are presented. Firstly, the vibrational properties are studied within the harmonic approximation, to investigate the dynamical stability of various SQS supercells. It is imperative for the modeling of the anharmonic effects that the constructed SQS supercells do not contain soft modes. To this end, different SQS configurations with increasing complexity, i.e., with higher-order figures of larger orders are examined. After stable SQS supercells are found, the anharmonic effects are introduced to compute the dielectric function and reflectivity of the selected PM MnS polymorphs.

4.3.1 Harmonic approximation

As previously stated, an accurate calculation of the phonon self-energy requires a soft-mode-free band structure, since the presence of negative frequencies would indicate dynamical instabilities and lead to erroneous results for the dielectric function, reflectivity, etc. Systems with local magnetic moments can be rather sensitive to different magnetic configurations and might produce fictitious soft modes. Considering that the systems of interest are known to be stable structures at room temperature, it is reasonable to expect that there exists at least one magnetic configuration that yields a phonon band structure without soft modes. However, the number of possible arrangements of local magnetic moments is practically infi-

nite, therefore, a consistent search scheme for stable magnetic configurations is necessary.

As before, the PM state of all systems of interest is modeled as an alloy of randomly distributed "up" and "down" local magnetic moments. This distribution is achieved by using the SQS method. Increasingly more complex SQS supercells need to be considered until a stable configuration is found. The complexity of a given SQS structure is determined by the type of figures $f(k, m)$, Fig. 2.2, which are used to generate the cell. The search scheme can be summarized as follows:

1. An SQS configuration is generated for a given size supercell and figure type $f(k, m)$.

2. The phonon band structure for this configuration is calculated within the harmonic approximation and checked against the presence of the soft modes.

3. If soft modes are present, a more complex SQS structure is generated. As a general rule, the order k from the previous run is kept, and the interaction distance m is increased. Only the "perfect" SQS configurations are considered. Thus, if a critical value for m is reached for a given vertex k, for which it is no longer possible to generate a "perfect" SQS, then the next vertex k is introduced.

4. Alternatively, going beyond a critical m value for a given vertex k, would need larger size of the SQS supercell.

5. Steps 1-3, or if needed step 4, are repeated until a soft-mode-free SQS is found.

Another important feature of the phonon band structure calculation in magnetic systems is the aspect of the symmetry of the underlying lattice. Generally, an SQS

cell of randomly distributed magnetic atoms will have a lower symmetry than the non-magnetic primitive cell. In this case, a larger number of displacements is needed to construct the interatomic force constant matrix. The SQS supercell also contains a larger number of atoms, which leads to more modes of motion, i.e., more phonon bands. On the other hand, experimental studies of vibrational frequencies of magnetic systems using, for example, neutron scattering reveal the phonon bands that correspond to the non-magnetic primitive cell. Therefore, it is clear that the dynamical matrix should be diagonalized for the underlying primitive cell with the inclusion of the effects of local magnetic moments. Here, this condition is satisfied by generating displaced configurations for the non-magnetic primitive cell. The distribution of local magnetic moments, as determined by SQS method, is then included in the displaced configurations for the calculation of the interatomic forces. This approach allows to preserve the underlying symmetry of the primitive cell and includes the effect of magnetism. The physical justification for such a method lies in the different time scales of atomic vibrations and spin flips [185, 237]. Spin flips, which govern the fluctuation of local magnetic moments, happen much faster than atomic vibrations. In other words, by the time an atom completes one period of oscillations, it will have undergone several magnetic configurations. Therefore, an atom would "see" the average effect of all possible arrangements of local magnetic moments, resulting in the symmetry preservation of the underlying non-magnetic primitive cell. This approximation is similar in spirit to the Born-Oppenheimer approximation, in which the same argument is used for decoupling electronic and atomic degrees of freedom.

Table 4.3: Parameters used for SQS construction

Structure		Size	Type of figure $f(k,m)$				Soft modes
			k=2	k=3	k=4	k=5	
B1	SQS-1	4×4×4	$m = 7.00$	–	–	–	B point
	SQS-2	4×4×4	$m = 7.00$	$m = 5.00$	$m = 5.00$	–	Γ point
	SQS-3	4×4×4	$m = 7.00$	$m = 5.00$	$m = 5.00$	$m = 5.00$	None
B4	SQS-1	2×2×2	$m = 5.00$	$m = 12.00$	–	–	Γ point
	SQS-2	4×4×1	$m = 6.20$	–	–	–	None
B31	SQS-1	2×2×2	$m = 4.00$	$m = 6.00$	–	$m = 4.23$	Γ point
	SQS-2	2×2×2	$m = 4.00$	$m = 6.00$	–	$m = 5.30$	Γ point
	SQS-3	2×2×2	$m = 4.00$	$m = 6.00$	–	$m = 6.00$	Γ point
	SQS-4	2×2×2	$m = 4.00$	$m = 6.00$	–	$m = 5.30$	None

B1-MnS polymorph

The SQS structures tested for the B1-MnS polymorph, as well as their calculated phonon band dispersions, are shown in Fig. 4.11. The face-centered cubic lattice (FCC) was used as the underlying primitive cell with two atoms instead of the conventional simple cubic lattice used in the study of pressure-induced phase transitions. The choice of the FCC lattice is purely for technical reasons as it makes the introduction of the anharmonic effects more convenient. The optimal soft-mode-free structure for the B1-MnS phase was found by progressively increasing the type of figures (parameter k in $f(k,m)$) to generate the SQS configurations, Table 4.3. The SQS-1 structure, which was obtained considering only pairs of atoms ($k = 2$), displays soft modes of large magnitude around point B in the BZ, Fig. 4.11(a). Including more complex figures such as triplets ($k = 3$) and quadruplets ($k = 4$) almost eliminated all negative frequencies, Fig. 4.11(b). However, there are still some soft modes of low magnitude at the Γ-point. This case is quite typical for the phonon bands of magnetic systems which are modeled using the SQS technique and have been also observed in other systems. Finally, with the inclusion of $k = 5$ figures, it was possible to obtain a phonon band structure

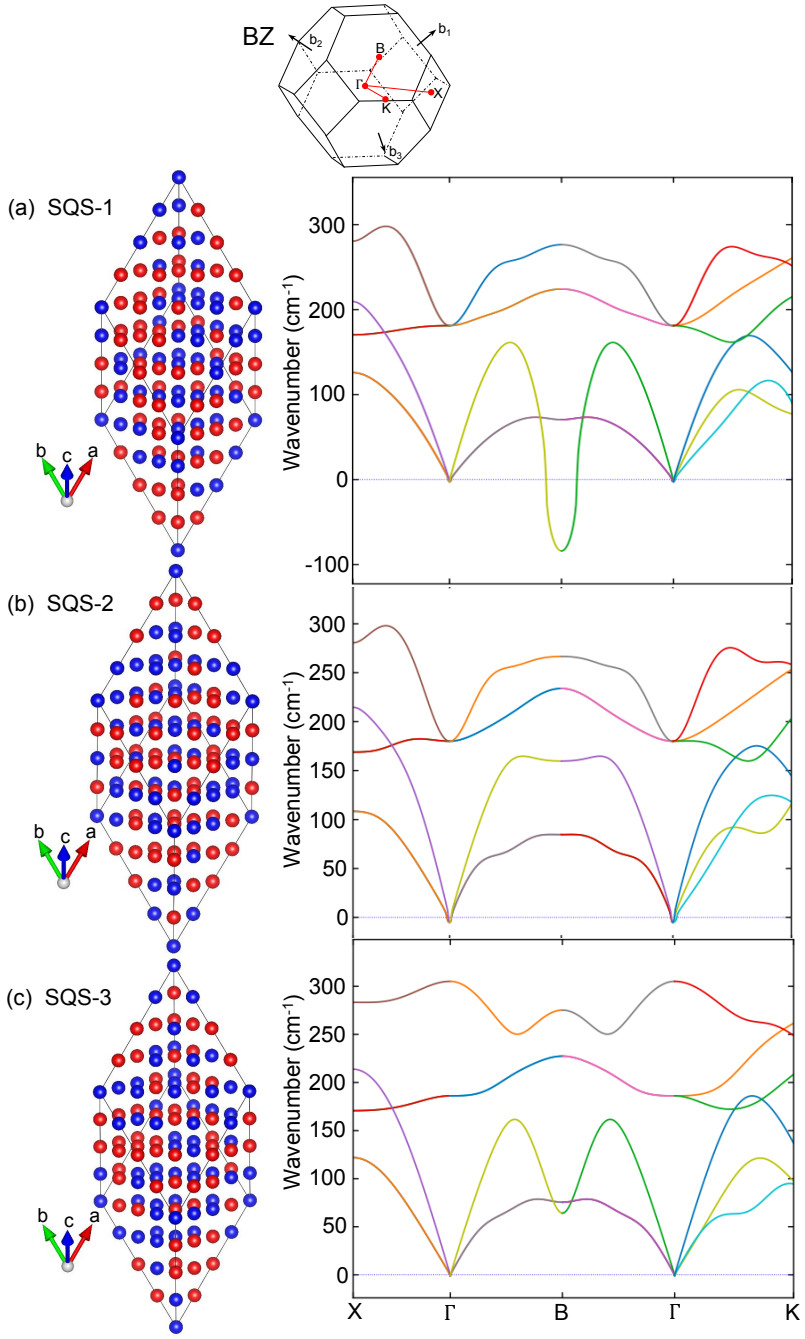

Figure 4.11: B1-SQS and phonon bands. BZ corresponds to the first BZ of the primitive cell of B1-MnS. Different colors are applied to distinguish the bands crossings [94]. This is done independently for each segment, i.e., specific colors in one segment do not correspond to the same bands in the other segment. The NAC correction was applied only to the soft-mode-free SQS-3.

without any negative modes, Fig. 4.11(c).

B4-MnS polymorph

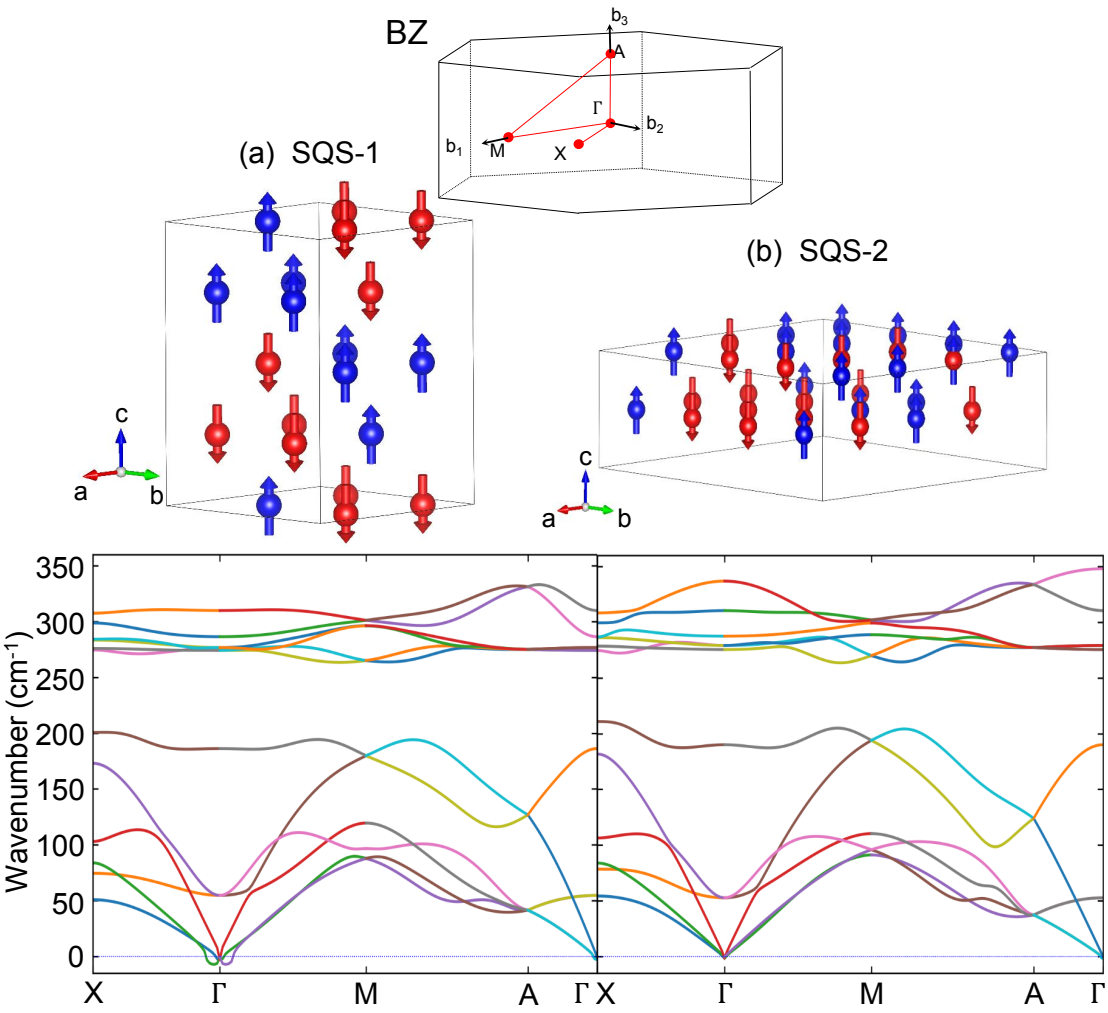

Figure 4.12: B4-SQS and phonon bands. BZ corresponds to the first BZ of the primitive cell of B4-MnS. Different sizes of SQS were tested. (a) 2×2×2 SQS supercell kept producing soft modes in the vicinity of Γ point for various values of k and m. (b) Using 4×4×1 SQS supercell, it was possible to obtain a soft-mode-free phonon band structure.

The search for a stable PM B4-MnS SQS configuration was slightly different from the B1-MnS case. Initially, a 2×2×2 SQS supercell was tested. For this size, only the inclusion of pairs and triplets allowed the generation of a "perfect" SQS,

Table 4.3. The figures of higher orders did not produce perfectly disordered structures. The investigation of the 2×2×2 SQS supercell with pairs and triplets revealed soft modes around the Γ-point, Fig. 4.12(a). As previously discussed, if figures of higher order for a given supercell size do not produce an SQS configuration without soft modes then a different size must be tested. Therefore, a 4×4×1 SQS supercell was generated. This size allowed us to increase the pair interaction distance and still obtain a "perfect" SQS. Such structure immediately created a soft-mode-free phonon band dispersion without having to include higher order figures, Fig. 4.12(b).

B31-MnS polymorph

All tested B31-MnS SQS configurations are shown in Fig. 4.13−4.14. Configurations SQS-1, SQS-2, and SQS-3 exhibited similar instabilities at the Γ point. Increasing the number of figures did not resolve the issue, leading only to slight changes in the magnitude of the soft modes. Normally, at this point, the size of the supercell should be increased in order to accommodate higher interaction distance m within figures of order k. However, this step would need a significant increase in the computational cost. Thus, a slightly different approach was tried in this case. From Fig. 4.14(a), it is noticed that the soft modes appear only in one acoustic band, whereas the other two appear stable. In other words, the vibrational instabilities are only observed in one direction, which is given by the eigenvector of the acoustic band that possesses those soft modes. Therefore, instead of constructing a new SQS configuration, the magnetic configuration could be altered only in the direction of instability. The direction of atomic oscillations is a linear combination of the three basis lattice vectors, therefore, the magnetic ordering along these vectors could be modified. In this case, a natural choice

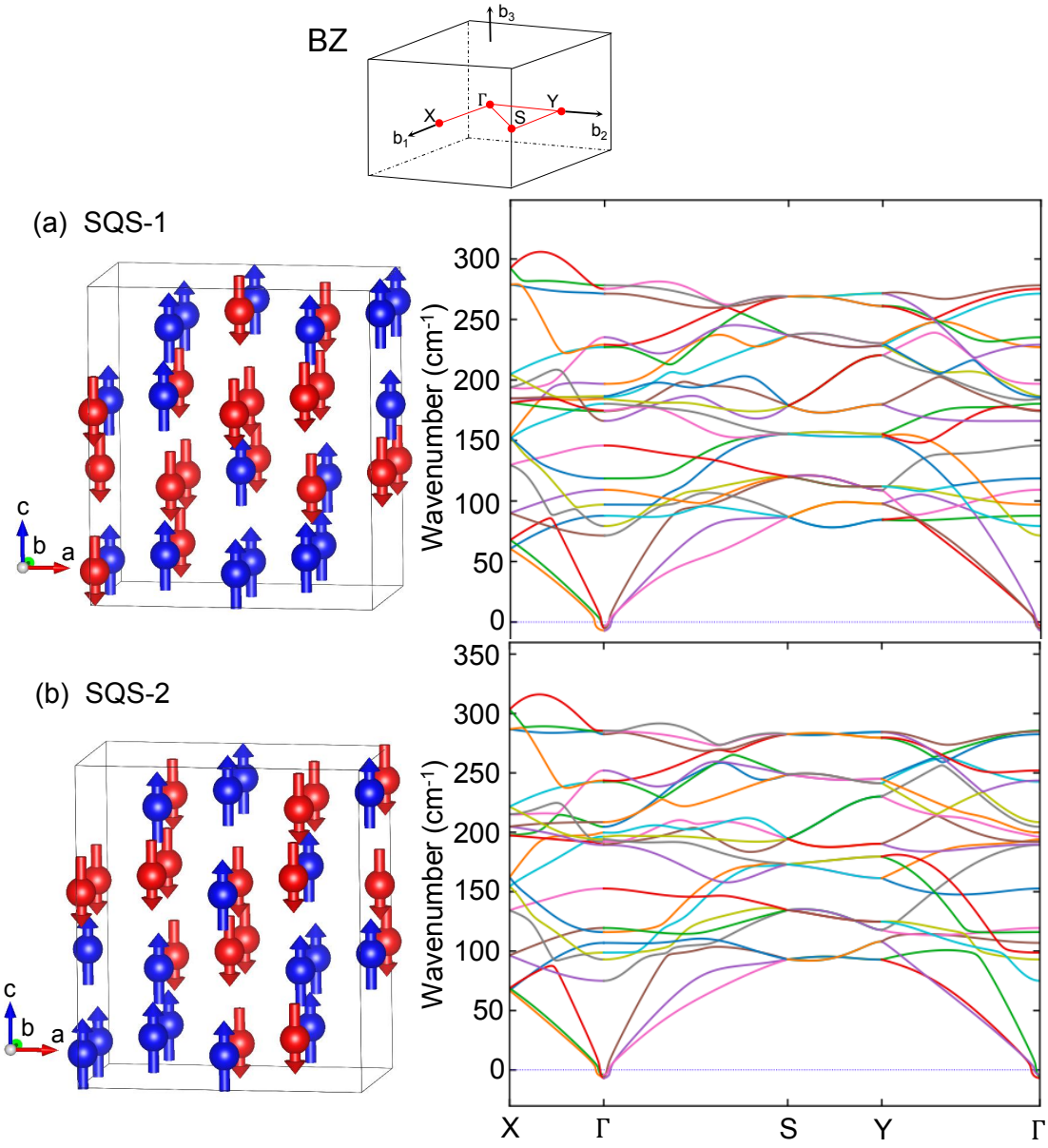

Figure 4.13: B31-SQS and phonon bands. BZ corresponds to the first BZ of the primitive cell of B31-MnS. Various values of k and m were not able to completely remove negative frequencies at the Γ point.

would be the **b**-direction since this lattice parameter is almost twice shorter than the other two, Fig. 4.10. A portion of the SQS-3 configuration is taken, namely the 2×1×2 part, and then repeated along the **b**-direction. The resulting structure and its phonon bands are shown in Fig. 4.14(b). As can be seen, such construc-

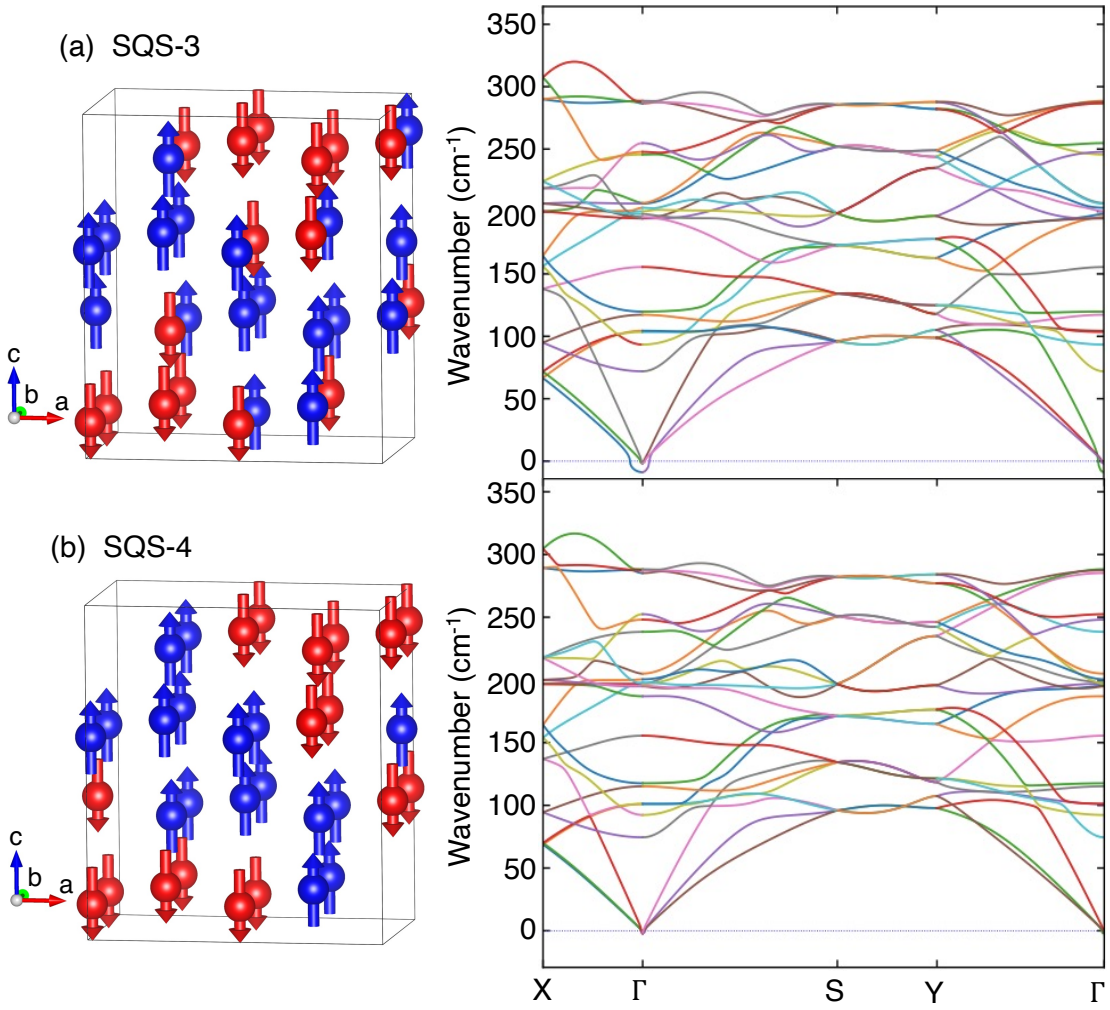

Figure 4.14: B31-SQS and phonon bands. (a) Noticing that the SQS-3 supercell possessed soft modes only in one acoustic band, the 2×1×2 part of SQS-3 was doubled in the **b**-direction. (b) A supercell thus obtained, SQS-4, produced phonon band structure without negative frequencies.

tion completely removed the soft modes that were present in one of the acoustic bands of an initial SQS-3 configuration. However, the SQS-4 configuration is not, strictly speaking, an SQS construct, since the correlation function does not match that of a perfectly random alloy.

4.3.2 Anharmonic effects, reflectivity

B1-MnS polymorph

The dielectric function used here was modeled based on a slightly modified form of the Lorentz model [238]:

$$\epsilon(\omega) = \epsilon_\infty + \frac{\epsilon_\infty(\omega_{LO}^2 - \omega_{TO}^2)}{\omega_{TO}^2 - \omega^2 - i\omega\Gamma(\omega)}, \tag{4.3}$$

where $\Gamma(\omega)$ is the imaginary part of the phonon self-energy. The main difference from Eq.(2.78) is that the oscillator strength is expressed directly in terms of the difference between the LO and TO modes. The third-order force constants were calculated using 4×4×4 supercells constructed from the FCC primitive cell. This supercell size resulted in the overall number of 442 displacement configurations, which corresponds to the phonon interaction distance of 10.44 Å. The local magnetic moments in the displaced configurations were distributed according to the stable SQS cell found in the previous section, i.e., SQS-3 in Fig. 4.11(c). The imaginary part of the self-energy was calculated on a 12×12×12 **q**-grid in reciprocal space. Since the main interest is to study the room/high temperature paramagnetic state of MnS, the isotope-disorder scattering effects were ignored as it was shown in the previous chapter that they are mostly visible only at low temperatures.

The calculated optical parameters are summarized in Table 4.4. As can be seen, there is a good agreement between the calculated and reported TO and LO modes. The imaginary part of the dielectric function together with the reflectivity is shown in Fig. 4.15, and the calculated optical parameters together with the experimental ones are summarized in Table 4.4. As can be seen from Fig. 4.15(a), the imaginary part of the dielectric function broadens as temperature increases. The

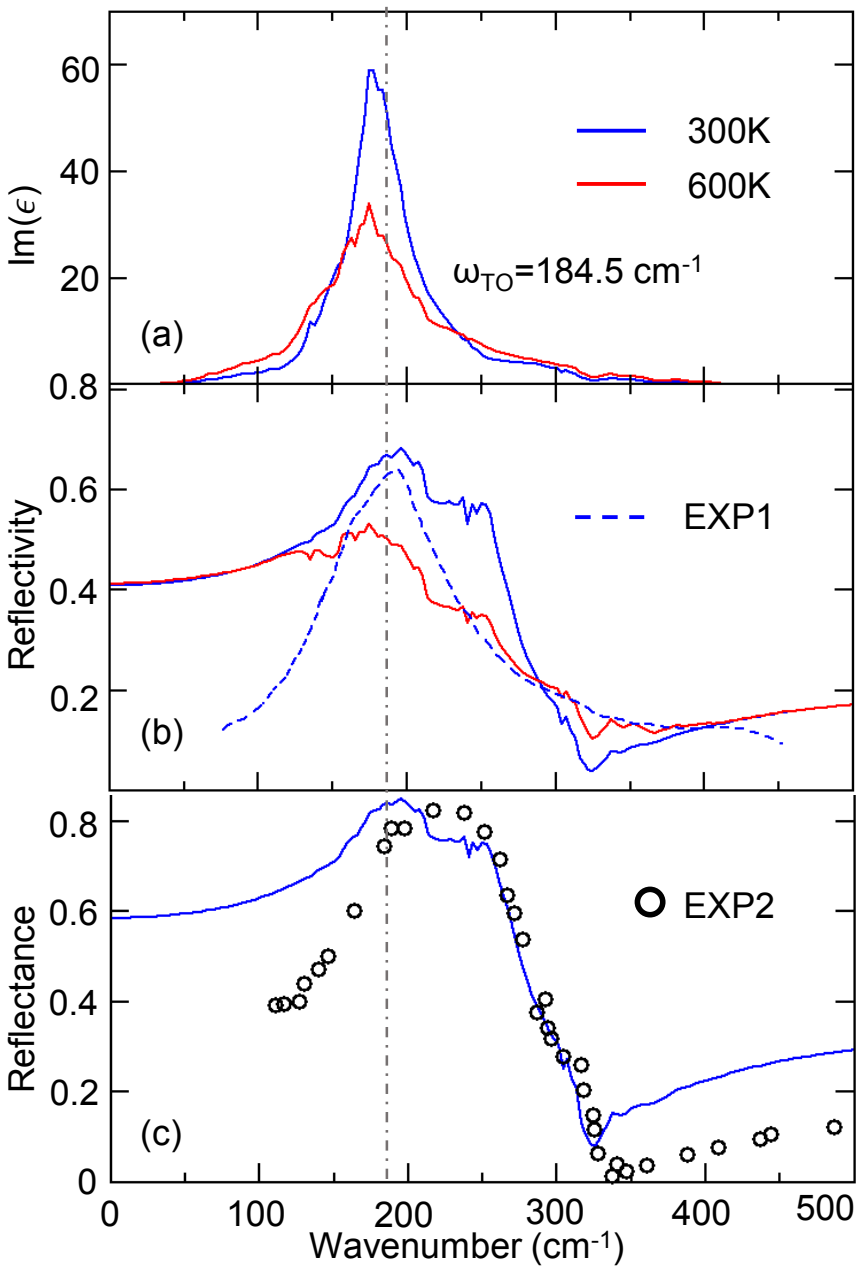

Figure 4.15: (a) Imaginary part of the predicted dielectric function for B1-MnS. (b) Computed reflectivity (solid lines) is compared to the experimental reflectivity of B1-MnS on a glass substrate. (c) Calculated reflectance of bulk B1-MnS is compared to measurements of pressed MnS powder.

same behavior was observed in CaS and MgS in Chapter 3. However, unlike in the case of CaS and MgS, the imaginary part of the dielectric function of the B1-MnS phase seems to deviate from the δ-peak behavior more strongly. In the

Table 4.4: Optical parameters of B1- and B4-MnS polymorphs. The calculated values are denoted by "DFT". "EXP1" and "EXP2" correspond to experimentally determined values.

System	Method	ϵ_∞	ω_{TO} (cm^{-1})	ω_{LO} (cm^{-1})	Ref.
B1-MnS	DFT	7.85	184.5	302.8	This work
	EXP1	–	185	330	[238]
	EXP2	6.80	185	320	[229]
B4-MnS	DFT	6.84	284.5	320.8	This work
	EXP1	–	286	324	[238]

case of both CaS and MgS, the $Im(\epsilon)$ displayed a rather sharp peak of magnitude at least two orders higher than the tail values, Fig. 3.2. This peak is preserved for the B1-MnS, however, it is spread over a wider range of wavenumbers. This broadening becomes slightly stronger as temperature increases. The predicted reflectivity is shown in Fig. 4.15(b), where it is also compared to available experimental measurements [238]. It can be seen that both calculated and experimental curves at 300 K reach their maximum at about the same wavenumber, which corresponds to the outer edge of the reststrahlen band. The main differences between the calculated and experimental trends originate from several sources. Firstly, the reflectivity obtained in the experiment of Ref. [238] is the result of B1-MnS grown on a glass substrate. Therefore, the reported reflectivity was fitted using a two-layer Lorentz model to treat the system as a sum of two oscillators: one corresponding to MnS (polycrystalline thin film) and the other corresponding to the glass substrate, i.e.:

$$\epsilon(\omega) = \epsilon_\infty + \frac{\epsilon_\infty(\omega_{LO}^2 - \omega_{TO}^2)}{\omega_{TO}^2 - \omega^2 - i\omega\Gamma(\omega)} + \frac{S_0}{\omega_0^2 - \omega^2 - i\omega\Gamma_0}, \tag{4.4}$$

where S_0, ω_0, and Γ_0 are the oscillator strength, resonant frequency, and damping constant of the glass substrate. These parameters were obtained from the reflectivity measurements of the pure substrate without MnS thin film [238]. Then, the

overall dielectric function $\epsilon(\omega)$ given by Eq. (4.4) was determined from reflectivity measurements of the MnS-substrate system. Thus, comparing the calculated reflectivity of bulk Pm B1-MnS to the one fitted from the MnS-substrate system is not entirely straightforward. The presence of the glass substrate could explain partially why the experimental reflectivity is lower in magnitude than the predicted one in the region from $\sim$90 cm^{-1} until 160 cm^{-1}. Secondly, the calculated reflectivity is higher than the experimental one inside the reststrahlen band. This behavior is similar to the case of CaS and MgS, and it could be probably attributed to the lack of additional damping effects, such as four-phonon interactions. The addition of four-phonon scattering processes might produce enough damping to be closer to the experimental reflectivity. These higher-order scatterings could also smooth the peaky structure observed in the calculated curve. Finally, the calculated reflectivity exhibits a characteristic dip around the wavenumber corresponding to the LO mode. Such dip is absent from the measured reflectivity of the MnS-substrate system [238]. However, it is present in the reflectance spectrum of pressed powder MnS samples [229]. The calculated reflectance is shown in Fig. 4.15(c) and is compared to the fitted one ("EXP2" [229]) from reflectivity measurements of pressed powder samples. As discussed in Chapter 3, measurements of pressed pellets can deviate significantly from single-crystal results. However, some optical parameters, such as the LO/TO splitting can still be expected to correlate closely. In general, there is a better agreement between the calculated and experimental reflectance of Ref. [229] than between the predicted and measured reflectivity of Ref. [238]. In the reflectance case, Fig. 4.15, the agreement between *ab initio* trend and the experimental one within the reststrahlen band ($\sim$184$-$320 cm^{-1}) is quite remarkable. The largest deviation appears in the low-wavenumber region (from 0 cm^{-1} until $\sim$184 cm^{-1}). This disagreement is typical for DFT predictions

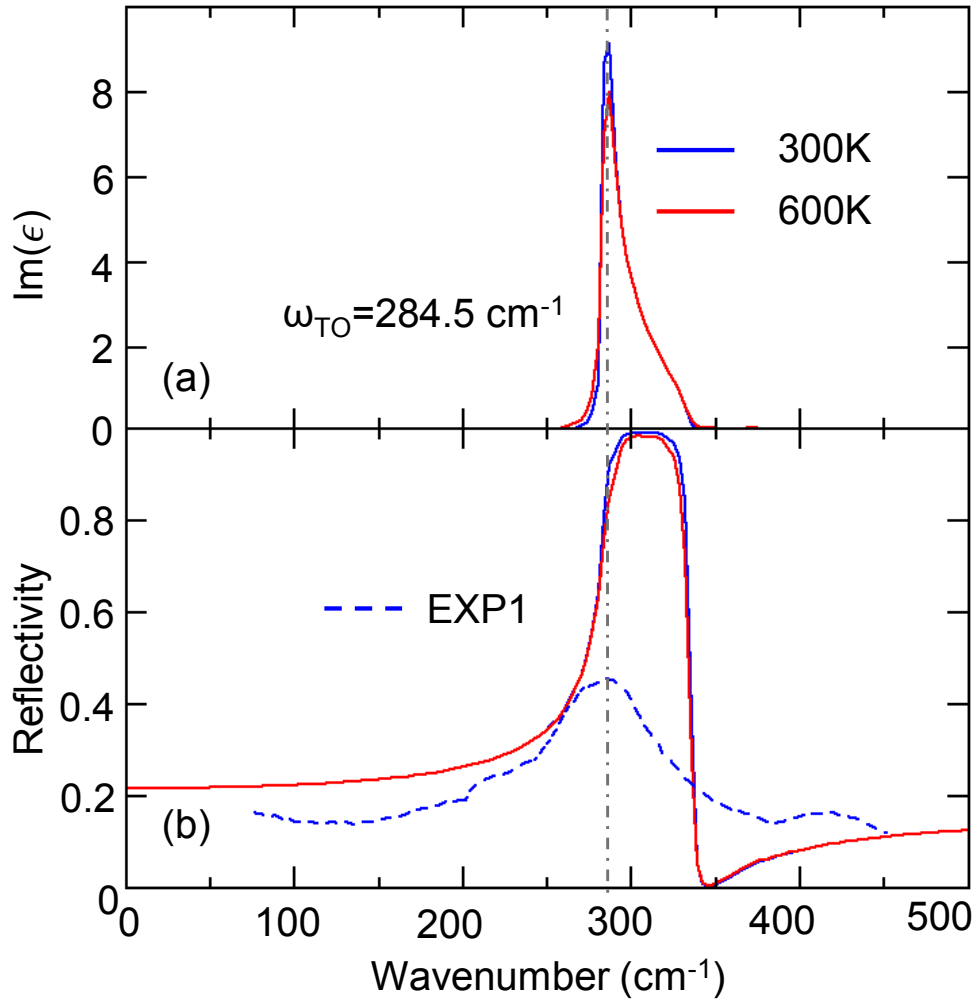

Figure 4.16: (a) B4-MnS imaginary part of the dielectric function. (b) Calculated reflectivity is compared to experimental values [238].

and is due to the overestimation of the high-frequency dielectric constant [193]. Lastly, the overestimation of the reflectance in the high-wavenumber tail could be due to the lack of four-phonon scattering processes.

B4-MnS polymorph

For this polymorph, the third-order force constants were calculated using 4×4×1 supercells of the B4 primitive cell. The local magnetic moments in the displaced configurations were distributed according to the stable SQS supercell found in the

previous section, SQS-2 in Fig. 4.12(b). This size resulted in the overall number of 1048 possible displacement configurations. Due to our computational resources coming to an end, it was not possible to calculate the full third-order IFC matrix. One possible way to reduce the number of necessary displaced configurations is to introduce a cutoff radius for the phonon-phonon interaction distance as was explained in Chapter 3. With a cutoff radius of 4 Å, 152 displacement configurations were obtained. The imaginary part of the self-energy was calculated on a 12×12×12 **q**-grid in the reciprocal space. The isotope-disorder scattering effects were ignored as in the case of the B1-MnS polymorph.

The calculated imaginary part of the dielectric function and reflectivity are shown in Fig. 4.16. It can be seen that the $Im(\epsilon)$ deviates only slightly from δ-peak, Fig. 4.16(a). This behavior is a direct consequence of not using the full third-order IFC matrix. Evidently, the amount of phonon-phonon scatterings provided by the chosen cutoff radius is not enough to produce significant damping. This response is further seen from the calculated reflectivity in Fig. 4.16(b), which is only slightly different from the case of an undamped oscillator, Fig. 2.4. Nevertheless, there is a rather close agreement in the low-wavenumber region, which was significantly overestimated in the case of CaS, MgS, and B1-MnS. Additionally, there is also a good agreement between the calculated and experimentally determined optical parameters, Table 4.4. This outcome suggests that the overall agreement between reflectivities could be improved by calculating additional IFC that reach beyond 4 Å, which are, apparently, the main source of damping for the B4-MnS polymorph.

4.4 Conclusions

In summary, static first-principles calculations to model the AFM and PM states of four MnS polymorphs were carried out. It was demonstrated that the combination of PBE+U with the construction of SQS supercells and localization of the Mn d-electrons through occupation matrix control methods allowed to achieve not only convergence and accuracy of structural optimizations but was vitally crucial to obtain finite energy band gaps and local magnetic moments in the PM phases. This result was particularly important in the case of the PM rock-salt B1-MnS polymorph, which experimentally has been observed to be an insulator, but was predicted to be metallic by multiple simulations. In this study, it was also shown that with this approach, it was possible to isolate energy changes as a function of pressure due purely to ionic and lattice parameters relaxation under hydrostatic compression. In this manner, the enthalpies of the PM MnS polymorphs were computed in order to explore their high-pressure landscape to detect structural transformations, and indeed, the cubic B1-MnS structure was determined to be the most stable at ambient pressure and up to approximately 21 GPa, pressure at which B1 undergoes a structural transformation to the orthorhombic B31-MnS phase. The overall trends in the electronic structure as well as phase transitions are expected to hold for different U values. The increase (decrease) of the U value will result in the increase (decrease) of the structural parameters and, therefore, in the change of magnitude of the transition pressure. The chosen value in this work was supported by the close agreement to experimental structural parameters. The predicted B1→B31 transformation, in the context of all modeling considerations made in this work, is rather meaningful as it closely resembles a structural phase transition observed from X-ray diffraction and high-pressure experiments performed on B1-MnS, in which the new but unidentified phase was reported at

about 26 GPa. Overall, the approach used in this work proved to be accurate in the modeling of manganese sulfide polymorphs and thus can be extended in the future to the investigation of other TM compounds.

Atomic vibrations of PM B1-, B4-, and B31-MnS within the harmonic approximation were also modeled. The main focus was on obtaining soft-mode-free configurations of local magnetic moments using the SQS technique. Slightly different strategies for the search of stable SQS configurations were employed for each polymorph. In the case of B1-MnS it was possible to find an SQS supercell without soft modes by progressively increasing the complexity of figures involved in the SQS generation. However, this approach was not enough to obtain a soft-mode-free B4-MnS structure. Here, it was necessary to test different SQS sizes to find stable configurations. Lastly, B31-MnS required an even more specific approach. After examining the specifics of soft modes in several SQS candidates, it was noticed that one structure contained soft modes only in one acoustic branch. Therefore, a part of this $2\times2\times2$ SQS supercell, specifically the $2\times1\times2$ part, was taken and repeated along the $\mathbf{b}-$direction. Such a strategy was successful in completely removing all soft modes previously present.

Finally, the optical properties of the B1- and B4-MnS polymorphs were investigated beyond the harmonic approximation. Due to its significance, the B1-MnS was studied thoroughly by calculating the full third-order IFC, which included 442 displacement configurations. The results showed an overall good agreement with available experimental data, especially in the values of the LO/TO splitting. Some of the deviations could be attributed to specifics in fitting procedures used in the corresponding experiments. Also, it is important to note that the experiments were conducted on polycrystalline thin films ("EXP1") and pressed powder samples ("EXP2"). The reflectivity and reflectance obtained from such experi-

ments differ, in general, from single-crystal experiments, which are much closer to the modeling technique used in this work. Nevertheless, it was found that the optical parameters can still be reliably obtained from this single-crystal-like simulation. The B4-MnS and B31-MnS polymorphs have lower symmetry than B1-MnS. Therefore, a significantly larger number of displacement configurations was required to construct the full IFC matrix for these systems. Due to the end of our allocated time, only the B4-MnS polymorph was modeled. This system was chosen because there is available experimental data, which allows us to directly estimate the accuracy of the method used in this work. Unfortunately, it was not possible to calculate the full IFC matrix, which required 1048 displacement configurations. A cutoff radius for phonon-phonon interaction was imposed to reduce the overall number to 152. Consequently, the calculated reflectivity deviated slightly from the idealized undamped case. This trend suggests that a significant amount of damping processes come from beyond the considered cutoff distance. Yet, the calculated optical parameters showed a good agreement with the experimental data. Hence, it is reasonable to expect that using the full IFC matrix could lead to a much better reconciliation between the calculated and experimental results for B4-MnS.

Chapter 5

$LaTiO_{3-\delta}/SrTiO_{3-\delta}$ heterostructures

In this chapter, the topic of oxygen deficiency of LAO/STO heterostructures is investigated. In particular, the goal is to examine whether or not there is an effect of vacancy clustering at the interface.

5.1 Computational details

Electronic structure

All calculations were performed using VASP [190, 200] and the projector-augmented plane wave basis [152]. The core electrons were kept frozen, and the valence configurations were $5p^6 5d^1 6s^2$ for La, $3s^2 3p^1$ for Al, $4s^2 4p^6 5s^2$ for Sr, $3p^6 3d^3 4s^1$ for Ti and $2s^2 2p^4$ for O, respectively. The exchange-correlation (XC) term in the effective Kohn–Sham potential was approximated according to the Perdew–Burke–Ernzerhof parameterization for solids (PBEsol) [216] of the generalized gradient approximation (GGA) [115]. A 3×3×4 $LaTiO_{3-\delta}/SrTiO_{3-\delta}$ supercell consisting of 180 atomic sites was used, Fig. 5.1. Pairs of oxygen vacancies were modeled by man-

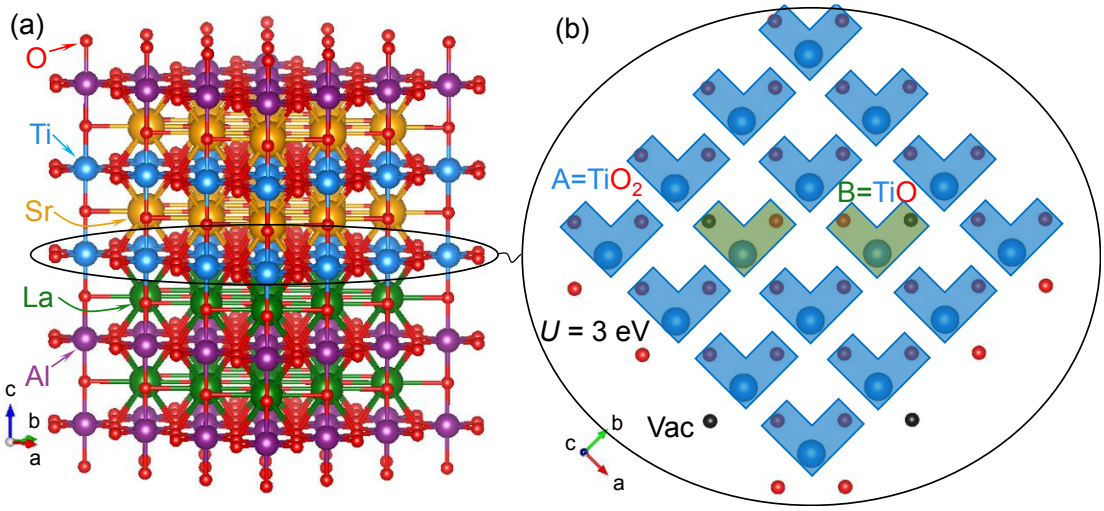

Figure 5.1: (a) 180-atomic site (178 atoms + 2 vacancies) $LaTiO_3/SrTiO_3$ supercell used in the calculations of this work. (b) The interface between LAO and STO layers. The "+U" correction is only applied to the Ti sites at the interface as it is effectively a $La_{0.5}Sr_{0.5}TiO_3$ system. The crystal structure is visualized using VESTA [20]

ually removing two oxygen atoms, corresponding to a vacancy concentration of 1.852% (δ =0.0556). Six different vacancy configurations were tested with various separations between O vacancies. The vacancy arrangements are shown in Fig. 5.2– 5.4. The k-space integration was done on a Γ-centered grid of uniformly distributed k-points with a spacing of $2\pi\times0.3$ Å^{-1}, resulting in a total of six k-points. The selected plane-wave kinetic energy cutoff was 500 eV and convergence of the structural optimizations was assumed when the total energy changes were less than 10^{-8} eV and the forces on each atom smaller than 10^{-3} eV/Å. The total energy for all configurations is shown in Fig. 5.6.

There are two points to which especial attention should be paid. First of all, the presence of La requires the additional care of the f-orbitals. These orbitals can sometimes end up close to or exactly at the Fermi level, although in reality are well above it. Therefore, the soft version of the La potential available in VASP was employed in this calculation. After checking the f-projected DOS for the

LAO/STO (without the vacancies), the f-states were found to be 3-4 eV above the Fermi level, which should be sufficient. Second of all, the interface couples to Sr and La atomic planes, making it effectively a $La_{0.5}Sr_{0.5}TiO_3$ system, Fig. 5.1. Bulk $LaTiO_3$ is a well-known Mott insulator [239]. Within the DFT framework, the electronic correlation effects can only be treated in a mean-field-like fashion through the DFT+U scheme. Therefore, the Hubbard "+U" correction of 3 eV was added to the Ti d-states at the interface. The next Ti layer did not require the "+U" term, since it effectively belongs to bulk $SrTiO_3$, which is a $d^{(0)}$ band-insulator.

Ionic relaxation

The full structural relaxation of the configurations considered turned out to be quite challenging. It was possible to fully relax (unit cell and ionic degrees of freedom) only two configurations, namely configurations "b" and "e", Fig. 5.2(b) and Fig. 5.4(e), respectively. Configuration "a", Fig. 5.2(a), which had the lowest energy before relaxation was impossible to be fully relaxed. The system seemed to be hitting a number of local minima and after trying distinct initialization paths and algorithms, it was still impossible to overcome the system being trapped in a local minimum. The rest of the configurations ("c", "d" and "e", Fig. 5.3(c), (d) and Fig. 5.4(e)) showed extremely slow convergence in interatomic forces. However, it seemed possible that they could eventually converge. Lastly, it was observed that without relaxing the structures, no finite local magnetic moments on any site were detected. After several iterations in the relaxation process, finite magnetic moments appeared and remained stable throughout the rest of the relaxation.

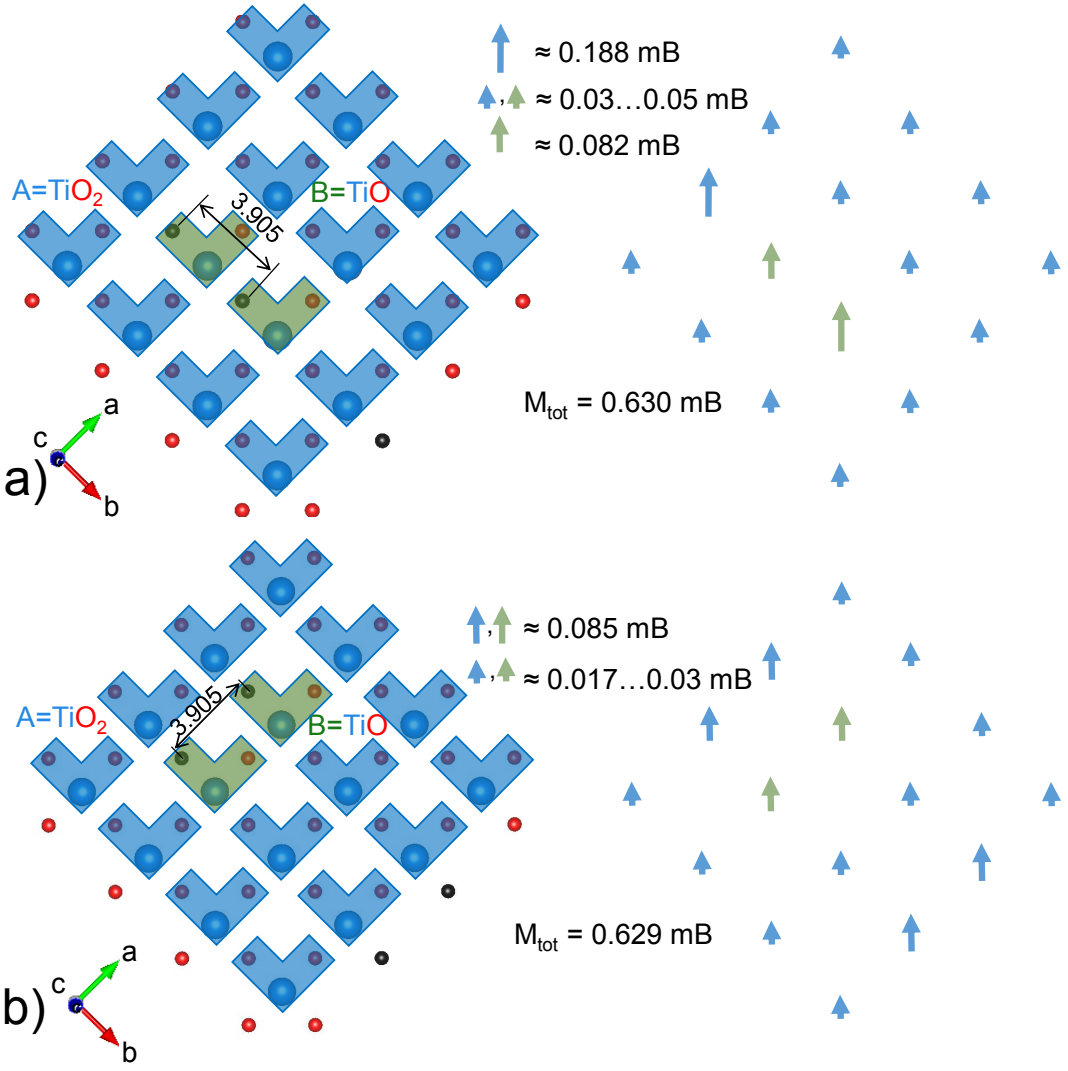

Figure 5.2: Configurations "a" and "b". The right-hand side shows the associated local magnetic moments. The moments appeared after several iterations of atomic relaxation and remained unchanged regardless of whether or not the structure was fully relaxed. It turned out impossible to fully relax configuration "a", configuration "b" was fully relaxed.

5.2 Orbital reconstruction

The orbital reconstruction that takes place at the LAO/STO interface can be qualitatively understood in terms of the surrounding crystal field change. In the bulk $SrTiO_{3-\delta}$ the orbital reconstruction due to the presence of the oxygen

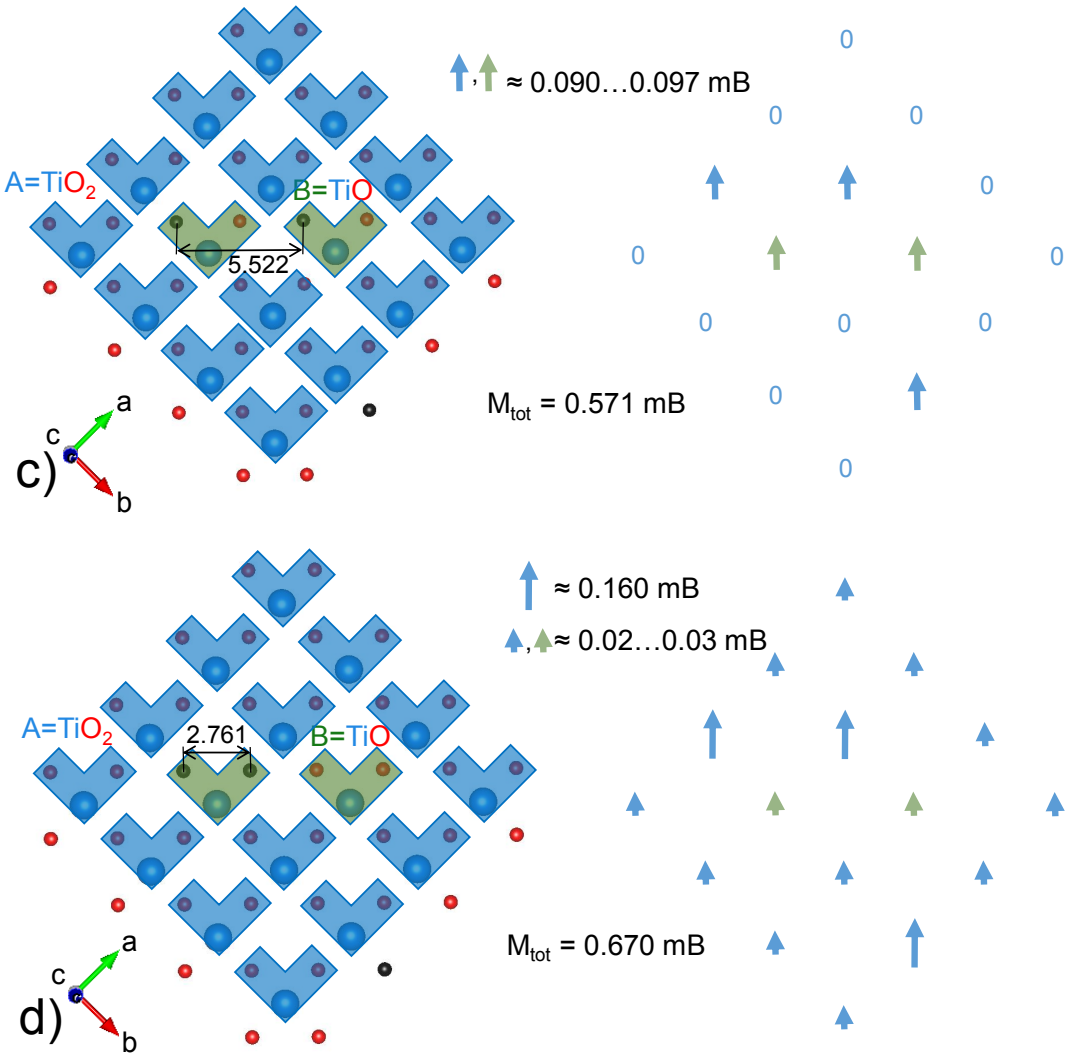

Figure 5.3: Configurations "c" and "d". Neither of these configurations was fully relaxed. However, the magnitude of the local magnetic moments remained unchanged after several iterations in the ionic relaxation.

vacancy has been explained with first- and second-order perturbation theory [88, 89]. Removing one oxygen atom lowers the corresponding Ti-ion symmetry from O_h to C_{4v}. In the case of a low vacancy concentration, this change in the crystal field symmetry can be treated as a perturbation. At first order, the C_{4v} crystal field lifts both the t_{2g} and e_g degeneracies. The lifting of the t_{2g} produces a singlet d_{xy}, which is lower in energy than the remaining doublet d_{xz} and d_{yz}.

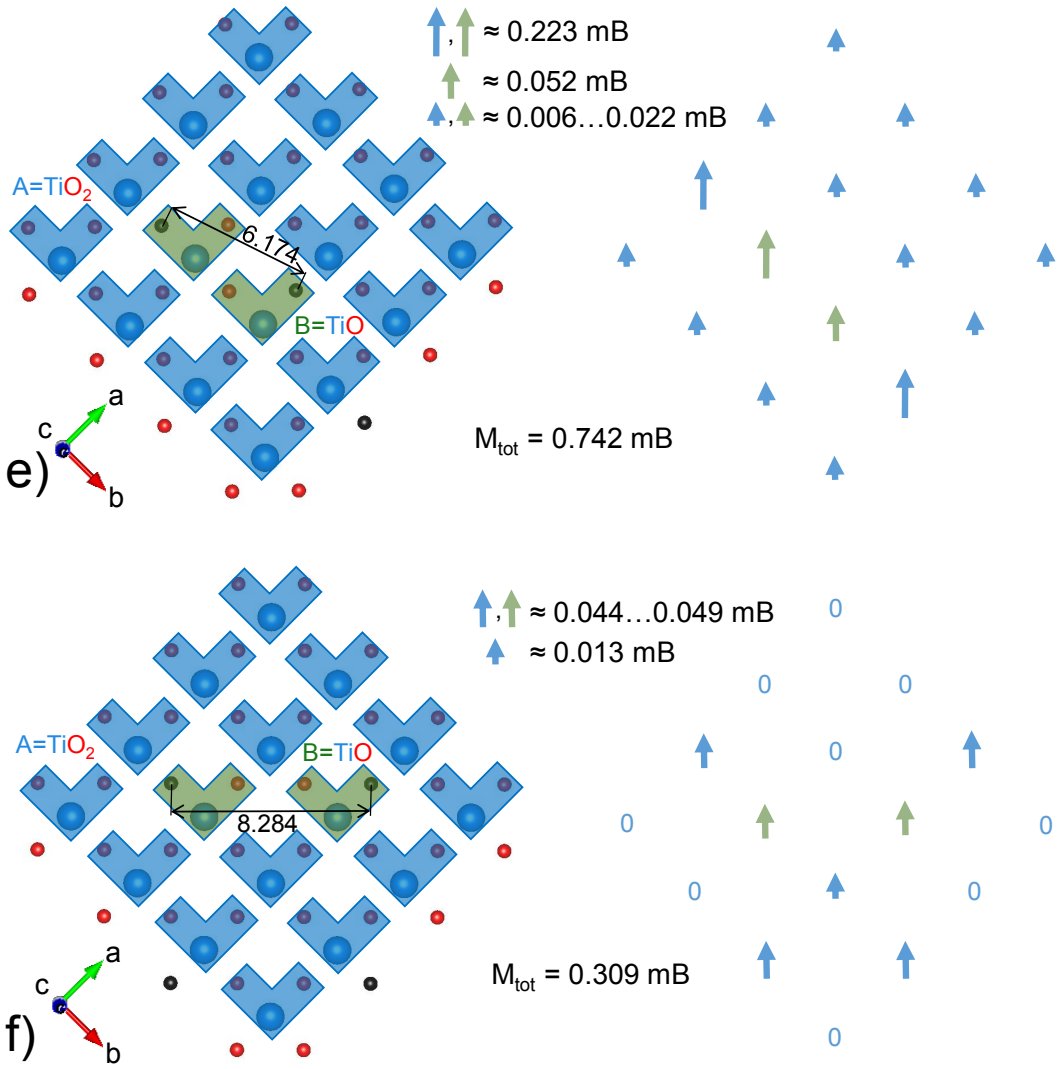

Figure 5.4: Configurations "e" and "f". Configuration "e" was fully relaxed, whereas configuration "f" was not. As in the previous cases, the magnitude of the moments saturated after several iterations and remained unchanged throughout the ionic relaxation for both configurations.

However, it has been argued that this effect might not be significant [88]. The second-order perturbation theory allows the coupling of Ti $3d$ with Ti $4s$ and $4p$ orbitals. In particular, this coupling pushes the d_{z^2} orbital below the t_{2g} orbitals. This mechanism does not, however, explain the lowering of the $d_{x^2-y^2}$ orbital. An alternative process postulated that the presence of the oxygen vacancy leads to the

Table 5.1: Total magnetization M_{tot} and distance between the vacancies Δ_{vv} for various configurations considered in this study

Configuration	a	b	c	d	e	f
M_{tot} (μB)	0.630	0.629	0.571	0.670	0.742	0.309
Δ_{vv} (Å)	3.905	3.905	5.522	2.761	6.174	8.284
Fully relaxed	No	Yes	No	No	Yes	No

lowering of the d_{y^2} state, which has contributions from both d_{z^2} and $d_{x^2-y^2}$ [240]. The local density of states (LDOS) projected at selected Ti sites are shown in Fig. 5.5. As can be seen, the Ti sites in the immediate vicinity of the oxygen vacancy show the in-gap states, which have d_{z^2} and $d_{x^2-y^2}$ character, Fig 5.5(a),(c) and (d). This observation is consistent with previous DFT studies [90, 91, 240]. Of particular interest is the Ti site neighboring both oxygen vacancies, Fig. 5.5(c). The in-gap states here have significantly higher populations than the other Ti sites. At the same time, the local magnetic moment of 0.082 μB associated with this site is more than twice lower than the value of 0.188 μB at the sites with only one vacancy next to them. This observation is indicative of the fact that the surrounding crystal field is stronger than the exchange interaction since the electrons prefer to occupy both spin channels of the low-lying in-gap states. The LDOS projected at the Ti site further away from the vacancies, Fig. 5.5(b) and (e), is in agreement with the model suggested in Ref. [88], i.e., these sites mostly preserve the O_h symmetry. However, due to the polar catastrophe at the interface, these orbitals receive a d-electron, which occupies t_{2g} manifold, particularly the d_{xy} orbital. The lowering of the d_{xy} orbital is due to the effect of oxygen vacancies, which in this case can be treated as a perturbation in the crystal field. A similar effect was also found in the defect-free LAO/STO interface [90]. The same crystal field argument applies in this case too, since at the defect-free LAO/STO interface Ti sites possess C_{4v} point symmetry. Therefore, the lifting of the t_{2g} degeneracy can be understood as the result of both oxygen vacancy and lower symmetry of

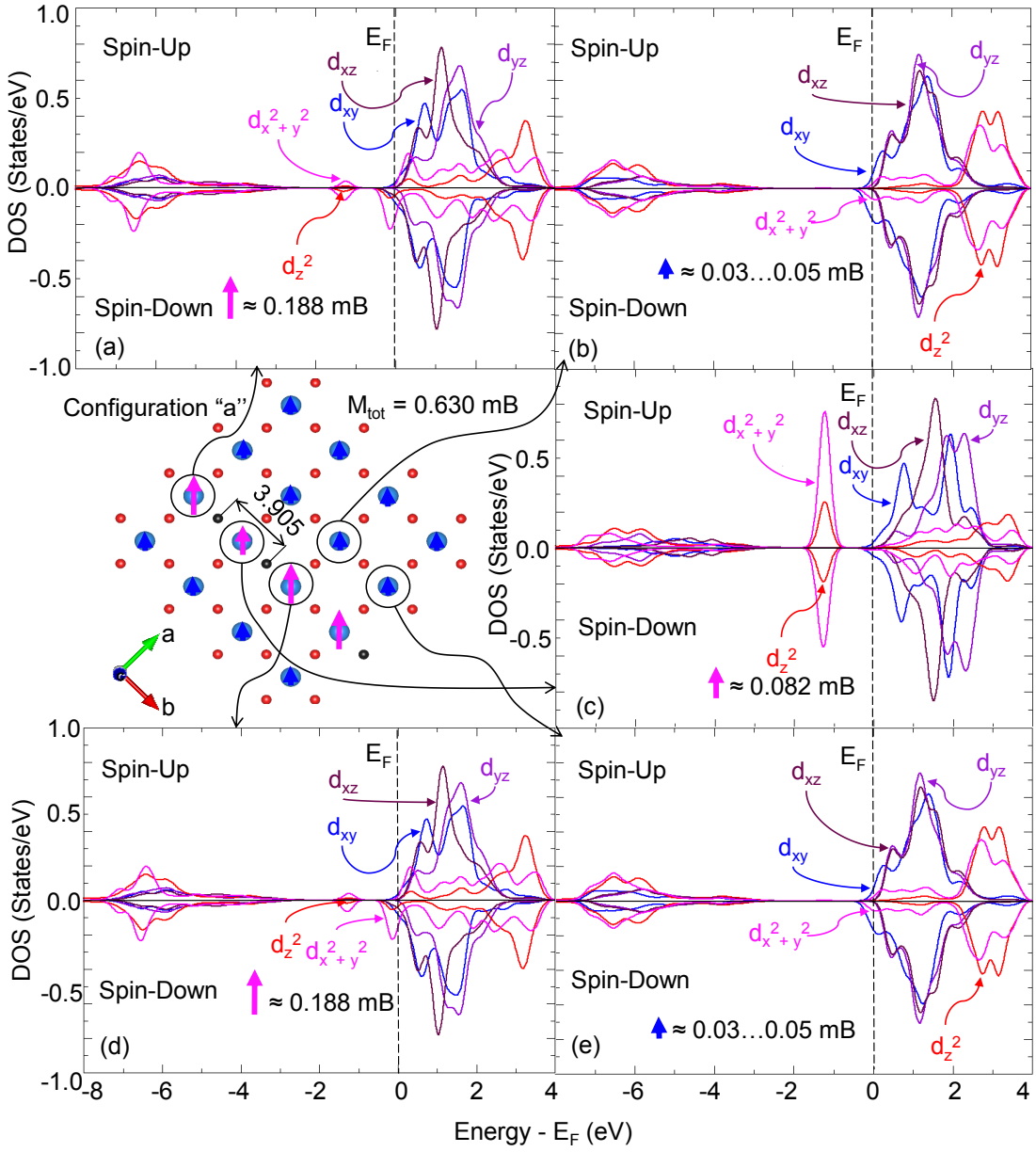

Figure 5.5: Ti-ion projected LDOS of configuration "a".There are two qualitatively distinct local magnetic moments. The ones (pink) that are centered at Ti sites in the immediate vicinity of the vacancies. These are made up of unequal filling of the e_g orbitals, mostly $d_{x^2-y^2}$. These moments are of the highest magnitude. The others (dark blue) are made up of d_{xy} orbitals. These are of 1-2 orders lower in magnitude.

the interface as compared to bulk STO.

5.3 Vacancy clustering

The total energy of all configurations considered is shown in Fig. 5.6. Clustering seems to be preferable in all cases except for configuration "d" which has the smallest separation between oxygen vacancies yet turns out to have the highest energy, although it is extremely close to configurations "c" and "e". It is also worth noting that configuration "a" has significantly lower energy than the other configurations. To better understand the difference between configurations "a" and "d", the LDOS of configuration "d" is plotted in Fig. 5.7. Comparing it to Fig. 5.5, the main difference is observed at the Ti site, which is positioned directly next to both vacancies. Unlike the linear clustering in configuration "a", which was characterized by highly populated in-gap states comprised of the $d_{x^2-y^2}$ and d_{z^2} orbitals, a much higher contribution from the d_{xy} orbitals can be seen in configuration "d". Following the mechanism previously explained, further lowering of the d_{xy} orbital signals the increase of the C_{4v} contribution to the surrounding crystal field. At the same time, this configuration seems to be less energetically favorable. Hence, it can be concluded that the system prefers to have the e_g states occupied.

The effect of vacancy clustering has also been found previously in bulk STO [241]. The effect of oxygen vacancy clustering has been confirmed experimentally in $SrTiO_{3-\delta}$ [242]. The authors found that the vacancies tend to arrange in a linear fashion analogous to configuration "a", Fig 5.2(a). Another DFT study found a similar tendency, although the authors concluded that the vacancy prefers to cluster vertically [243].

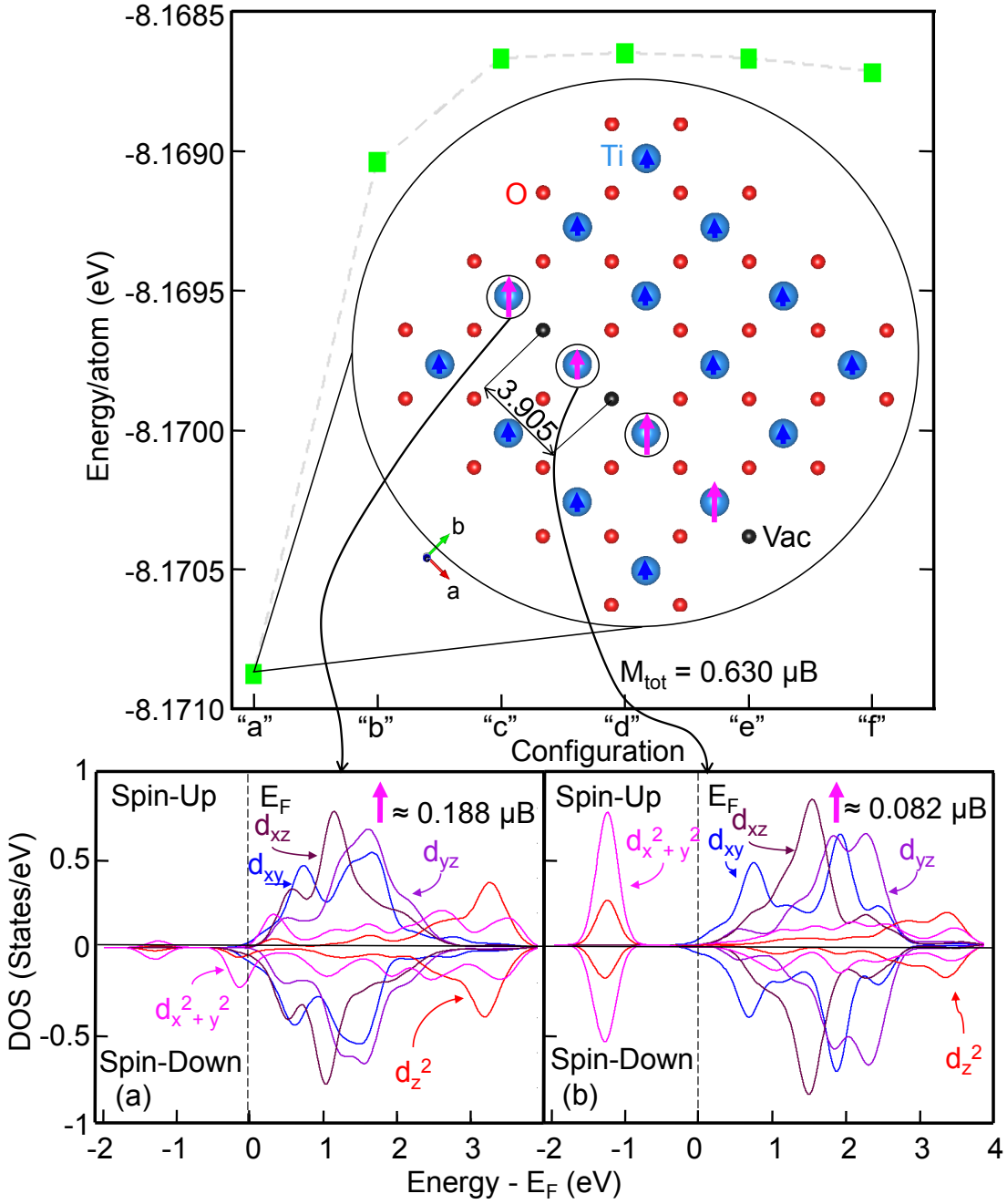

Figure 5.6: The total energy of LAO/STO with a pair of oxygen vacancies at the interface.

5.4 Conclusions

An oxygen-deficient heterostructure of $LaAlO_{3-\delta}/SrTiO_{3-\delta}$ was investigated using DFT with the main goal of clarifying the potential clustering of oxygen vacancies

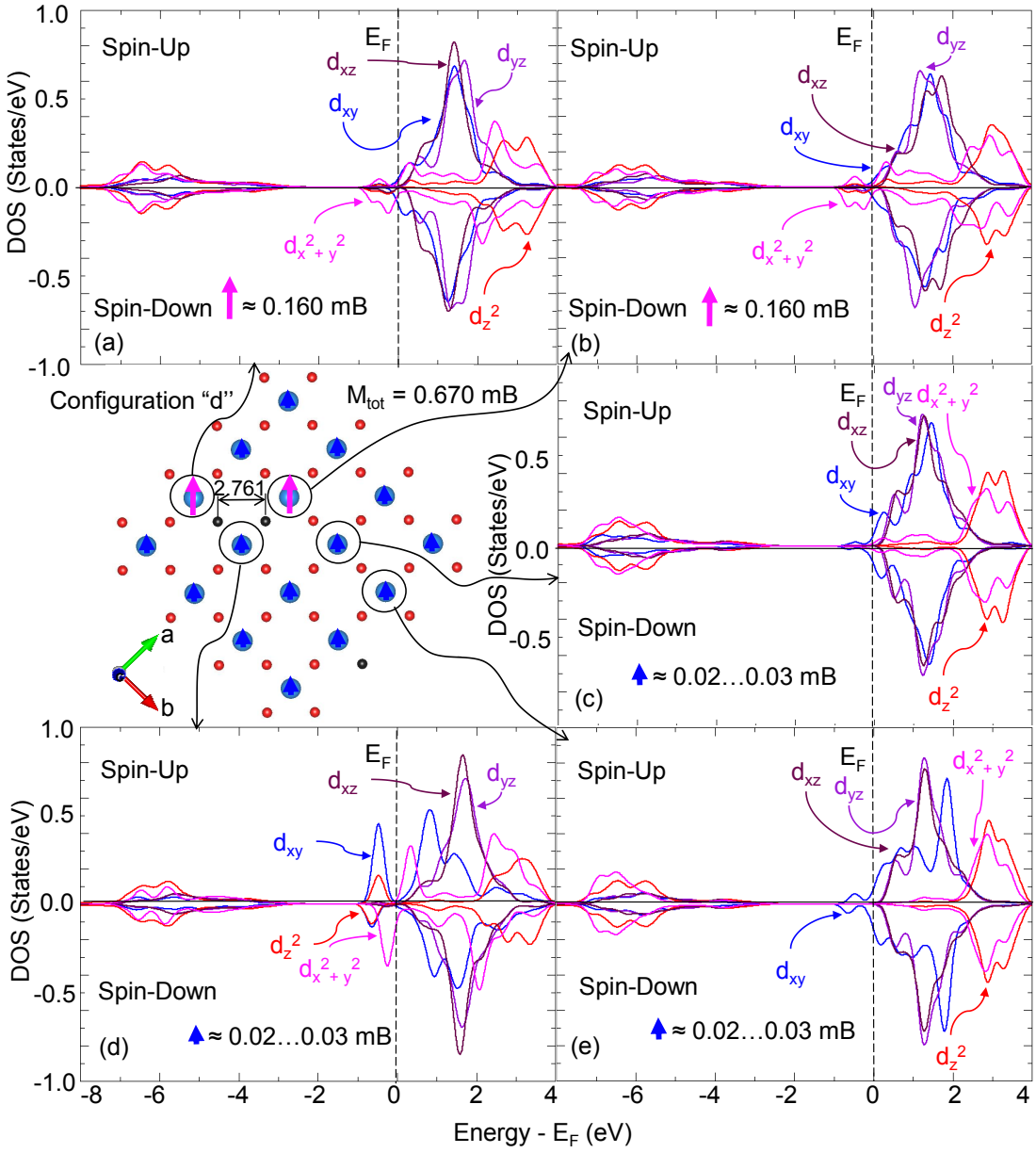

Figure 5.7: Ti-ion projected LDOS of configuration "d". The main difference with respect to configuration "a", Fig. 5.5, is the additional lowering of the d_{xy} states, which indicates a higher C_{4v} contribution to the crystal field.

at the interface. Oxygen vacancies were modeled by manually removing two oxygen atoms, and a total of six distinct configurations of a pair of vacancies at the interface were considered. Different mechanisms of orbital reconstruction for Ti ions can take place depending on the distance between the Ti ion and vacancies.

If a Ti ion is not situated directly next to an oxygen vacancy, then there is a lift of the t_{2g} symmetry, which results in the energy lowering of the d_{xy} orbital. This effect is also observed in stoichiometric LAO/STO heterostructures, where the redistribution of valence electrons takes place due to polar catastrophe phenomena. Specifically, the energy lowering of the d_{xy} orbital can be explained by considering the change in the surrounding crystal field as a perturbation. This energy lowering of the d_{xy} orbital is also present for Ti ions neighboring the oxygen vacancies, but in this case, the energy lowering of the e_g orbitals is more prominent. This study demonstrated that these states are responsible for finite local magnetic moments appearing at the oxygen-deficient LAO/STO interface. It was observed that out of the six configurations considered, the most energetically stable was the configuration with the oxygen vacancies arranged linearly at the opposite sites from the Ti ion.

Summary and outlook

First-principles investigations of structural, magnetic, and optical properties of CaS, MgS, and MnS, as well as the effect of vacancy clustering in $LaAlO_{3-\delta}/SrTiO_{3-\delta}$ were conducted using DFT [1, 2].

The optical properties of non-magnetic sulfides (CaS and MgS) were studied by a combination of DFT and FDM [94] techniques. To simulate the damping (anharmonicity), three-phonon scatterings together with the isotope-disorder scattering effect were included using perturbation theory [95, 96]. Overall, a satisfactory agreement with experimental and previous theoretical results was achieved. For CaS, the predicted LO/TO splitting of $\sim$113 cm^{-1} was a match to the experimental value of 113 cm^{-1} taken from single-crystal absorption data [203], but not to another measurement of 185 cm^{-1} also from absorption experiments [204]. The harsh difference in experimental values of the LO/TO splitting could be attributed to using two distinct methods to determine the LO/TO splitting from the respective raw data. On the other hand, a previous DFT study found a value of 70 cm^{-1} for the LO/TO splitting [205] in CaS, which is grossly underestimated in comparison to both LO/TO splitting reported measurements. The disparity between the DFT result in this study and the previously calculated one can be linked mainly to the fact that the Born effective charges and high-frequency dielectric constant were not fully found *ab initio* for the value of 70 cm^{-1}, but taken from other studies [219, 220]. The predicted reflectivity for CaS compared

well with the single-crystal absorption spectrum [203]. The main difference was the presence of a peaky structure in the high-wavenumber tail of the simulated reflectivity, which was absent in the experimental data [203]. A possible explanation for this discrepancy could be the lack of four-phonon scattering processes in the calculation of the self-energy (damping constant). In the case of MgS, the calculated LO/TO splitting of $\sim$152 cm^{-1} was in excellent agreement with another DFT value of 156 cm^{-1} [206]. Unlike in the case of CaS, for MgS both DFT results were obtained from fully calculating by first-principles all parameters necessary for the computation of phonon frequencies. The small difference in the predicted values could be explained by the particular choice of potentials and exchange-correlation functionals (PAW + PBEsol in this work and PP + LDA in Ref. [206]). Thus, both *ab initio* LO/TO splitting values were about 20% smaller than their experimental counterpart derived from absorption measurements of MgS thin films [204]. The underestimation of the DFT results could be associated to the method used to extract the experimental magnitudes of ω_{TO} and ω_{LO} [204]. The computed reflectivity for MgS also showed a similar peaky structure to that observed in CaS. Unfortunately, no reflectivity measurements were available for MgS to have a direct comparison with the DFT computations. Then, four MnS polymorphs were investigated with the main goal of calculating their optimal structures and reflectivity and reflectance spectra. PM states of each polymorph were modeled as disordered arrays of local magnetic moments using the SQS technique [92]. The analysis of the DOS showed that all polymorphs were insulating. This result was particularly important for the B1-MnS phase, as previous DFT simulations [230, 235] found it to be metallic, but experimentally has been observed to be insulating [229, 234]. Although, the predicted $E_g = 1.4$ eV for PM B1-MnS was fairly underestimated in comparison to the experimental values

of 2.7 eV [234] and 2.8 eV [229]. A scheme based on the idea of rehybridization of d and p orbitals was suggested to explain the shrinkage of the band gap in the transition from the AFM to the PM state. Additionally, the high-pressure landscape of the four MnS polymorphs was investigated by computing their enthalpies. The results showed a structural transition from the cubic B1-MnS phase to the orthorhombic B31-MnS polymorph at about 21 GPa. These findings shed a new light onto reported high-pressure transitions observed in DAC experiments [80–83]. Vibrational properties of MnS polymorphs were studied using a combination of DFT and FDM methods. First, using SQS constructions for each polymorph, a systematic study within the harmonic approximation was followed to obtain soft-mode-free SQS supercells. Slightly different strategies in the SQS generation were employed in each case. The reflectivity and reflectance were calculated for the B1- and B4-MnS polymorphs. In these cases, only three-phonon scattering processes were included in the calculation of the phonon self-energy. For the B1-MnS polymorph, an overall reasonable agreement with experimental results was achieved [229, 238]. The calculated LO/TO splitting of 118.3 cm^{-1} was slightly lower in comparison to experimentally determined values of 135 cm^{-1} (B1-MnS grown on a glass substrate) [238] and 145 cm^{-1} (B1-MnS powder pellets) [229]. Additionally, the calculated reflectivity and reflectance were in fairly good agreement with experimental spectra. In the case of the B4-MnS polymorph, a close match between the calculated and the experimental LO/TO splitting values of $\sim$36 cm^{-1} and 38 cm^{-1} [238], respectively, was achieved. However, the predicted reflectivity was about 60% larger within the reststrahlen band. The reason for this overestimation could be connected to the phonon-phonon interaction cutoff distance of 4 Å, which was used in the calculation of the self-energy. Increasing this radius could help reach a much better agreement with the experimental spec-

trum.

Lastly, the phenomenon of vacancy clustering in the $LaAlO_{3-\delta}/SrTiO_{3-\delta}$ heterostructure was investigated. Six different vacancy configurations with varying distance between two vacancies were analyzed. The most energetically stable vacancy configuration was found to be the one in which the vacancies were arranged linearly at the opposite sites from the Ti ion, this result was consistent with previous findings [243]. General trends of orbital reconstruction previously observed by other DFT studies [88–91, 240, 243] were also found in this work. In particular, two mechanisms of orbital reconstruction were recognized. The first one is characteristic of Ti ions located further away from vacancy sites, and it is realized by lifting the t_{2g} degeneracy and lowering the d_{xy} orbital. This effect can be described within the framework of perturbation theory [88, 89]. The second mechanism is realized at Ti ions that neighbor the vacancies directly. In this case, the e_g orbitals are lowered in energy.

The results obtained in this work can be further improved and serve as a basis for future developments. The simulated optical properties of CaS, MgS and B1-MnS could describe better experimental results by the inclusion of four-phonon scattering processes [95, 96]. A DFT study on MgO [193] showed that this inclusion resulted in a much better agreement between predicted and experimental reflectivities, reflectances, etc. Therefore, CaS, MgS and B1-MnS could also benefit from higher-order scattering processes. Also, it is possible that the four-phonon part of the self-energy (the "Loop" diagram) could smooth the simulated reflectivity in the high-wavenumber region. In the case of the B4-MnS polymorph, an obvious continuation would be to extend the phonon-phonon interaction cutoff radius to include larger number of displacement configurations. Considering the excellent agreement already obtained between the calculated LO/TO splitting

and the experimental value, it is reasonable to expect a much better match of the reflectivities too. Moreover, the data obtained for CaS, MgS and B1-MnS could be used in the calculation of transport properties, such as the thermal conductivity, which can be important in the study of Mercury formation. In this context, the four-phonon scatterings are highly relevant as it has been shown that their contribution to the reduction of the thermal conductivity could be of the same order as the three-phonon processes [244]. Also, the next natural consideration would be the study of alloys, e.g., $Ca_{1-x}Mg_xS$. In this case, the calculation of optical properties becomes more complex as, in principle, fully disordered supercells would be necessary to model $Ca_{1-x}Mg_xS$ alloy. These disordered alloys, however, could also be constructed using the SQS technique [92]. Their phonon bands can then be obtained from their supercells following an unfolding procedure [245], in which the spectral weights would be interpreted as part of the self-energy. Finally, further investigations on oxygen deficient LAO/STO heterostructures could be designed. The results of this and previous works [243] suggest the linear ordering of oxygen vacancies. It would be extremely interesting to see what effect completely disordered vacancies could have on the system. Such disordered state could also be constructed employing the SQS method.

Bibliography

[1] P. Hohenberg, W. Kohn, *Phys. Rev.* **1964**, *136*, B864.

[2] W. Kohn, L. J. Sham, *Phys. Rev.* **1965**, *140*, A1133.

[3] J. M. Rondinelli, E. Kioupakis, *Annu. Rev. Mater. Res.* **2015**, *45*, 491–518.

[4] D. J. Vaughan, J. R. Craig, *Mineral chemistry of metal sulfides*, Cambridge University Press, Cambridge, **1978**.

[5] R. R. Chianelli, M. Daage, M. J. Ledoux, *Adv. Catal.* **1994**, *40*, 177–232.

[6] Z.-H. Ge, L.-D. Zhao, D. Wu, X. Liu, B.-P. Zhang, J.-F. Li, J. He, *Mater. Today* **2016**, *19*, 227–239.

[7] D. G. Moon, S. Rehan, D. H. Yeon, S. M. Lee, S. J. Park, S. Ahn, Y. S. Cho, *Sol. Energy Mater. Sol. Cells* **2019**, *200*, 109963.

[8] X. Rui, H. Tan, Q. Yan, *Nanoscale* **2014**, *6*, 9889–9924.

[9] A. Ohtomo, H. Hwang, *Nature* **2004**, *427*, 423–426.

[10] H. Y. Hwang, Y. Iwasa, M. Kawasaki, B. Keimer, N. Nagaosa, Y. Tokura, *Nat. Mater.* **2012**, *11*, 103–113.

[11] A. Bhattacharya, S. J. May, *Annu. Rev. Mater. Res.* **2014**, *44*, 65–90.

[12] A. Brinkman, M. Huijben, M. Van Zalk, J. Huijben, U. Zeitler, J. Maan, W. G. van der Wiel, G. Rijnders, D. H. Blank, H. Hilgenkamp, *Nat. Mater.* **2007**, *6*, 493–496.

[13] S. Banerjee, O. Erten, M. Randeria, *Nat. Phys.* **2013**, *9*, 626–630.

[14] L. Li, C. Richter, J. Mannhart, R. Ashoori, *Nat. Phys.* **2011**, *7*, 762–766.

[15] J. W. Larimer, *Geochim. Cosmochim. Acta* **1968**, *32*, 965–982.

[16] K. Keil, K. Snetsinger, *Science* **1967**, *155*, 451–453.

[17] D. Lide, *CRC Handbook of Chemistry and Physics, Internet Version 2005*, CRC Press, **2005**.

[18] H. Feng, S. Wang, B. Wu, *J. Phys. Conf. Ser.* **2022**, *2148*, 012015.

[19] https://www.mindat.org/min-2970.html.

[20] K. Momma, F. Izumi, *J. Appl. Crystallogr.* **2008**, *41*, 653–658.

[21] N. Yamashita, S. Asano, *J. Phys. Soc. Jpn.* **1987**, *56*, 352–358.

[22] S. Tanaka, V. Shanker, M. Shiiki, H. Deguchi, H. Kobayashi, *Proceedings of the society for information display* **1985**, *26*, 255–258.

[23] T. A. O'Brien, P. D. Rack, P. H. Holloway, M. C. Zerner, *J. Lumin.* **1998**, *78*, 245–257.

[24] H. Kasano, K. Megumi, H. Yamamoto, *J. Electrochem. Soc.* **1984**, *131*, 1953.

[25] V. Shanker, S. Tanaka, M. Shiiki, H. Deguchi, H. Kobayashi, H. Sasakura, *Appl. Phys. Lett.* **1984**, *45*, 960–961.

[26] P. Smet, J. Van Gheluwe, D. Poelman, R. Van Meirhaeghe, *J. Lumin.* **2003**, *104*, 145–150.

[27] P. F. Smet, I. Moreels, Z. Hens, D. Poelman, *Materials* **2010**, *3*, 2834–2883.

[28] J. Versluys, D. Poelman, D. Wauters, R. Van Meirhaeghe, *J. Phys. Condens. Matter* **2001**, *13*, 5709.

[29] S. J. Yun, Y. S. Kim, S.-H. K. Park, *Appl. Phys. Lett.* **2001**, *78*, 721–723.

[30] B. Sun, G. Yi, D. Chen, Y. Zhou, J. Cheng, *J. Mater. Chem.* **2002**, *12*, 1194–1198.

[31] C. Wang, K. Tang, Q. Yang, C. An, B. Hai, G. Shen, Y. Qian, *Chem. Phys. Lett.* **2002**, *351*, 385–390.

[32] C. Wang, K. Tang, Q. Yang, Y. Qian, *J. Electrochem. Soc.* **2003**, *150*, G163.

[33] N. Sawada, Y. Chen, T. Isobe, *J. Alloys Compd.* **2006**, *408*, 824–827.

[34] P. Smet, D. Poelman, *J. Phys. D: Appl. Phys.* **2009**, *42*, 095306.

[35] S. Asano, N. Yamashita, *J. Phys. Soc. Jpn.* **1980**, *49*, 2231–2235.

[36] Y. Nakao, *J. Phys. Soc. Jpn.* **1980**, *48*, 534–541.

[37] S. Asano, N. Yamashita, *Phys. Lett. A* **1981**, *86*, 191–193.

[38] D. Aurbach, Z. Lu, A. Schechter, Y. Gofer, H. Gizbar, R. Turgeman, Y. Cohen, M. Moshkovich, E. Levi, *Nature* **2000**, *407*, 724–727.

[39] T. Gao, M. Noked, A. J. Pearse, E. Gillette, X. Fan, Y. Zhu, C. Luo, L. Suo, M. A. Schroeder, K. Xu, et al., *J. Am. Chem. Soc* **2015**, *137*, 12388–12393.

[40] P. Canepa, G. Sai Gautam, D. C. Hannah, R. Malik, M. Liu, K. G. Gallagher, K. A. Persson, G. Ceder, *Chem. Rev.* **2017**, *117*, 4287–4341.

[41] M. Mao, T. Gao, S. Hou, C. Wang, *Chem. Soc. Rev.* **2018**, *47*, 8804–8841.

[42] S.-H. Chung, A. Manthiram, *Adv. Mater.* **2019**, *31*, 1901125.

[43] Z. Zhao-Karger, X. Zhao, D. Wang, T. Diemant, R. J. Behm, M. Fichtner, *Adv. Energy Mater.* **2015**, *5*, 1401155.

[44] J. Zhang, Z. Chang, Z. Zhang, A. Du, S. Dong, Z. Li, G. Li, G. Cui, *ACS nano* **2021**, *15*, 15594–15624.

[45] O. Namur, B. Charlier, *Nat. Geosci.* **2017**, *10*, 9–13.

[46] B. Charlier, O. Namur, *Elements* **2019**, *15*, 9–14.

[47] C. Cartier, B. J. Wood, *Elements* **2019**, *15*, 39–45.

[48] L. R. Nittler, S. Z. Weider, *Elements* **2019**, *15*, 33–38.

[49] D. A. Rothery, M. Massironi, G. Alemanno, O. Barraud, S. Besse, N. Bott, R. Brunetto, E. Bunce, P. Byrne, F. Capaccioni, et al., *Space Sci. Rev.* **2020**, *216*, 1–46.

[50] H. Hiesinger, J. Helbert, G. Alemanno, K. Bauch, M. D'Amore, A. Maturilli, A. Morlok, M. Reitze, C. Stangarone, A. Stojic, et al., *Space Sci. Rev.* **2020**, *216*, 1–37.

[51] F. Vilas, D. L. Domingue, J. Helbert, M. D'Amore, A. Maturilli, R. L. Klima, K. R. Stockstill-Cahill, S. L. Murchie, N. R. Izenberg, D. T. Blewett, et al., *Geophys. Res. Lett.* **2016**, *43*, 1450–1456.

[52] H. Hiesinger, J. Helbert, M. C.-I. Team, *Planet. Space Sci.* **2010**, *58*, 144–165.

[53] B. Fender, A. Jacobson, F. Wedgwood, *J. Chem. Phys.* **1968**, *48*, 990–994.

[54] L. Corliss, N. Elliott, J. Hastings, *Phys. Rev.* **1956**, *104*, 924.

[55] D. F. Hewett, O. N. Rove, *Econ. Geol.* **1930**, *25*, 36–56.

[56] J. W. Anthony, R. A. Bideaux, K. W. Bladh, M. C. Nichols, Handbook of Mineralogy, **2012**.

[57] A. Lepland, R. L. Stevens, *Mar. Geol.* **1998**, *151*, 1–25.

[58] J. Čuda, T. Kohout, J. Filip, A. Tuček, Jiřıand Kosterov, J. Haloda, R. Skála, E. Santala, I. Medřík, R. Zbořil, *Am. Mineral.* **2013**, *98*, 1550–1556.

[59] https://www.mindat.org/min-89.html.

[60] https://www.mindat.org/min-7268.html.

[61] K. Keil, *J. Geophys. Res.* **1968**, *73*, 6945–6976.

[62] Y. Zhang, P. H. Benoit, D. W. Sears, *J. Geophys. Res. E* **1995**, *100*, 9417–9438.

[63] K. Keil, K. Fredriksson, *Geochim. Cosmochim. Acta* **1963**, *27*, 939–947.

[64] A. Fioretti, G. Molin, *Meteorit. Planet. Sci.* **1998**, *33*, A46.

[65] B. Mason, E. Jarosewich, *Geochim. Cosmochim. Acta* **1967**, *31*, 1097–1099.

[66] M. Kalinowski, *GFF* **1996**, *118*, 53–54.

[67] B. Skromme, Y. Zhang, D. J. Smith, S. Sivananthan, *Appl. Phys. Lett.* **1995**, *67*, 2690–2692.

[68] P. W. Anderson, *Phys. Rev.* **1950**, *79*, 350.

[69] P. W. Anderson, *Phys. Rev.* **1959**, *115*, 2.

[70] M. Lines, E. Jones, *Phys. Rev. B* **1965**, *139*, A1313.

[71] M. Lines, E. Jones, *Phys. Rev.* **1966**, *141*, 525.

[72] B. Morosin, *Phys. Rev. B* **1970**, *1*, 236.

[73] Y. Liu, Y. Qiao, W.-X. Zhang, Z. Li, X.-L. Hu, L.-X. Yuan, Y.-H. Huang, *J. Mater. Chem.* **2012**, *22*, 24026–24033.

[74] D. Chen, H. Quan, G.-S. Wang, L. Guo, *ChemPlusChem* **2013**, *78*, 843–851.

[75] S. M. Lee, J.-K. Lee, Y. C. Kang, *Chem.: Asian J.* **2014**, *9*, 590–595.

[76] X. Xu, S. Ji, M. Gu, J. Liu, *ACS Appl. Mater. Interfaces* **2015**, *7*, 20957–20964.

[77] N. F. Mahamad Yusoff, N. H. Idris, L. Noerochim, *Int. J. Energy Res* **2022**, *46*, 667–683.

[78] X. Li, J. Shen, N. Li, M. Ye, *J. Power Sources* **2015**, *282*, 194–201.

[79] Z. Zhang, H. Zhao, Z. Zeng, C. Gao, J. Wang, Q. Xia, *Electrochim. Acta* **2015**, *155*, 85–92.

[80] A. Kraft, B. Greuling, *Cryst. Res. Technol.* **1988**, *23*, 605–608.

[81] C. McCammon, *Phys. Chem. Miner.* **1991**, *17*, 636–641.

[82] J. S. Sweeney, D. L. Heinz, *Phys. Chem. Miner.* **1993**, *20*, 63–68.

[83] G. Xiao, X. Yang, X. Zhang, K. Wang, X. Huang, Z. Ding, Y. Ma, G. Zou, B. Zou, *J. Am. Chem. Soc.* **2015**, *137*, 10297–10303.

[84] P. Bouvier, J. Kreisel, *J. Phys. Condens. Matter* **2002**, *14*, 3981.

[85] A. Rusydi, S. Dhar, Y. Feng, J. Ding, H. Hilgenkamp, T. Venkatesan, *Natur. Comm.* **2011**, *2*.

[86] D. Dikin, M. Mehta, C. Bark, C. Folkman, C. Eom, V. Chandrasekhar, *Phys. Rev. Lett.* **2011**, *107*, 056802.

[87] J. A. Bert, B. Kalisky, C. Bell, M. Kim, Y. Hikita, H. Y. Hwang, K. A. Moler, *Natur. Physc.* **2011**, *7*, 767–771.

[88] C. Lin, C. Mitra, A. A. Demkov, *Phys. Rev. B* **2012**, *86*, 161102.

[89] C. Lin, A. A. Demkov, *Phys. Rev. Lett.* **2013**, *111*, 217601.

[90] F. Lechermann, L. Boehnke, D. Grieger, C. Piefke, *Phys. Rev. B* **2014**, *90*, 085125.

[91] M. Behrmann, F. Lechermann, *Phys. Rev. B* **2015**, *92*, 125148.

[92] A. Zunger, S.-H. Wei, L. G. Ferreira, J. E. Bernard, *Phys. Rev. Lett.* **1990**, *65*, 353.

[93] M. Cardona, Y. Y. Peter, *Fundamentals of semiconductors*, *Vol. 619*, Springer, **2005**.

[94] A. Togo, I. Tanaka, *Scr. Mater.* **2015**, *108*, 1–5.

[95] A. Maradudin, A. Fein, *Phys. Rev.* **1962**, *128*, 2589.

[96] R. Cowley, *Adv. Phys.* **1963**, *12*, 421–480.

[97] S.-i. Tamura, *Phys. Rev. B* **1983**, *27*, 858.

[98] R. O. Jones, O. Gunnarsson, *Rev. Mod. Phys.* **1989**, *61*, 689.

[99] J. Hafner, *J. Comp. Chem.* **2008**, *29*, 2044–2078.

[100] R. O. Jones, *Rev. Mod. Phys.* **2015**, *87*, 897.

[101] J. P. Brodholt, L. Voĉadlo, *MRS bulletin* **2006**, *31*, 675–680.

[102] M. Orio, D. A. Pantazis, F. Neese, *Photosynth. Res.* **2009**, *102*, 443–453.

[103] D. J. Cole, N. D. Hine, *J. Phys. Condens. Matter* **2016**, *28*, 393001.

[104] L. H. Thomas in Math. Proc. Camb. Philos. Soc. *Vol. 23*, Cambridge University Press, **1927**, pp. 542–548.

[105] E. Fermi, *Rend. Accad. Naz. Lincei* **1927**, *6*, 5.

[106] E. Fermi, *Z. Phys.* **1928**, *48*, 73–79.

[107] R. Martin, *Electronic Structure: Basic Theory and Practical Methods*, Cambridge University Press, **2004**.

[108] K. Capelle, *Braz. J. Phys.* **2006**, *36*, 1318–1343.

[109] https://www.tddft.org/programs/libxc/functionals/.

[110] L. Vitos, *Computational quantum mechanics for materials engineers: the EMTO method and applications*, Springer Science & Business Media, **2007**.

[111] J. P. Perdew, A. Zunger, *Phys. Rev. B* **1981**, *23*, 5048.

[112] D. M. Ceperley, B. J. Alder, *Phys. Rev. Lett.* **1980**, *45*, 566.

[113] J. P. Perdew, Y. Wang, *Phys. Rev. B* **1992**, *45*, 13244.

[114] J. Perdew, D. Langreth, V. Sahni, *Phys. Rev. Lett.* **1977**, *38*, 1030.

[115] D. C. Langreth, J. P. Perdew, *Phys. Rev. B* **1980**, *21*, 5469.

[116] J. P. Perdew, *Phys Rev. Lett.* **1985**, *55*, 1665.

[117] J. P. Perdew, W. Yue, *Phys. Rev. B* **1986**, *33*, 8800.

[118] J. P. Perdew, J. A. Chevary, S. H. Vosko, K. A. Jackson, M. R. Pederson, D. J. Singh, C. Fiolhais, *Phys. Rev. B* **1992**, *46*, 6671.

[119] J. P. Perdew, K. Burke, M. Ernzerhof, *Phys. Rev. Lett.* **1996**, *77*, 3865.

[120] Z. Wu, R. E. Cohen, *Phys. Rev. B* **2006**, *73*, 235116.

[121] J. Paier, R. Hirschl, M. Marsman, G. Kresse, *J. Chem. Phys.* **2005**, *122*, 234102.

[122] E. Moroni, G. Kresse, J. Hafner, J. Furthmüller, *Phys. Rev. B* **1997**, *56*, 15629.

[123] R. Hafner, D. Spisak, R. Lorenz, J. Hafner, *J. Phys. Condens. Matter* **2002**, *14*, 4297.

[124] J. P. Perdew, A. Ruzsinszky, G. I. Csonka, O. A. Vydrov, G. E. Scuseria, L. A. Constantin, X. Zhou, K. Burke, *Phys. Rev. Lett.* **2008**, *100*, 136406.

[125] T. Van Voorhis, G. E. Scuseria, *J. Chem. Phys.* **1998**, *109*, 400–410.

[126] J. P. Perdew, S. Kurth, A. Zupan, P. Blaha, *Phys. Rev. Lett.* **1999**, *82*, 2544.

[127] J. Tao, J. P. Perdew, V. N. Staroverov, G. E. Scuseria, *Phys. Rev. Lett.* **2003**, *91*, 146401.

[128] V. N. Staroverov, G. E. Scuseria, J. Tao, J. P. Perdew, *Phys. Rev. B* **2004**, *69*, 075102.

[129] J. Sun, A. Ruzsinszky, J. P. Perdew, *Phys. Rev. Lett.* **2015**, *115*, 036402.

[130] V. N. Staroverov, G. E. Scuseria, J. Tao, J. P. Perdew, *J. Chem. Phys.* **2003**, *119*, 12129–12137.

[131] J. Tao, J. Perdew, A. Ruzsinszky, G. Scuseria, G. Csonka, V. Staroverov, *Philos. Mag.* **2007**, *87*, 1071–1084.

[132] P. J. Stephens, F. J. Devlin, C. F. Chabalowski, M. J. Frisch, *J. Phys. Chem.* **1994**, *98*, 11623–11627.

[133] J. P. Perdew, M. Ernzerhof, K. Burke, *J. Chem. Phys.* **1996**, *105*, 9982–9985.

[134] N. F. Mott, *Proc. Phys. Soc. A* **1949**, *62*, 416.

[135] N. F. Mott, *Proc. R. Soc. Lond. A* **1982**, *382*, 1–24.

[136] V. I. Anisimov, J. Zaanen, O. K. Andersen, *Phys. Rev. B* **1991**, *44*, 943.

[137] H. Bruus, K. Flensberg, *Many-body quantum theory in condensed matter physics: an introduction*, OUP Oxford, **2004**.

[138] J. Hubbard, *Proc. Math. Phys. Eng. Sci.* **1963**, *276*, 238–257.

[139] M. Czyżyk, G. Sawatzky, *Phys. Rev. B* **1994**, *49*, 14211.

[140] V. I. Anisimov, I. Solovyev, M. Korotin, M. Czyżyk, G. Sawatzky, *Phys. Rev. B* **1993**, *48*, 16929.

[141] A. Liechtenstein, V. I. Anisimov, J. Zaanen, *Phys. Rev. B* **1995**, *52*, R5467.

[142] V. I. Anisimov, F. Aryasetiawan, A. Lichtenstein, *J. Phys. Condens. Matter* **1997**, *9*, 767.

[143] B. Himmetoglu, A. Floris, S. De Gironcoli, M. Cococcioni, *Int. J. Quantum Chem.* **2014**, *114*, 14–49.

[144] R. Judd, B., *Operator Tecnhiques in Atomic Spectroscopy*, McGraw-Hill, New York, **1963**.

[145] L. Vaugier, H. Jiang, S. Biermann, *Phys. Rev. B* **2012**, *86*, 165105.

[146] M. Cococcioni, S. De Gironcoli, *Phys. Rev. B* **2005**, *71*, 035105.

[147] S. L. Dudarev, G. A. Botton, S. Y. Savrasov, C. J. Humphreys, A. P. Sutton, *Phys. Rev. B* **1998**, *57*, 1505–1509.

[148] E. Bousquet, N. Spaldin, *Phys. Rev. B* **2010**, *82*, 220402.

[149] T. Jeong, W. Pickett, *J. Phys. Condens. Matter* **2006**, *18*, 6289.

[150] L. De'Medici, J. Mravlje, A. Georges, *Phys. Rev. Lett.* **2011**, *107*, 256401.

[151] K. Lejaeghere, G. Bihlmayer, T. Björkman, P. Blaha, S. Blügel, V. Blum, D. Caliste, I. E. Castelli, S. J. Clark, A. Dal Corso, et al., *Science* **2016**, *351*, aad3000.

[152] P. E. Blöchl, *Phys. Rev. B* **1994**, *50*, 17953.

[153] N. Ashcroft, N. Mermin, *Solid State Physics*, Holt, Rinehart and Winston, **1976**.

[154] K. Schwarz, P. Blaha, G. K. Madsen, *Comput. Phys. Commun.* **2002**, *147*, 71–76.

[155] J. C. Slater, *Phys. Rev.* **1937**, *51*, 846.

[156] O. K. Andersen, *Phys. Rev. B* **1975**, *12*, 3060.

[157] P. Blaha, K. Schwarz, P. Sorantin, S. Trickey, *Comput. Phys. Commun.* **1990**, *59*, 399–415.

[158] J. Singh, D., *Planewaves, Pseudopotential and the LAPW Method*, Kluwer Academic Publishers, Boston, Dordrecht, London, **1994**.

[159] O. Andersen, O. Jepsen, G. Krier, *Lectures on methods of electronic structure calculations* **1994**, 63–124.

[160] M. Springborg, O. K. Andersen, *J. Chem. Phys.* **1987**, *87*, 7125–7145.

[161] M. Methfessel, C. Rodriguez, O. Andersen, *Phys. Rev. B* **1989**, *40*, 2009.

[162] L. Vitos, J. Kollár, H. L. Skriver, *Phys. Rev. B* **1994**, *49*, 16694.

[163] L. Vitos, J. Kollár, H. L. Skriver, *Phys. Rev. B* **1997**, *55*, 13521.

[164] M. L. Cohen, V. Heine, *Solid State Physics*, Academic, New York, **1970**.

[165] R. Car, *Quantum. Struct. Act. Rel.* **2002**, *21*, 97–104.

[166] D. Hamann, M. Schlüter, C. Chiang, *Phys. Rev. Lett.* **1979**, *43*, 1494.

[167] G. B. Bachelet, D. R. Hamann, M. Schlüter, *Phys. Rev. B* **1982**, *26*, 4199.

[168] D. Vanderbilt, *Phys. Rev. B* **1985**, *32*, 8412.

[169] D. Vanderbilt, *Phys. Rev. B* **1990**, *41*, 7892.

[170] S. J. Clark, M. D. Segall, C. J. Pickard, P. J. Hasnip, M. I. Probert, K. Refson, M. C. Payne, *Z. Kristallogr. Cryst. Mater.* **2005**, *220*, 567–570.

[171] R. Car, M. Parrinello, *Phys. Rev. Lett.* **1985**, *55*, 2471.

[172] G. Kresse, D. Joubert, *Phys. Rev. B* **1999**, *59*, 1758.

[173] A. M. Rappe, K. M. Rabe, E. Kaxiras, J. Joannopoulos, *Phys. Rev. B* **1990**, *41*, 1227.

[174] O. Bengone, M. Alouani, P. Blöchl, J. Hugel, *Phys. Rev. B* **2000**, *62*, 16392.

[175] A. Rohrbach, J. Hafner, G. Kresse, *J. Phys. Condens. Matter* **2003**, *15*, 979.

[176] J. P. Allen, G. W. Watson, *Phys. Chem. Chem. Phys.* **2014**, *16*, 21016–21031.

[177] F. Yonezawa, K. Morigaki, *Prog. Theor. Phys. Suppl.* **1973**, *53*, 1–76.

[178] K. Hass, L. Davis, A. Zunger, *Phys. Rev. B* **1990**, *42*, 3757.

[179] A. Van de Walle, P. Tiwary, M. De Jong, D. Olmsted, M. Asta, A. Dick, D. Shin, Y. Wang, L.-Q. Chen, Z.-K. Liu, *Calphad* **2013**, *42*, 13–18.

[180] J. M. Sanchez, F. Ducastelle, D. Gratias, *Phys. A: Stat. Mech.* **1984**, *128*, 334–350.

[181] S.-H. Wei, L. Ferreira, J. E. Bernard, A. Zunger, *Phys. Rev. B* **1990**, *42*, 9622.

[182] J. Von Pezold, A. Dick, M. Friák, J. Neugebauer, *Phys. Rev. B* **2010**, *81*, 094203.

[183] D. Shin, A. Van De Walle, Y. Wang, Z.-K. Liu, *Phys. Rev. B* **2007**, *76*, 144204.

[184] A. Dick, T. Hickel, J. Neugebauer, *Steel Res. Int.* **2009**, *80*, 603–608.

[185] F. Körmann, A. Dick, B. Grabowski, T. Hickel, J. Neugebauer, *Phys. Rev. B* **2012**, *85*, 125104.

[186] L. Zhou, F. Körmann, D. Holec, M. Bartosik, B. Grabowski, J. Neugebauer, P. H. Mayrhofer, *Phys. Rev. B* **2014**, *90*, 184102.

[187] G. Trimarchi, Z. Wang, A. Zunger, *Phys. Rev. B* **2018**, *97*, 035107.

[188] J. Varignon, M. Bibes, A. Zunger, *Nat. Commun.* **2019**, *10*, 1–11.

[189] S. Baroni, S. De Gironcoli, A. Dal Corso, P. Giannozzi, *Rev. Mod. Phys.* **2001**, *73*, 515.

[190] G. Kresse, J. Furthmüller, *Phys. Rev. B* **1996**, *54*, 11169.

[191] K. Parlinski, Z. Li, Y. Kawazoe, *Phys. Rev. Lett.* **1997**, *78*, 4063.

[192] F. Gervais, *Mater. Sci. Eng. R Rep.* **2002**, *39*, 29–92.

[193] G. Fugallo, B. Rousseau, M. Lazzeri, *Phys. Rev. B* **2018**, *98*, 184307.

[194] A. Togo, L. Chaput, I. Tanaka, *Phys. Rev. B* **2015**, *91*, 094306.

[195] S. L. Adler, *Phys. Rev.* **1962**, *126*, 413.

[196] N. Wiser, *Phys. Rev.* **1963**, *129*, 62.

[197] S. Baroni, R. Resta, *Phys. Rev. B* **1986**, *33*, 7017.

[198] P. Nozieres, D. Pines, *Phys. Rev.* **1958**, *111*, 442.

[199] P. Van Camp, V. Van Doren, J. Devreese, *Phys. Rev. B* **1981**, *24*, 1096.

[200] G. Kresse, J. Furthmüller, *Comput. Mater. Sci.* **1996**, *6*, 15–50.

[201] A. Van De Walle, M. Asta, G. Ceder, *CALPHAD* **2002**, *26*, 539–553.

[202] A. Chmeruk, M. Núñez-Valdez, *Appl. Phys. A* **2023**, *129*, 477.

[203] Y. Kaneko, K. Morimoto, T. Koda, *J. Phys. Soc. Jpn.* **1982**, *51*, 2247–2254.

[204] A. Hofmeister, E. Keppel, A. Speck, *Mon. Not. R. Astron. Soc.* **2003**, *345*, 16–38.

[205] M. Bayrakci, K. Colakoglu, E. Deligoz, Y. O. Ciftci, *High Press. Res.* **2009**, *29*, 187–203.

[206] S. Duman, S. Bağcı, H. M. Tütüncü, G. Srivastava, *Phys. Rev. B* **2006**, *73*, 205201.

[207] E. Calandrini, L. Paulatto, D. Antonangeli, F. He, R. P. Lobo, F. Capitani, J.-B. Brubach, P. Roy, L. Vincent, P. Giura, *Phys. Rev. B* **2021**, *103*, 054302.

[208] A. R. Oganov, P. I. Dorogokupets, *Phys. Rev. B* **2003**, *67*, 224110.

[209] O. Hellman, I. Abrikosov, S. Simak, *Phys. Rev. B* **2011**, *84*, 180301.

[210] J. Klarbring, O. Hellman, I. A. Abrikosov, S. I. Simak, *Phys. Rev. Lett.* **2020**, *125*, 045701.

[211] L. Paulatto, F. Mauri, M. Lazzeri, *Phys. Rev. B* **2013**, *87*, 214303.

[212] G. Kresse, J. Furthmüller, J. Hafner, *EPL* **1995**, *32*, 729.

[213] T. Feng, X. Ruan, *Phys. Rev. B* **2016**, *93*, 045202.

[214] K. Esfarjani, H. T. Stokes, *Phys. Rev. B* **2008**, *77*, 144112.

[215] X. Gonze, C. Lee, *Phys. Rev. B* **1997**, *55*, 10355.

[216] G. I. Csonka, J. P. Perdew, A. Ruzsinszky, P. H. T. Philipsen, S. Lebègue, J. Paier, O. A. Vydrov, J. G. Ángyán, *Phys. Rev. B* **2009**, *79*, 155107.

[217] A. Chmeruk, M. Núñez-Valdez, *J. Appl. Phys.* **2022**, *131*, 115904.

[218] S. M. Peiris, A. J. Campbell, D. L. Heinz, *J. Phys. Chem. Sol.* **1994**, *55*, 413–419.

[219] G. K. Straub, W. A. Harrison, *Phys. Rev. B* **1989**, *39*, 10325.

[220] I. Boswarva, *Phys. Rev. B* **1970**, *1*, 1698.

[221] R. V. Gaines, H. C. Skinner, E. Foord, B. Mason, A. Rosenzweig, *Dana's New Mineralogy, Vol. 315*, John Wiley and Sons, New York, **1997**.

[222] B. Szigeti, *J. Chem. Soc. Faraday Trans.* **1949**, *45*, 155–166.

[223] P. Sony, A. Shukla, *Phys. Rev. B* **2008**, *77*, 075130.

[224] J. M. Soler, E. Artacho, J. D. Gale, A. García, J. Junquera, P. Ordejón, D. Sánchez-Portal, *J. Phys. Condens. Matter* **2002**, *14*, 2745.

[225] P. Giannozzi, S. Baroni, N. Bonini, M. Calandra, R. Car, C. Cavazzoni, D. Ceresoli, G. L. Chiarotti, M. Cococcioni, I. Dabo, et al., *J. Phys. Condens. Matter* **2009**, *21*, 395502.

[226] I. Varatharajan, A. Maturilli, J. Helbert, G. Alemanno, H. Hiesinger, *Earth Planet. Sci. Lett.* **2019**, *520*, 127–140.

[227] T. J. Johnson, E. Diaz, K. D. Hughey, T. L. Myers, T. A. Blake, A. C. Dohnalkova, S. D. Burton, *Appl. Spectrosc.* **2020**, *74*, 851–867.

[228] L. Long, M. Querry, R. Bell, R. Alexander, *Infrared Phys. Technol.* **1993**, *34*, 191–201.

[229] D. R. Huffman, R. L. Wild, *Phys. Rev.* **1967**, *156*, 989.

[230] T. Oguchi, K. Terakura, A. R. Williams, *Phys. Rev. B* **1983**, *28*, 6443.

[231] D. Hobbs, J. Hafner, *J. Phys. Condens. Matter* **1999**, *11*, 8197.

[232] C. Bradley, A. Cracknell, *The mathematical theory of symmetry in solids: representation theory for point groups and space groups*, Oxford University Press, **2009**.

[233] R. Tappero, P. D'Arco, A. Lichanot, *Chem. Phys. Lett.* **1997**, *273*, 83–90.

[234] H. Sato, T. Mihara, A. Furuta, M. Tamura, K. Mimura, N. Happo, M. Taniguchi, Y. Ueda, *Phys. Rev. B* **1997**, *56*, 7222.

[235] P. Raybaud, G. Kresse, J. Hafner, H. Toulhoat, *J. Phys. Condens. Matter* **1997**, *9*, 11085.

[236] D. Orgassa, H. Fujiwara, T. C. Schulthess, W. H. Butler, *Phys. Rev. B* **1999**, *60*, 13237.

[237] B. Dutta, F. Körmann, S. Ghosh, B. Sanyal, J. Neugebauer, T. Hickel, *Phys. Rev. B* **2020**, *101*, 094201.

[238] E. Jahne, O. Goede, V. Weinhold, *Phys. Status Solidi (b)* **1988**, *146*, K157–K160.

[239] G. Khaliullin, S. Maekawa, *Phys. Rev. Lett.* **2000**, *85*, 3950.

[240] N. Pavlenko, T. Kopp, E. Tsymbal, J. Mannhart, G. Sawatzky, *Phys. Rev. B* **2012**, *86*, 064431.

[241] B. Lee, K. M. Choi, H.-S. Ahn, S. Han, J. Lee, et al., *Phys. Rev. Lett.* **2007**, *98*, 115503.

[242] K. Eom, E. Choi, M. Choi, S. Han, H. Zhou, J. Lee, *J. Phys. Chem. Lett.* **2017**, *8*, 3500–3505.

[243] M. Sing, H. O. Jeschke, F. Lechermann, R. Valentí, R. Claessen, *Eur. Phys. J. Spec. Top.* **2017**, *226*, 2457–2475.

[244] T. Feng, L. Lindsay, X. Ruan, *Phys. Rev. B* **2017**, *96*, 161201.

[245] V. Popescu, A. Zunger, *Phys. Rev. B* **2012**, *85*, 085201.

Acknowledgement

This work was supported by the Helmholtz Association through *funding of first-time professorial appointments of excellent women scientists (W2/W3)*. I am grateful to the Gauss Centre for Supercomputing e.V. (www.gauss-centre.eu) for funding this project by providing computing time through the John von Neumann Institute for Computing (NIC) on the GCS Supercomputer JUWELS at Jülich Supercomputing Centre (JSC) under projects **abinitiomodmatsgeo** and **geopressmagphon**. I would also like to thank GFZ for additional funding that has allowed to finish this work.

At this point, I would like to thank everyone who has influenced the making of this thesis in one way or the other.

First and foremost, I would like to thank my supervisor Prof. Dr. Maribel Núñez-Valdez for giving me this opportunity and fostering a harmonious work environment, granting me both autonomy and valuable guidance. Being able to count on her diverse expertise proved immensely beneficial and for that I cannot express my gratitude enough. I am also grateful to Prof. Dr. Björn Winkler for agreeing to be the co-supervisor and giving me the opportunities to present my work at the seminars of his group at the Goethe Frankfurt University. His comments and insights were of great help in completing this work. Additionally, I want to thank my former supervisor Prof. Dr. Liviu Chioncel from the University of Augsburg who has remained in touch and been always ready to offer useful advice and insight into various computational aspects.

I would also like to thank all of my colleagues at GFZ without whom the completion of this thesis would not have been possible. My special thanks go out to Dr. Sergio Speziale, Dr. Sergey Lobanov and Prof. Dr. Monika Koch-Müller. Their deep understanding of different experimental techniques has been immensely valu-

able in connecting computational modeling with real-life situations.

Finally, I would like to thank my family and friends who have supported me throughout all these years. Their unwavering courage and optimism even in the hardest of times have been an endless source of inspiration. I want to dedicate this thesis to my late grandfather; the moments we shared together are some of my fondest memories which I will cherish forever.